

Simulation of plasma turbulence in the periphery of diverted tokamaks

THÈSE N° 8944 (2018)

PRÉSENTÉE LE 16 NOVEMBRE 2018
À LA FACULTÉ DES SCIENCES DE BASE
SPC - THÉORIE
PROGRAMME DOCTORAL EN PHYSIQUE

ÉCOLE POLYTECHNIQUE FÉDÉRALE DE LAUSANNE

POUR L'OBTENTION DU GRADE DE DOCTEUR ÈS SCIENCES

PAR

Paola PARUTA

acceptée sur proposition du jury:

Prof. F. Courbin, président du jury
Prof. P. Ricci, directeur de thèse
Dr E. Serre, rapporteur
Dr N. Vianello, rapporteur
Dr B. Labit, rapporteur



ÉCOLE POLYTECHNIQUE
FÉDÉRALE DE LAUSANNE

Suisse
2018



*“Look — It’s Low Carbon Emission Man”*¹

Dedicated to my mum and dad...
(don’t worry, you don’t need to read the rest)

¹ Reproduced by kind permission of PRIVATE EYE

Acknowledgements

I would like to begin by thanking those teachers and professors who have been role models for me and have passed on to me their passion for science. In particular Pasquale Pucciani, my secondary school teacher, whom I remember as one of the most virtuous and moral people I have ever met, I am glad I was your student. At university, Prof. Alfio Quarteroni got me fascinated with numerics, as if it was a game, a riddle to solve. Professor Rony Keppens was the first teacher I had the pleasure to work closely to, when I was in Belgium for my master thesis. Thank you for believing in me and giving me the freedom to investigate what tickled my curiosity. I also want to thank my thesis supervisor Paolo Ricci without whom this work would not have been possible. He was always available whenever I needed him and he made the transition from the world of mathematics, where I lived in for many years, to the one of plasma physics as smooth as possible. A big thank you goes to Prof. Marcia Portella Oberli, I do not know if I would be crossing the finish line if I did not have the chance of having you as my mentor.

This thesis was the result of four years of mostly solitary research, nonetheless, some of my major achievements resulted from the interaction with other PhD students, Professors and Scientific personnel at the Swiss Plasma Center (SPC). It was thank to Tony Cooper that, a couple of months into the investigation of possible flux coordinates for diverted configuration, I discovered that flux coordinates are always singular at the X-point. He spared me the extra months that I would have wasted before realising it myself. The work on TCV would not have seen the light without Samuel Lanthaler. I had summed all the PhD students at a seminar to try and figure out which magnetic configuration I could simulate with the new code, Sam said TCV, I told him it was not going to work, that I needed an analytical expression, 10 minutes into the conversation with him, I was convinced that it was indeed possible, and 3 months later I was looking at the results of the first TCV-simulation. That was a great feeling. Francesco Carpanese, Olivier Sauter, Roberto Maurizio, Jean-Marc Moret, Joaquim Loizu and Davide Galassi all contributed to the success of the work on TCV. For the blob chapter, a lot of the credit goes to Christian Theiler, who co-supervised me together with Paolo and helped me make sense of otherwise cryptic reference papers. Federico Nespoli, Benoit Labit and Cedric Tsui were kind enough to share their knowledge, opening up a window on real-life blobs that exist outside the world of computer and simulations. To my officemate Julien, honestly, I will never thank you enough. You believed in me and supported me. The experience I had at Princeton was professionally one of the most satisfying of my life. You are a great friend.

And a great running buddy. To Carrie, my other officemate, thank you for patiently listening to my rants when the code would crash (those very few isolated times it did). I cannot count the time I interrupted your work to share my wandering thoughts out loud. Also thank you for the double-null simulation. You are one of the strongest people I know and you are incredibly smart. It was a pleasure to share these last two years with you.

If you are reading this, you are probably either a PhD student yourself or you know me, either way, directly or indirectly you know PhD life can be tough. And not just I'm-having-a-bad-day tough, I am talking feeling-like-you-are-loosing-your-mind tough. Friends and family are what helped me move on and keep it all together. This thesis, this achievement, also belongs to them. There are so many I want to thank, I hope there is no page limit to the acknowledgments section. Let me start by thanking the SPC PhD family that welcomed me when I arrived, naive and happy as I was. You guys create a great environment, no competition whatsoever, plenty of aperos, and Great Escape-No Name combos that I enjoyed especially in the first couple of years of my PhD. Special mention goes to Pedro, J. Faustin, Fed, Stipa, Emmanuel, Pesa, Matteo and Jérémy - the PhD apero masterchefs. To Umar, the puppeteer behind some life changing events. To Italy, with love, I would like to thank my always faithful friends Cecio and Ema. The fact that we managed to keep in touch across borders moves me, PEC forever. I would also like to thank the other few bravehearted that visited me here in Lausanne: Eva, François Clerens and BEST LLN. Your visits meant a lot.

Thank you, Hamish. We shared a good chunk of this PhD experience. You have witnessed all of those hard times I have mentioned and most of the good ones, too. One word is too much and two is too little. Thank you for being by my side. And never more than six meters and a wall away.

Now, in *chronological* order, Josefine, Nico, Justin, Manue and Christina. I cannot help smiling when I think of you. You are amazing friends. Jojo, you took care of me when I most needed it, I will be forever grateful. It fills me with joy knowing that I can always count on someone as sweet and kind as you. Nico, you are one of the most generous people I know, and it is also thanks to you and Rouchoz that I decided I want to stay in Lausanne. Justin! Climbing buddy and my favourite American. Thanks also for helping me out with the thesis, by taking the time to discuss with me when I could not make sense of some physics results, and by proof reading it. Manue, petit raccoon, you are the one who steadies the ship when I am all over the place. Thank you for tolerating me in these last few crazy months. And finally, Christina, thanks for sharing #misery weekends that made me feel less lonely when I was writing up my thesis.

To my family, because although you are far away, you are always with me. Your unwavering support and unconditional love got me where I am.

Abstract

The turbulent plasma dynamics in the periphery of a fusion device plays a key role in determining its overall performance. In fact, the periphery controls the heat load on the vessel walls, the plasma confinement, the level of impurities in the core, the plasma fuelling and the removal of fusion ashes. Hence, understanding and predicting the plasma turbulence in this region is of crucial importance for the success of the fusion program.

The GBS code has been developed in past years to simulate plasma turbulence in the periphery of limited tokamaks. The goal of the present thesis is to extend GBS to the treatment of diverted scenarios. Such configurations are of interest for present state-of-the-art experiments and future fusion reactors. For the implementation of this geometry, we express the model in toroidal coordinates, abandoning the flux coordinates previously used in limited configuration, and overcoming the singularity that this coordinate system presents at the X-point of diverted configurations. The accuracy of the numerical scheme is improved by upgrading the second order finite differences scheme to fourth order on staggered grids. The resulting version of GBS is carefully verified through a series of tests (i.e., a benchmark with the previous version of GBS in limited configuration, a rigorous check of the correctness of the code implementation with the method of manufactured solutions, and a convergence study on a relatively simple diverted configuration).

The results of a GBS simulation is then used to investigate the dynamics of coherent turbulent structures, called blobs, that characterise plasma turbulence in the periphery of fusion devices. A diverted double-null configuration is considered, and the blob motion is studied using a pattern recognition algorithm. The velocity of the blobs in the presence of an X-point matches the analytical scaling that we derived by considering the different blob properties in the divertor and main SOL regions, retaining the correction terms that account for blob density and ellipticity. In addition, we show that the blob current pattern observed in the simulation results match the theoretical expectations.

Finally, the new version of GBS is run with a realistic diverted magnetic equilibrium, taken from an experiment carried out on the TCV tokamak. First insights of the turbulence properties are in good agreement with the current physical understanding of plasma dynamics in the periphery of diverted tokamaks.

Riassunto

La dinamica turbolenta del plasma nella regione di bordo (periferia) dei reattori a fusione svolge un ruolo cruciale nel determinarne le prestazioni complessive. Infatti, la periferia controlla il carico di calore sulle pareti, il confinamento del plasma, il livello di impurità nel nucleo, il rifornimento di plasma e la rimozione delle ceneri risultanti dalle reazioni di fusione. Pertanto, comprendere e prevedere la dinamica turbolenta del plasma in questa regione è di cruciale importanza per il successo dell'intero programma.

Il codice numerico GBS è stato sviluppato nell'ultimo decennio per simulare la turbolenza del plasma nella periferia di macchine tokamak in configurazione magnetica *limited*. L'obiettivo di questa tesi è di estendere GBS al trattamento di configurazioni magnetiche con divertore, di interesse per gli attuali esperimenti e per i futuri reattori a fusione. Le coordinate di flusso usate in configurazione limitata presentano una singolarità al cosiddetto punto a X in configurazioni con divertore, per questo motivo il modello fisico è qui riformulato in coordinate toroidali. La precisione dello schema numerico è migliorata passando da differenze finite al secondo ordine a differenze finite al quarto ordine su griglie sfalsate. La nuova versione di GBS è accuratamente verificata attraverso una serie di test: un confronto con la versione precedente in configurazione limitata, un rigoroso controllo di correttezza dell'implementazione con il metodo delle soluzioni fabbricate e uno studio di convergenza su una configurazione con divertore relativamente semplice.

Quindi, il codice è utilizzato per indagare la dinamica dei blob, strutture coerenti di plasma che caratterizzano la turbolenza nella periferia. Partendo da una simulazione in configurazione con divertore con due punti a X, chiamata double-null (doppio-nullo), il movimento del blob viene tracciato utilizzando un algoritmo per il riconoscimento delle immagini. I risultati ottenuti riproducono le previsioni analitiche per la velocità dei blob in presenza di punti a X, qui derivate considerando le diverse proprietà dei blob nel divertore e nella zona periferica principale, mantenendo i termini che tengono conto della densità e dell'ellitticità dei blob. Inoltre, in questa simulazione, il flusso della corrente interna ai blob è in accordo con le aspettative teoriche.

La nuova versione di GBS viene usata per simulare la turbolenza periferica per un equilibrio magnetico con divertore, tratto da un esperimento effettuato sul tokamak TCV. I risultati preliminari sono in generale accordo con l'attuale comprensione fisica della turbolenza nella periferia del plasma.

Contents

Acknowledgements	v
Abstract	vii
Riassunto	viii
1 Introduction	1
1.1 The tokamak reactor	2
1.2 The plasma periphery	2
1.3 Challenge behind simulations of diverted configurations	5
2 Physical model in toroidal coordinates	9
2.1 Drift-reduced Braginskii's equations	9
2.2 Differential operators in toroidal coordinates	13
2.2.1 Physical operators scale lengths	13
2.2.2 Toroidal coordinates	14
2.2.3 Magnetic field in toroidal coordinates	15
2.2.4 Operators in toroidal coordinates	16
2.2.5 Ordering of the magnetic field components	17
2.2.6 Assumption on plasma quantities derivatives in toroidal coordinates . .	19
2.2.7 Simplified operator expressions	19
2.3 Radial boundary conditions	24
2.4 Initial conditions	25
3 Numerical implementation and code verification	27
3.1 Code structure	27

Contents

3.2	Spatial discretisation	28
3.2.1	Numerical grid and staggering	28
3.2.2	Fourth order finite differences	30
3.3	Implementation of the boundary conditions	32
3.4	Parallelisation	32
3.5	Comparison with previous version of GBS in limited configuration	33
3.6	Verification of GBS with the method of manufactured solution	38
3.7	Convergence study	41
4	Blobs	47
4.1	The two-region model for the blob dynamics in diverted configuration	48
4.2	Blob tracking in double-null GBS simulation	57
4.3	Comparison of the simulation results with the two-region model	62
5	TCV-like simulation	69
5.1	Exporting a TCV magnetic equilibrium to GBS	69
5.2	Simulation settings	72
5.2.1	Initial conditions and wall sources	73
5.2.2	Physical parameters	73
5.2.3	Revised wall boundary conditions	74
5.2.4	Source of parallel momentum and inner radial boundary conditions	74
5.3	Preliminary results	78
5.3.1	Radial turbulent transport	84
5.3.2	Poloidal rotation	86
5.4	Outlook	87
6	Summary	89
	Bibliography	99
	Curriculum Vitae	101

1 Introduction

Fusion aims at providing clean energy based on practically inexhaustible fuel, to support the increasing world energy demand, without impacting the Earth climate. Fusion reactions currently powers the stars by fusing mainly hydrogen atoms together and generating enormous amount of energy. In a earthbound fusion power plant, two isotopes of hydrogen (deuterium and tritium) will be brought to an energy of about 10 keV and will fuse together to release 18 MeV, as the kinetic energy of an alpha particle (14 MeV) and of a neutron (4 MeV) [1]. The alpha particles, consisting of two protons and two neutrons, will be used to heat up the fresh fusion fuel, keeping the reaction going, while the neutrons will be, first, used to produce tritium, which cannot be found in nature, by having them collide with lithium and, ultimately, their energy will be harvested and converted into electricity.

The advantages of fusion are multiple. Its energy density, i.e. energy produced per unit mass of fuel, is millions times higher than fossil fuels: 1 kg of deuterium and 3 kg of lithium can support the energy demand of 100 people for their entire lifetime, one would need 15.000.000 kg of coal to achieve the same [2]¹. Unlike fossil fuels, fusion does not emit CO_2 , primal responsible of the world's quickly rising temperatures and climate change. Moreover, fusion fuel is widely available and abundant, deuterium can be found naturally in water, while lithium is present in the Earth crust and in ocean water. Fusion power plants based on deuterium-tritium reactions could power the world for 100 million years before running out of lithium. If we were able to master deuterium-deuterium reactions, we could use fusion for 10 billion years [3]. Unlike solar or wind, fusion does not depend on weather conditions. In fact, intermittency, which is nowadays a limiting factor in the use of many reusable energies [4], does not concern fusion energy. With respect to other renewable sources, such as hydroelectric or tidal, fusion is not contingent to a country's geography. Radioactivity is not an issue for fusion reactors in the same way it is for fission ones. The lithium and deuterium are not radioactive, tritium is, but its half life is short (12.5 years) and will be produced and consumed in within the power plant. Energetic neutrons instead can activate the reactor's structural material, but this radioactivity is short-lived especially if compared to fission. Indeed, it takes 100 years for fusion and 1 million for fission waste to become safe to handle [5]. Finally, there is no risk of nuclear

¹Based on an average power consumption of 1kW for a lifetime of 80 years, with a fusion power plant producing an harvesting an energy of 70 million kWh from 1kg of deuterium and 3kg of tritium.

accidents in fusion, since it is not based on a chain reaction, like fission is. In fact, achieving controlled fusion requires a fine tuning of different parameters, which makes fusion hard to achieve, but extremely easy to stop.

The downsides to fusion are caused by the incredible technological challenge that comes with it. One is the huge up-front down-payment needed to fund the research. For example ITER, the world research project expected to prove the feasibility of fusion energy, costs around 20 billion Euros. The second big downside is timing, with the present level of funding, most likely fusion will not be an energy option in the first half of this century, meaning that other low-carbon energy solutions need to be considered in the immediate future to tackle climate change.

1.1 The tokamak reactor

Deuterium and tritium fuse at energies of 10 keV, corresponding to a temperature of about 100 million degrees Celsius. At this temperature matter is completely ionised, made of ions and electrons, in the so-called plasma state. A plasma has to be confined sufficiently long and at sufficiently high density to produce electricity. In the present thesis we focus on plasma confinement based on the use of magnetic fields. In the presence of a magnetic field, the Lorentz force causes particles to gyrate, confining their motion perpendicularly to the magnetic field line. In a tokamak fusion device (Fig. 1.1), a plasma is confined by using a magnetic field in a toroidal chamber. In this configuration poloidal and toroidal components of the magnetic field results in helical field lines. The helical lines looping around the torus map nested toroidal surfaces, called flux surfaces (see Fig. 1.1). The toroidal component of the magnetic field is created by a set of poloidal coils. The poloidal magnetic field, instead, is generated through induction, by a ramp up of current in a coil located at the center of the torus. As the current cannot be increased indefinitely, tokamak operation is inherently pulsed. A detail description of a tokamak device can be found in [1].

1.2 The plasma periphery

Because of collisions and turbulence, plasma is not perfectly confined in a tokamak and tends to flow outwards, across the flux surfaces, eventually reaching the tokamak wall. To avoid the hot plasma outflow damaging the first wall of the reactor, the plasma is channelled towards the limiter or the divertor plates, made to withstand high energy fluxes. A limiter can be either a metal rail that intercepts the outermost flux surfaces, or it can be integral part of the inboard wall, which the flux surfaces are pushed towards. Fig. 1.2 (left) sketches the poloidal cross section of a plasma limited by a toroidal rail (in blue), that extends along the toroidal direction. The limited configuration was implemented in the early days of fusion history. Nowadays, diverted configurations are preferred since they move the interaction of the plasma with the wall further away from the core of the reactor. In a diverted single-null scenario, the shape of the outer flux surface is modified using external coils to create two legs, ending at the divertor plates.

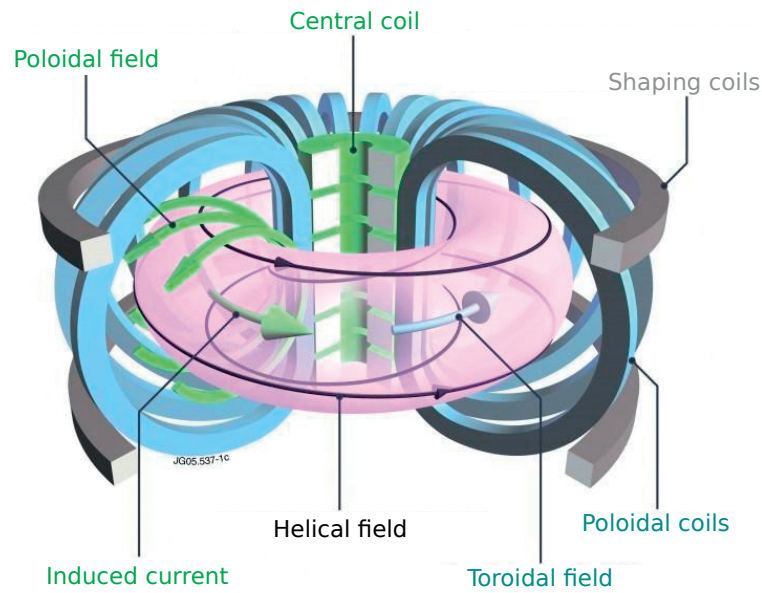


Figure 1.1 – Schematic representation of a tokamak magnetic cage. The poloidal coils generate the toroidal magnetic field (in blue). A current ramp up in the central coil induces a toroidal current in the plasma that generates the poloidal magnetic field (in green). The combination of toroidal and poloidal fields, results in an helical field line (in black) that wraps around the torus, defining the flux surface in pink. Image credit Euro-fusion.

Three main nested regions can be identified in Fig. 1.2 for both limited and diverted scenarios: the core, the edge and the scrape-off layer (SOL). The core is the hottest central part where fusion reactions take place; temperature and density decrease moving radially outwards, until the edge region is reached, where the plasma is relatively cold. Here, the formation of a steep pressure gradient might be observed, due to a transport barrier. Both the core and the edge are characterised by magnetic field lines that lie on nested closed toroidal surfaces. In contrast, the SOL is the outermost region where magnetic field lines are “open”, in the sense that they do not close inside the tokamak chamber and they intercept the wall of the machine. With the term periphery we identify the colder region of the tokamak, composed by the edge and the SOL. This region is highly turbulent and characterised by the presence of coherent turbulent structures, called blobs, that detach from the main plasma and move radially outwards. The SOL and the edge are separated by the last closed flux surface, also called separatrix. Note that the separatrix in fig 1.2 (right) displays an X-point, which corresponds to a location where the magnetic field is purely toroidal. In general, various shapes for the separatrix are possible, and they are characterised by the number or type of X-points present. We can have single-null (like the one presented here), double null (two X-point at top and bottom) and snowflake (where two X-points coincide) configurations.

The interaction between the SOL plasma and its surrounding walls represents one of the main challenges of the fusion program. Recent investigations of the heat load on the wall of existing tokamaks show alarmingly narrow features of the heat flux profile in the proximity of the last

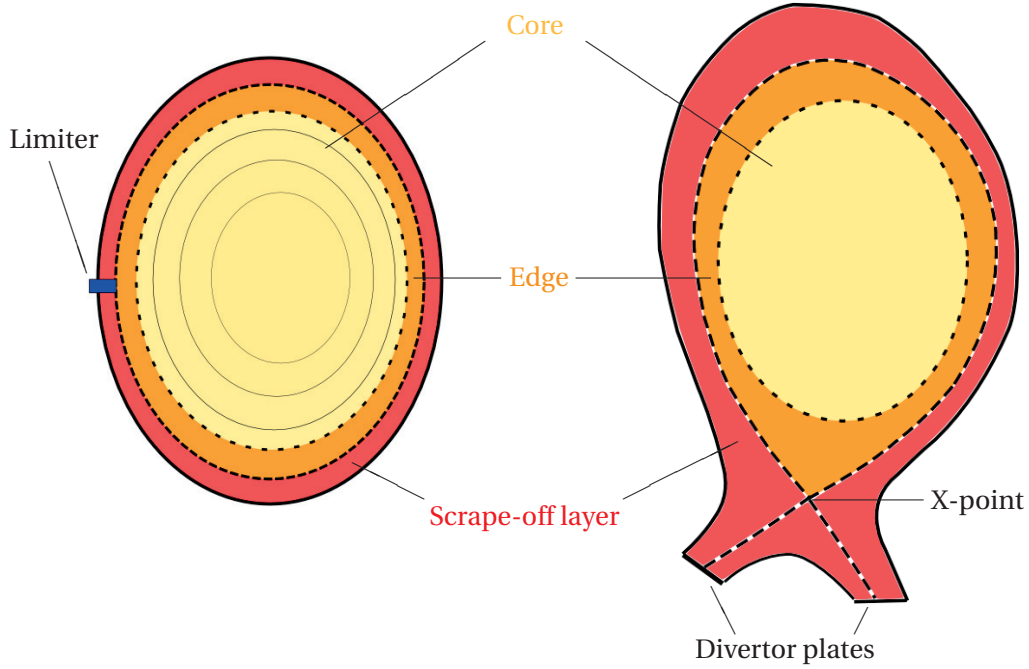


Figure 1.2 – Illustration of the poloidal cross-section of a limited (left) and of a diverted (right) tokamak configuration.

closed flux surface [6]. Empirical extrapolations point out that, in ITER, the quasi totality of the heat produced by fusion reactions might be exhausted over a surface 1mm thick, exceeding the heat flux limit of 5MW/m^2 , above which the wall is damaged [7]. Moreover, plasma fueling, impurities and neutral dynamics are all governed by the complex physics that takes place in the plasma periphery of a tokamak device. Hence, understanding and predicting the plasma turbulence in this region, with the use of simulation codes, is of crucial importance for the success of fusion [8].

From a modelling point of view, multiple challenges arise when approaching the tokamak periphery. Phenomena occurring on a wide range of length and time scales are present, from the electron gyro-radius to the machine major radius; from the gyro-motion to the turbulence time scale. The presence of large amplitude turbulent structures does not allow for the decoupling between fluctuating and background quantities.

GBS is a three-dimensional first-principles simulation code that has been developed in the past years in order to study the plasma turbulence dynamics in the tokamak periphery. Similarly to other codes developed for the same reason (BOUT++ [9], TOKAM3X [10], GBD [11], GRILLIX [12], HESEL [13]), GBS evolves the drift-reduced Braginskii's equations [14]-[15], a set of fluid equations valid in the high-collisionality regime of the tokamak periphery. In the past years GBS has contributed to progress our understanding of the SOL physics in limited configurations, where the SOL is defined by a toroidal or poloidal limiter. For example, GBS has provided predictions of the SOL width [16] in this configuration. The work discussed in the present thesis is focused on extending GBS to the treatment of diverted tokamak scenarios.

1.3 Challenge behind simulations of diverted configurations

The main challenge related to the implementation of a diverted configuration into a simulation code is the choice of a proper coordinate system. As charged particles move freely along the magnetic field line, whereas their motion is constrained in the direction orthogonal to it, parallel and perpendicular dynamics in a magnetised plasma occur on very different length scales. In particular, most plasma properties are approximately constant on flux surfaces and vary sharply across them. Therefore a coordinate system where the basis vectors identify parallel and perpendicular directions has the advantage of reducing the computational cost of the simulations.

In most code implementations, as well as in the limited version of GBS [17], a coordinate whose contour lines correspond to the flux surfaces is chosen as one of the two perpendicular coordinates. Such flux coordinate can be identified with the magnetic poloidal flux ψ , the function that allows expressing the tokamak toroidally symmetric equilibrium magnetic field as:

$$\mathbf{B} = F(\psi)\nabla\varphi + \nabla\psi \times \nabla\varphi \quad (1.3.1)$$

which ensures $\nabla \cdot \mathbf{B} = 0$ [18]. The first term on the right-hand side of Eq. (1.3.1) represents the toroidal component of the magnetic field, $F(\psi)$ being a scalar function of ψ , and the second term identifies the poloidal component, φ being the toroidal angle. For a toroidally symmetric magnetic field, the poloidal flux ψ does not depend on φ , $\nabla\varphi \cdot \nabla\psi = 0$. From Eq. (1.3.1), it follows that $\mathbf{B} \cdot \nabla\psi = 0$. This shows that ψ contour lines correspond indeed to the flux surfaces on which the magnetic field lies and that the contravariant basis vector $\nabla\psi$ always conveniently points in a direction orthogonal to the magnetic field line and to the flux surface, as desired.

In diverted equilibria, the use of the poloidal flux ψ as one of the coordinates is complicated by the presence of one or multiple X-points. At these locations, the magnetic field is purely toroidal and has no component in the poloidal plane. Equation (1.3.1) implies $\nabla\psi \times \nabla\varphi = 0$ and consequently $\nabla\psi = 0$ at the X-point. In fact, the X-point is defined as a saddle point of the magnetic flux ψ . As a consequence, a coordinate system that uses the flux coordinate in diverted configuration, is singular at the X-point, in fact its Jacobian is $J = (\nabla\psi \cdot \nabla\alpha \times \nabla\varphi)^{-1} = \infty$ ($\nabla\alpha$ denoting a third basis vector, in addition to $\nabla\psi$ and $\nabla\varphi$). Moreover, the use of a flux coordinate is made problematic by the flux expansion around the X-point: in the proximity of the X-point, since $\nabla\psi$ is small, the spacing between the ψ contour lines becomes larger than at the midplane. This makes it challenging from a numerical standpoint to attain a good physical resolution around the X-point. Indeed, a uniform spacing in ψ does not correspond to a uniform spacing in physical space, and an over-resolution at mid-plane is needed in order to attain a good resolution around the X-point, increasing the computational cost of a simulation.

Various approaches are being followed to tackle the singularity of the flux coordinate in diverted equilibria. In BOUT++ [9] and TOKAM3X [10], the use of the flux coordinate is retained

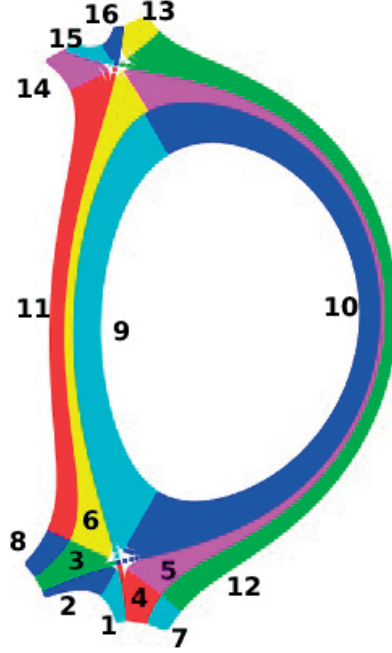


Figure 1.3 – Example of domain decomposition linked to the use of flux coordinates in TOKAM3X for WEST tokamak (courtesy of F. Nespoli). Here 8 domains meet at the X-point, complicating the numerical treatment of the region.

also in diverted scenarios, but the numerical grid points are generated to avoid falling on the X-point position. This bypasses the problem of the singularity at the X-point but does not solve the low resolution issue due to the flux expansion. In addition, usually this approach is implemented by decomposing the domain in sub-domains which are rectangular in the (ψ, α) coordinates (α indicating the chosen poloidal coordinate). Fig 1.3 shows the domain decomposition used by TOKAM3X for WEST tokamak. The downside is that the X-point becomes the point at which the domains are glued together, complicating the numerical treatment of a region of high physical interest that is already unresolved when using flux coordinates. In GRILLIX [12], flux coordinates are abandoned in favour of Cartesian coordinates in the poloidal plane. To compensate the lack of alignment of the coordinates to the magnetic flux, an effort to accurately capture the parallel direction is put in place by carefully handling the parallel operator with the Flux Coordinate Independent (FCI) method [19]-[20]. HESEL and GBD instead do not include X-point geometries.

In GBS we choose to step away from the use of flux coordinates and, instead, use the toroidal coordinates (r, θ, φ) , which are defined as:

$$\begin{aligned} x &= R \cos \varphi = (R_0 - r \cos \theta) \cos \varphi \\ y &= R \sin \varphi = (R_0 - r \cos \theta) \sin \varphi \\ z &= Z_0 + r \sin \theta \end{aligned} \tag{1.3.2}$$

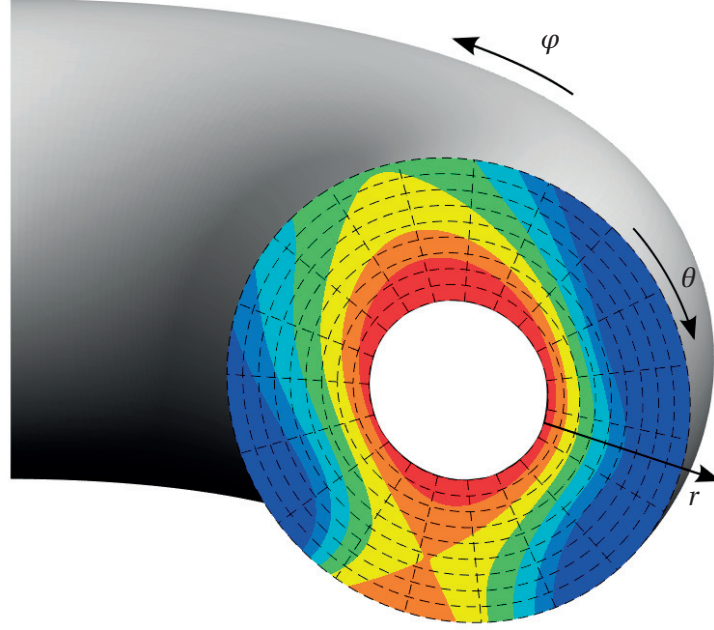


Figure 1.4 – Visualisation of the toroidal coordinates (r, θ, φ) used to implement diverted configuration in GBS. The corresponding grid (in dashed lines) is not aligned to the poloidal flux ψ (represented by the color-plot).

being R the distance from the symmetry axis of the torus, θ the poloidal angle, and r the distance in the poloidal plane from the point located at $R = R_0$ and vertical position Z_0 . This allows us to easily enclose the edge and SOL of a diverted plasma in a domain that corresponds to a rectangular box in the (r, θ, φ) coordinates, unlike in the case of flux coordinates or Cartesian coordinates (R, Z, φ) . In addition, the coordinate system and numerical method we propose have the advantage of being flexible, allowing the straightforward implementation of double-null [21] or snowflakes [22] configurations.

To partially compensate for the loss of alignment of the coordinate system to the magnetic field, we increase the order of accuracy of the numerical scheme.

This thesis is organised as follows. In chapter 1 we presented the potential of fusion as a source energy for humankind and the basic mechanism of the tokamak fusion device (see Sec. 1.1). Section 1.2 highlighted the importance simulating plasma turbulence in the tokamak periphery, motivating the work of this thesis, which consists in extending the GBS code capabilities to the simulation of the periphery of diverted tokamaks. We discussed the downsides of flux coordinates for the implementation of diverted equilibria and our choice of using *non*-flux aligned toroidal coordinates in Sec. 1.3.

Chapter 2 focuses on the drift-reduced Braginskii's equations solved by GBS (Sec. 2.1). It reports on the analytical derivation of differential operators in the new toroidal coordinate system (Sec. 2.2) and completes the physical picture by presenting the boundary conditions

used at the wall and at the divertor legs (Sec. 2.3). Finally the initial condition are presented (Sec. 2.4).

The first part of chapter 3 is dedicated to the numerical implementation, in toroidal coordinates, of the physical model presented in chapter 2, in order to allow for a diverted equilibrium, starting from the existing limiter version of GBS [23]: after introducing the code structure (Sec. 3.1), the new grid and the upgraded numerical scheme are detailed (Sec. 3.2), followed by the implementation of the wall boundaries (Sec. 3.3). The second part of the chapter is dedicated to the verification of the new code by testing its parallelisation properties (Sec. 3.4), by benchmarking it with the previous version of GBS in the case of a limited configuration (Sec. 3.5), by using the rigorous method of manufactured solution to check the convergence order of the algorithm (Sec. 3.6), and, finally, by running the first diverted equilibrium with GBS and proving that it converges when increasing the grid resolution (Sec. 3.7).

In chapter 4, we investigate the physical properties of turbulence in the case of a double null equilibrium. Following the work of Myra *et al.* [24], we derive an analytical scaling for blob velocity in the presence of an X-point (Sec. 4.1). We then present the blob tracking technique used for the double-null GBS simulation (Sec. 4.2) and, finally, the numerical results are compared with the analytical predictions (Sec. 4.1).

In chapter 5), a TCV single-null is implemented into the new version of GBS. Some modification to boundary conditions, initial conditions and source terms are required to improve code stability as well as the physical model, and are presented in Sec. 5.2. A preliminary analysis of the turbulent dynamics in the simulation result is performed in Sec. 5.3. Finally, the importance of the inner radial boundary condition is the subject of Sec. 5.4. A Summary of the thesis follows.

2 Physical model in toroidal coordinates

The present chapter details the physical model used by GBS to evolve plasma turbulence in the tokamak periphery and it provides expressions of the differential operators in toroidal coordinates. The physical model is a two-fluid model resulting in a set of equations known as the drift-reduced Braginskii's equations. The model and its derivation are detailed in section 2.1. The spatial differential operators, appearing in the drift-reduced Braginskii's equations, act either in the direction parallel to the magnetic field or in the one perpendicular to it, and therefore involve very different scale lengths. Since our coordinate system is not aligned to the magnetic field, the projection on it of the parallel and perpendicular operators mixes the different scale lengths. The derivation of the differential operators and their simplification in the case of large aspect ratio and high safety factor approximation is the subject of section 2.2. Finally, the physical model is completed by introducing boundary conditions and initial conditions in sections 2.3 and 2.4.

2.1 Drift-reduced Braginskii's equations

Since the plasma at the periphery of a tokamak device is sufficiently collisional that deviations from a Maxwellian distribution are small, a fluid description, such as the one derived by Braginskii [14], is generally used. These equations express the conservation of density, momentum, energy and electric charge of a quasi-neutral plasma. Formally, they are derived by taking the moments of Boltzmann's equation.

Here we derive the density equation (2.1.11) and refer to [14], [15], and [25] for the derivation of the complete set of equations. Boltzmann's equation for the electron distribution function $f_e = f_e(\mathbf{x}, \mathbf{v}, t)$ states that:

$$\frac{\partial f_e}{\partial t} + \nabla_{\mathbf{x}} \cdot (\mathbf{v} f_e) - e \nabla_{\mathbf{v}} \cdot \left(\frac{\mathbf{E} + \mathbf{v} \times \mathbf{B}/c}{m_e} f_e \right) = C \quad (2.1.1)$$

where \mathbf{v} is the velocity of the electrons, \mathbf{E} and \mathbf{B} are the electric and magnetic field, e and m_e are the electric charge and mass of the electrons. Integrating over velocity space and defining

Chapter 2. Physical model in toroidal coordinates

the electron density $n_e = \int f_e(\mathbf{x}, \mathbf{v}) d\mathbf{v}$ one obtains the continuity equation:

$$\frac{\partial n_e}{\partial t} + \nabla \cdot (n_e \mathbf{v}_e) = 0 \quad (2.1.2)$$

where \mathbf{v}_e is the electron fluid velocity defined as the first moment of Boltzmann's equation, $\mathbf{v}_e = \int \mathbf{v} f_e(\mathbf{x}, \mathbf{v}) d\mathbf{v} / n_e$.

Since turbulence occurs on a time scale considerably longer than the gyro-motion ($\partial_t \ll \Omega_{ci} = eB/(m_i c)$) and on a scale length larger than the ion sonic gyro-radius, $\rho_s = c_s/\Omega_{ci}$, with $c_s = \sqrt{T_e/m_i}$, the drift approximation of the particle orbits can be used to simplify Braginskii's equations, as shown by Zeiler [15]. Considering only leading order terms, the velocity can be split into the component parallel to the magnetic field and the perpendicular drifts, i.e. the $\mathbf{E} \times \mathbf{B}$ and diamagnetic drift, that is:

$$\mathbf{v}_e = \mathbf{v}_{\parallel, e} + \mathbf{v}_{\perp} = \mathbf{b} v_{\parallel, e} + \mathbf{v}_E + \mathbf{v}_{d, e} \quad (2.1.3)$$

with

$$\mathbf{v}_E = -\frac{c}{B} \nabla \phi \times \mathbf{b} \quad (2.1.4)$$

$$\mathbf{v}_{d, e} = -\frac{c}{en_e B} \mathbf{b} \times \nabla (n_e T_e) \quad (2.1.5)$$

Substituting Eq. (2.1.3) into $\nabla \cdot (n_e \mathbf{v}_e)$:

$$\nabla \cdot (n_e \mathbf{v}_{\parallel, e}) = \mathbf{b} \cdot \nabla (n_e v_{\parallel, e}) + n_e v_{\parallel, e} \nabla \cdot \mathbf{b} \approx \nabla_{\parallel} (n_e v_{\parallel, e}) \quad (2.1.6)$$

$$\begin{aligned} \nabla \cdot (n_e \mathbf{v}_E) &= cn_e \nabla \times \frac{\mathbf{b}}{B} \cdot \nabla \phi + \frac{c}{B} \mathbf{b} \cdot \nabla \phi \times \nabla n_e \\ &= \frac{2cn_e}{B} C(\phi) + \frac{c}{B} [\phi, n_e] \end{aligned} \quad (2.1.7)$$

$$\nabla \cdot (n_e \mathbf{v}_{d, e}) = -\frac{2c}{eB} C(n_e T_e) \quad (2.1.8)$$

In eq (2.1.6) we neglected the divergence of \mathbf{b} since it is proportional to the tokamak inverse aspect ratio a/R_0 (a minor radius and R_0 major radius), this will be proven in the section 2.2. The parallel operator $\nabla_{\parallel} u$, the curvature operator $C(u)$ and the Poisson brackets operator $[\phi, u]$, u being an arbitrary fluid quantity, in physical units are defined as:

$$\nabla_{\parallel} u = \mathbf{b} \cdot \nabla u, \quad C(u) = \frac{B}{2} \left(\nabla \times \frac{\mathbf{b}}{B} \right) \cdot \nabla u, \quad [\phi, u] = \mathbf{b} \cdot \nabla \phi \times \nabla u \quad (2.1.9)$$

By assuming quasi-neutrality and singly charged ions, i.e. $n = n_e = n_i$, the density equation in physical units becomes:

$$\frac{\partial n}{\partial t} = -\frac{c}{B} [\phi, n] + \frac{2c}{eB} C(n T_e) - \frac{2cn}{B} C(\phi) - \nabla_{\parallel} (n v_{\parallel, e}) \quad (2.1.10)$$

The continuity equation, together with the other conservation equations, consitutes the drift-

reduced Braginskii's set of equations. That is:

$$\frac{\partial n}{\partial t} = -\frac{\rho_*^{-1}}{B}[\phi, n] + \frac{2}{B}[C(p_e) - nC(\phi)] - \nabla_{\parallel}(nv_{\parallel e}) + S_n + D_n \nabla_{\perp}^2 n \quad (2.1.11)$$

$$\frac{\partial v_{\parallel e}}{\partial t} = -\frac{\rho_*^{-1}}{B}[\phi, v_{\parallel e}] - v_{\parallel e} \nabla_{\parallel} v_{\parallel e} \quad (2.1.12)$$

$$\begin{aligned} & + \frac{m_i}{m_e} \left(\nu j_{\parallel} + \nabla_{\parallel} \phi - \frac{1}{n} \nabla_{\parallel} p_e - 0.71 \nabla_{\parallel} T_e \right) \\ & - \frac{2}{3n} \frac{m_i}{m_e} \nabla_{\parallel} G_e + D_{v_{\parallel e}} \nabla_{\perp}^2 v_{\parallel e} \\ \frac{\partial v_{\parallel i}}{\partial t} = & -\frac{\rho_*^{-1}}{B}[\phi, v_{\parallel i}] - v_{\parallel i} \nabla_{\parallel} v_{\parallel i} - \frac{1}{n} \nabla_{\parallel} (p_e + \tau p_i) \\ & - \frac{2}{3n} \nabla_{\parallel} G_i + D_{v_{\parallel i}} \nabla_{\perp}^2 v_{\parallel i} \end{aligned} \quad (2.1.13)$$

$$\begin{aligned} \frac{\partial T_e}{\partial t} = & -\frac{\rho_*^{-1}}{B}[\phi, T_e] - v_{\parallel e} \nabla_{\parallel} T_e + \frac{4}{3} \frac{T_e}{B} \left[\frac{1}{n} C(p_e) + \frac{5}{2} C(T_e) - C(\phi) \right] \\ & + \frac{2}{3} T_e \left[0.71 \nabla_{\parallel} v_{\parallel i} - 1.71 \nabla_{\parallel} v_{\parallel e} + 0.71 (v_{\parallel i} - v_{\parallel e}) \frac{\nabla_{\parallel} n}{n} \right] \\ & + S_{T_e} + \chi_{\perp, e} \nabla_{\perp}^2 T_e + \chi_{\parallel, e} \nabla_{\parallel}^2 T_e \end{aligned} \quad (2.1.14)$$

$$\begin{aligned} \frac{\partial T_i}{\partial t} = & -\frac{\rho_*^{-1}}{B}[\phi, T_i] - v_{\parallel i} \nabla_{\parallel} T_i + \frac{4}{3} \frac{T_i}{B} \left[C(T_e) + \frac{T_e}{n} C(n) - C(\phi) \right] \\ & + \frac{2}{3} T_i (v_{\parallel i} - v_{\parallel e}) \frac{\nabla_{\parallel} n}{n} - \frac{2}{3} T_i \nabla_{\parallel} v_{\parallel e} - \frac{10}{3} \tau \frac{T_i}{B} C(T_i) + S_{T_i} + D_{T_i} \nabla_{\perp}^2 T_i \end{aligned} \quad (2.1.15)$$

$$\begin{aligned} \frac{\partial \omega}{\partial t} = & -\frac{\rho_*^{-1}}{B}[\phi, \omega] - v_{\parallel i} \nabla_{\parallel} \omega + \frac{B^2}{n} \nabla_{\parallel} j_{\parallel} + \frac{2B}{n} C(p_e + \tau p_i) \\ & + \frac{B}{3n} C(G_i) + D_{\omega} \nabla_{\perp}^2 \omega \end{aligned} \quad (2.1.16)$$

$$\nabla_{\perp}^2 \phi = \omega - \tau \nabla_{\perp}^2 T_i \quad (2.1.17)$$

In Eqs. (2.1.11)-(2.1.17) all variables are dimensionless. In the following, we use a tilde to denote physical variables, unless specified otherwise. We define the plasma density $n = \tilde{n}/n_0$, the electron temperature $T_e = \tilde{T}_e/T_{e0}$, the ion temperature $T_i = \tilde{T}_i/T_{i0}$, the electro-static potential $\phi = e\tilde{\phi}/T_{e0}$, the electron parallel velocity $v_{\parallel e} = \tilde{v}_{\parallel e}/c_{s0}$, the ion parallel velocity $v_{\parallel i} = \tilde{v}_{\parallel i}/c_{s0}$ and the vorticity $\omega = \tilde{\omega} e \rho_{s0}^2 / T_{e0}$ with $n_0, T_{e0}, T_{i0}, c_{s0} = \sqrt{T_{e0}/m_i}$ and $\rho_{s0} = c_{s0}/\Omega_{ci}$ reference density, temperatures, sound velocity and ion sonic Larmor radius expressed in physical units. The electron and ion pressures are denoted as $p_e = nT_e$ and $p_i = nT_i$. The dimensionless current is $j_{\parallel} = n(v_{\parallel i} - v_{\parallel e})$. Time is defined as $t = \tilde{t} c_{s0}/R_0$, where R_0 is the major radius at magnetic axis, in physical units. The dimensionless parameters appearing in the model equations are: $\rho_* = \rho_{s0}/R_0$ (normalised ion sonic Larmor radius), $\nu = e^2 n_0 R_0 / (m_i c_{s0} \sigma_i)$ (normalised resistivity), $\tau = T_{i0}/T_{e0}$ (ion to electron temperature ratio).

Chapter 2. Physical model in toroidal coordinates

The gyroviscous terms $G_{e,i}$ in the parallel velocities and vorticity equations are defined as:

$$G_e = -\eta_{0,e} \left(2\nabla_{\parallel} v_{\parallel e} - \frac{C(p_e)}{Bn} + \frac{C(\phi)}{B} \right) \quad (2.1.18)$$

$$G_i = -\eta_{0,i} \left(2\nabla_{\parallel} v_{\parallel i} + \tau \frac{C(p_i)}{Bn} + \frac{C(\phi)}{B} \right) \quad (2.1.19)$$

with $\eta_{0,e,i}$ constant coefficients.

Some of the differential operators present in eqs (2.1.11)-(2.1.17) were already introduced in Eq. (2.1.9) in physical units. In dimensionless form they can be rewritten as:

$$\nabla_{\parallel} u = R_0 \tilde{\nabla}_{\parallel} u = R_0 \mathbf{b} \cdot \tilde{\nabla} u \quad (2.1.20)$$

$$\nabla_{\parallel}^2 u = R_0^2 \tilde{\nabla}_{\parallel}^2 u = R_0^2 \mathbf{b} \cdot \tilde{\nabla} (\mathbf{b} \cdot \tilde{\nabla} u) \quad (2.1.21)$$

$$[\phi, u] = \rho_{s0}^2 [\tilde{\phi}, \tilde{u}] = \rho_{s0}^2 \mathbf{b} \cdot (\tilde{\nabla} \phi \times \tilde{\nabla} u) \quad (2.1.22)$$

$$C(u) = R_0 \rho_{s0} \tilde{C}(u) = R_0 \rho_{s0} \frac{\tilde{B}}{2} \left(\tilde{\nabla} \times \frac{\mathbf{b}}{\tilde{B}} \right) \cdot \tilde{\nabla} u \quad (2.1.23)$$

$$\nabla_{\perp}^2 u = \rho_{s0}^2 \tilde{\nabla}_{\perp}^2 u = \rho_{s0}^2 \tilde{\nabla} \cdot ((\mathbf{b} \times \tilde{\nabla} u) \times \mathbf{b}) \quad (2.1.24)$$

The final form in Eqs. (2.1.20)-(2.1.24) presents the operator in terms of the equilibrium magnetic field $\tilde{\mathbf{B}}$, with \tilde{B} being its modulus and $\mathbf{b} = \tilde{\mathbf{B}}/\tilde{B}$ its normalised versor. The first equality, instead, relates the dimensionless form to the physical one, making use of the scale lengths R_0 and ρ_{s0} .

Making use of the definition of fluid quantities and differential operators in dimensionless form, we can relate the density equation derived from Maxwell's equation in physical units (see Eq. (2.1.10)) to its dimensionless form (see Eq. (2.1.11)):

$$\begin{aligned} \frac{\partial n}{\partial t} &= -\frac{\rho_{s0} R_0}{B} [\phi, \tilde{n}] + \frac{2\rho_{s0} R_0}{B} \tilde{C}(nT_e) - \frac{2n\rho_{s0} R_0}{B} \tilde{C}(\phi) - R_0 \tilde{\nabla}_{\parallel} (n v_{\parallel,e}) \\ &= -\frac{\rho_*^{-1}}{B} [\phi, n] + \frac{2}{B} C(nT_e) - \frac{2n}{B} C(\phi) - \nabla_{\parallel} (n v_{\parallel,e}) \end{aligned} \quad (2.1.25)$$

In the density and temperature equations (2.1.11), (2.1.14), (2.1.15), the additional source terms S_n and $S_{T_{e,i}}$ are introduced to mimic the outflow of plasma and heat from the core. Furthermore, small numerical diffusion terms of the type $D_f \nabla_{\perp}^2 f$ are added for numerical stability.

We note that the drift-reduced Braginskii's equations were first implemented in the GBS code in limited configuration in the electrostatic, cold-ion limit, assuming no interaction of the plasma with the neutrals, as described in Ref. [26]. In the following years, the hot ion physics was introduced by Masetto *et al.* [27], electromagnetic effects by Halpern *et al.* [28] and coupling with the neutral dynamics by Wersal *et al.* [29]. The most complete model used for limited simulations is summarised in the paper by Halpern *et al.* [23]. The version of the drift-reduced Braginskii's equations considered in the present paper, summarised in Eqs. (2.1.11)-(2.1.17), does not include coupling with neutrals, nor electromagnetic effects, but does include hot ions. The Boussinesq approximation in the evaluation of the divergence

of the polarisation current is used to reduce the cost. Finally, we assumed $\nabla \cdot \mathbf{b} \simeq 0$ when computing the parallel advection terms.

2.2 Differential operators in toroidal coordinates

In the previous section, we have defined the dimensionless operators $\nabla_{\parallel}(u)$, $\nabla_{\parallel}^2(u)$, $C(u)$, $[\phi, u]$ and ∇_{\perp}^2 in terms of the equilibrium magnetic field. In this section, we project them on toroidal coordinates and we simplify them under the large aspect ratio, $R_0/a \gg 1$, and large safety factor assumptions, $q > 1$.

In order to obtain the simplified expression, we proceed as follows. We first comment on the typical scale lengths of the physical operators (e.g. $\tilde{\nabla}_{\parallel} u = 1/R_0$, $\tilde{\nabla}_{\perp} \sim 1/l_{\perp}$) in Sec. 2.2.1. Then, after rigorously defining the toroidal coordinate system and the magnetic field covariant and contravariant form in Sec. 2.2.2, 2.2.3, we project the differential operators on the toroidal basis (Sec. 2.2.4). Since the coordinate system and magnetic field are not aligned, the resulting expressions involve derivatives in all three directions, mixing poloidal, radial, and toroidal scale lengths of magnetic field and evolved quantities u . Hence, in Sec. 2.2.5 we propose an ordering for the magnetic field components, by identifying the typical scale lengths of the poloidal flux derivatives (e.g. $\partial_{\tilde{r}} \psi \sim 1/a$) and in Sec. 2.2.6 we justify the assumptions on the u derivatives in toroidal coordinates (e.g. $\partial_{\tilde{r}} u \sim 1/l_{\perp}$). Having determined the scale lengths of differential operators, magnetic field and u derivatives in toroidal coordinates, we can order them using the small parameters $\rho_* = \rho_{s0}/R_0$, $\sigma = l_{\perp}/R_0$, and $\varepsilon = a/R_0$. The final simplification neglects terms that are order one or higher in ρ_* , σ and ε .

2.2.1 Physical operators scale lengths

The scale lengths ρ_{s0} and R_0 that we used to write the dimensionless form of the operators in Eqs. (2.1.20)-(2.1.24) do not necessarily correspond to the typical ones. Or, otherwise said, we proposed a dimensionless form for the operators and not a normalised one. This in particular holds true for the perpendicular scale length. We used ρ_{s0} for the nondimensionalisation, but the perpendicular gradients have to be on scale lengths larger than the Larmor radius for the drift-reduced approximation to hold. We call $l_{\perp} > \rho_{s0}$ the typical perpendicular gradient scale length (in physical units) and $l_{\parallel} \sim 2\pi q R_0 \sim R_0$ the parallel one.

While it is straightforward to identify $\tilde{\nabla}_{\parallel}$ and $\tilde{\nabla}_{\parallel}^2$ as parallel and $\tilde{\nabla}_{\perp}^2$ as perpendicular operators, it is less intuitive doing so for the curvature gradient or the Poisson brackets. They were first introduced in Eqs. (2.1.7) and (2.1.8) to account for the density transport due to $\mathbf{E} \times \mathbf{B}$ and diamagnetic drifts, which are perpendicular to the magnetic field by definition (see Eqs. (2.1.4) and (2.1.5)). The curvature operator, though, contains a derivative that acts on the fluid quantity u and one that acts on the magnetic field, $\tilde{\nabla} \times (\mathbf{b}/\tilde{B})$ (see Eq. (2.1.23)). This latter corresponds to the curvature of the magnetic field which is proportional $1/R_0$. In fact, the curvature of the magnetic field is defined as $\mathbf{k} = \mathbf{b} \cdot \nabla \mathbf{b}$ and, when the local current density is negligible, $\tilde{\nabla} \times \tilde{\mathbf{B}} = 0$ and $\tilde{\nabla} \times (\mathbf{b}/\tilde{B}) = 2\mathbf{b} \times \mathbf{k}/\tilde{B}$. Incidentally, with this we have also proven that the derivative on u in $\tilde{C}(u)$ acts orthogonal to the magnetic field, since $(2\mathbf{b} \times \mathbf{k}/\tilde{B}) \perp \mathbf{b}$.

Chapter 2. Physical model in toroidal coordinates

To conclude, the typical scale lengths of the physical operators are,

$$\tilde{\nabla}_{\parallel} u \sim \frac{1}{R_0}, \quad \tilde{\nabla}_{\parallel}^2 u \sim \frac{1}{R_0^2}, \quad \tilde{C}(u) \sim \frac{1}{R_0 l_{\perp}}, \quad [\tilde{\phi}, u] \sim \frac{1}{l_{\perp}^2}, \quad \tilde{\nabla}_{\perp}^2 u \sim \frac{1}{l_{\perp}^2} \quad (2.2.1)$$

and, analogously, for the dimensionless form,

$$\nabla_{\parallel} u \sim 1, \quad \nabla_{\parallel}^2 u \sim 1, \quad C(u) \sim \frac{\rho_{s0}}{l_{\perp}} = \rho_* \sigma^{-1}, \quad [\phi, u] \sim \frac{\rho_{s0}^2}{l_{\perp}^2} = \rho_*^2 \sigma^{-2}, \quad \nabla_{\perp}^2 u \sim \frac{\rho_{s0}^2}{l_{\perp}^2} = \rho_*^2 \sigma^{-2} \quad (2.2.2)$$

Note that using l_{\perp} instead of ρ_{s0} when defining the dimensionless form in Eqs. (2.1.20)-(2.1.24) would have indeed led to operators of order one, but l_{\perp} , unlike ρ_{s0} , can not be determined starting from plasma quantities such as the plasma electron temperature, ion mass and strenght of the magnetic field. l_{\perp} corresponds to the turbulence scale in the perpendicular direction and can not be estimated a-priori, nonetheless we expect $\rho_{s0} < l_{\perp} < R_0$.

2.2.2 Toroidal coordinates

Before proceeding with the ordering, let us rigorously define the toroidal coordinate basis and its properties. The toroidal coordinates $(\tilde{r}, \theta, \varphi)$ can be defined by a mapping to the Cartesian coordinates $(\tilde{x}, \tilde{y}, \tilde{z}) = \mathbf{G}(\tilde{r}, \theta, \varphi)$:

$$\begin{aligned} \tilde{x} &= \tilde{R} \cos \varphi = (R_0 - \tilde{r} \cos \theta) \cos \varphi \\ \tilde{y} &= \tilde{R} \sin \varphi = (R_0 - \tilde{r} \cos \theta) \sin \varphi \\ \tilde{z} &= Z_0 + \tilde{r} \sin \theta \end{aligned} \quad (2.2.3)$$

with (R_0, Z_0) magnetic axis position on a poloidal plane and R major radius. The covariant coordinate basis [30] $(\mathbf{e}_{\tilde{r}}, \mathbf{e}_{\theta}, \mathbf{e}_{\varphi})$ is defined as follows:

$$\begin{aligned} \mathbf{e}_{\tilde{r}} &= \frac{\partial \mathbf{G}}{\partial \tilde{r}} = (-\cos \theta \cos \varphi, -\cos \theta \sin \varphi, \sin \theta) \\ \mathbf{e}_{\theta} &= \frac{\partial \mathbf{G}}{\partial \theta} = \tilde{r}(\sin \theta \cos \varphi, \sin \theta \sin \varphi, \cos \theta) \\ \mathbf{e}_{\varphi} &= \frac{\partial \mathbf{G}}{\partial \varphi} = \tilde{R}(-\sin \varphi, \cos \varphi, 0) \end{aligned}$$

The contravariant basis $(\mathbf{e}^{\tilde{r}}, \mathbf{e}^{\theta}, \mathbf{e}^{\varphi}) = (\nabla \tilde{r}, \nabla \theta, \nabla \varphi)$ is instead defined as [30]:

$$\mathbf{e}^i = \nabla i = \frac{\mathbf{e}_j \times \mathbf{e}_k}{\mathbf{e}_i \cdot \mathbf{e}_j \times \mathbf{e}_k} = \frac{\mathbf{e}_i}{\|\mathbf{e}_i\|^2}$$

since the toroidal coordinates orthogonal. Furthermore, due to the orthogonality of the coordinate system,

$$\begin{aligned} \mathbf{e}_{\tilde{r}} // \nabla \tilde{r}, \quad ||\mathbf{e}_{\tilde{r}}|| = 1, \quad ||\nabla \tilde{r}|| = 1, \\ \mathbf{e}_{\theta} // \nabla \theta, \quad ||\mathbf{e}_{\theta}|| = \tilde{r}, \quad ||\nabla \theta|| = \frac{1}{\tilde{r}} \\ \mathbf{e}_{\varphi} // \nabla \varphi, \quad ||\mathbf{e}_{\varphi}|| = \tilde{R}, \quad ||\nabla \varphi|| = \frac{1}{\tilde{R}} \end{aligned} \quad (2.2.4)$$

Finally, the Jacobian of the transformation \mathbf{G} is $\tilde{J} = (\nabla \tilde{r} \cdot \nabla \theta \times \nabla \varphi)^{-1} = \tilde{r} \tilde{R}$.

2.2.3 Magnetic field in toroidal coordinates

We express the axisymmetric tokamak magnetic field in the form

$$\tilde{\mathbf{B}} = F(\tilde{\psi}) \tilde{\nabla} \varphi + \tilde{\nabla} \varphi \times \tilde{\nabla} \tilde{\psi}(\tilde{r}, \theta) \quad (2.2.5)$$

where, for simplicity, we assume $F = R_0 B_0$, implying that the toroidal magnetic field varies as $1/\tilde{R}$. The expression of the magnetic field in contravariant components, $\tilde{\mathbf{B}} = \tilde{B}^i \mathbf{e}_i$, reads as

$$\tilde{\mathbf{B}} = \frac{B_0 R_0}{\tilde{R}^2} \mathbf{e}_{\varphi} - \frac{1}{\tilde{r} \tilde{R}} \partial_{\theta} \tilde{\psi} \mathbf{e}_{\tilde{r}} + \frac{1}{\tilde{r} \tilde{R}} \partial_{\tilde{r}} \tilde{\psi} \mathbf{e}_{\theta} \quad (2.2.6)$$

that can be obtained applying the relation $\tilde{B}^i = \tilde{\mathbf{B}} \cdot \nabla i$ to the magnetic field expression in Eq. (2.2.5), and using the information on the basis vectors in Eqs. (2.2.4). In covariant components, $\tilde{\mathbf{B}} = \tilde{B}_i \mathbf{e}^i$, one obtains

$$\tilde{\mathbf{B}} = B_0 R_0 \tilde{\nabla} \varphi - \frac{1}{\tilde{r} \tilde{R}} \partial_{\theta} \tilde{\psi} \tilde{\nabla} \tilde{r} + \frac{\tilde{r}}{\tilde{R}} \partial_{\tilde{r}} \tilde{\psi} \tilde{\nabla} \theta \quad (2.2.7)$$

2.2.4 Operators in toroidal coordinates

Eqs. (2.1.20)-(2.2.6) provide all the elements to evaluate the expressions of the differential operators in toroidal coordinates. In physical units these are (note the use of Einstein notation)

$$\begin{aligned}\tilde{\nabla}_{\parallel} u &= \frac{\tilde{\mathbf{B}}}{\tilde{B}} \cdot \left(\nabla_{\tilde{r}} \frac{\partial u}{\partial \tilde{r}} + \nabla_{\theta} \frac{\partial u}{\partial \theta} + \nabla_{\varphi} \frac{\partial u}{\partial \varphi} \right) \\ &= \frac{1}{\tilde{B}} \left(\tilde{B}^{\tilde{r}} \frac{\partial u}{\partial \tilde{r}} + \tilde{B}^{\theta} \frac{\partial u}{\partial \theta} + \tilde{B}^{\varphi} \frac{\partial u}{\partial \varphi} \right)\end{aligned}\quad (2.2.8)$$

$$\tilde{\nabla}_{\parallel}^2 u = \tilde{\nabla}_{\parallel} (\tilde{\nabla}_{\parallel} u) = \frac{\tilde{B}^i}{\tilde{B}} \frac{\partial}{\partial \tilde{c}^i} \left(\frac{\tilde{B}^j}{\tilde{B}} \frac{\partial u}{\partial \tilde{c}^j} \right) \quad (2.2.9)$$

$$\begin{aligned}\tilde{[\phi, u]} &= \frac{\tilde{\mathbf{B}}}{\tilde{B}} \cdot \left[\left(\frac{\partial \phi}{\partial \tilde{r}} \nabla_{\tilde{r}} + \frac{\partial \phi}{\partial \theta} \nabla_{\theta} + \frac{\partial \phi}{\partial \varphi} \nabla_{\varphi} \right) \times \left(\frac{\partial u}{\partial \tilde{r}} \nabla_{\tilde{r}} + \frac{\partial u}{\partial \theta} \nabla_{\theta} + \frac{\partial u}{\partial \varphi} \nabla_{\varphi} \right) \right] \\ &= \frac{1}{\tilde{B} \tilde{J}} (\tilde{B}_{\varphi} [\phi, f]_{\tilde{r}, \theta} + \tilde{B}_{\tilde{r}} [\phi, u]_{\theta, \varphi} + \tilde{B}_{\theta} [\phi, u]_{\varphi, \tilde{r}})\end{aligned}\quad (2.2.10)$$

$$\begin{aligned}\tilde{C}(u) &= \frac{1}{2 \tilde{J} \tilde{B}} \left[-\frac{\tilde{B}_{\varphi}}{\tilde{B}^2} \partial_{\theta} \tilde{B}^2 \frac{\partial u}{\partial \tilde{r}} + \frac{\tilde{B}_{\varphi}}{\tilde{B}^2} \partial_{\tilde{r}} \tilde{B}^2 \frac{\partial u}{\partial \theta} \right. \\ &\quad \left. + \left(\partial_{\tilde{r}} \tilde{B}_{\theta} - \partial_{\theta} \tilde{B}_{\tilde{r}} - \frac{\tilde{B}_{\theta}}{\tilde{B}^2} \partial_{\tilde{r}} \tilde{B}^2 + \frac{\tilde{B}_{\tilde{r}}}{\tilde{B}^2} \partial_{\theta} \tilde{B}^2 \right) \frac{\partial u}{\partial \varphi} \right]\end{aligned}\quad (2.2.11)$$

$$\begin{aligned}\tilde{\nabla}_{\perp}^2 u &= \tilde{\nabla} \cdot \tilde{\nabla}_{\perp} u = \frac{1}{\tilde{J}} \frac{\partial}{\partial \tilde{c}^k} \left(\tilde{J} (\nabla_{\perp} u)^k \right) \\ &= \frac{1}{\tilde{J}} \sum_k \frac{\partial}{\partial \tilde{c}^k} \left(\frac{\tilde{J}}{\tilde{B}^2} \|\mathbf{e}^k\|^2 \epsilon_{ijk} \epsilon^{lni} \tilde{B}_l \tilde{B}^j \frac{\partial u}{\partial \tilde{c}^n} \right)\end{aligned}\quad (2.2.12)$$

where we define $[\phi, f]_{x,y} := \partial_x \phi \partial_y f - \partial_y \phi \partial_x f$, \tilde{c}^i indicates one of the coordinates $(\tilde{r}, \theta, \varphi)$, and ϵ^{ijk} is the Levi-Civita symbol. \tilde{B} is the modulus of $\tilde{\mathbf{B}}$, computed as $\tilde{B} = \sqrt{\tilde{B}_i \tilde{B}^i}$.

The derivation of the operators above is relatively straightforward but for the perpendicular Laplacian in Eq. (2.2.12). Starting from Eq. (2.1.24) the perpendicular Laplacian in physical units reads:

$$\tilde{\nabla}_{\perp}^2 u := \tilde{\nabla} \cdot \tilde{\nabla}_{\perp} u = \tilde{\nabla} \cdot \left[\frac{1}{\tilde{B}^2} (\tilde{\mathbf{B}} \times \tilde{\nabla} u) \times \tilde{\mathbf{B}} \right]$$

Let us start by computing the innermost cross product:

$$\tilde{\mathbf{B}} \times \tilde{\nabla} u = \frac{1}{\tilde{J}} \epsilon^{ijk} \tilde{B}_i \frac{\partial u}{\partial \tilde{c}^j} \mathbf{e}_k$$

Now the perpendicular gradient can be computed

$$\begin{aligned}\tilde{\nabla}_{\perp} u &= \frac{1}{\tilde{B}^2} (\tilde{\mathbf{B}} \times \tilde{\nabla} u) \times \tilde{\mathbf{B}} = \frac{1}{\tilde{B}^2} \tilde{J} \epsilon_{ijk} (\tilde{\mathbf{B}} \times \tilde{\nabla} u)^i \tilde{B}^j \mathbf{e}^k \\ &= \frac{1}{\tilde{B}^2} \epsilon_{ijk} \epsilon^{lni} \tilde{B}_l \tilde{B}^j \frac{\partial u}{\partial \tilde{c}^n} \mathbf{e}^k\end{aligned}\quad (2.2.13)$$

Finally, we compute the divergence of the perpendicular gradient

$$\begin{aligned}\tilde{\nabla}_\perp^2 u &:= \tilde{\nabla} \cdot \tilde{\nabla}_\perp u = \frac{1}{\tilde{J}} \frac{\partial}{\partial \tilde{c}^k} \left(\tilde{J} (\nabla_\perp u)^k \right) \\ &= \frac{1}{\tilde{J}} \sum_k \frac{\partial}{\partial \tilde{c}^k} \left(\frac{\tilde{J}}{\tilde{B}^2} \|\mathbf{e}^k\|^2 \epsilon_{ijk} \epsilon^{lni} \tilde{B}_l \tilde{B}^j \frac{\partial u}{\partial \tilde{c}^n} \right)\end{aligned}\quad (2.2.14)$$

Note that all operators involve derivatives in all three directions (r, θ, φ) , since our coordinate system is not aligned to the magnetic field.

2.2.5 Ordering of the magnetic field components

In order to simplify the expression of the operators in Eqs. (2.2.8)- (2.2.12), we here investigate the magnitude of magnetic field components appearing therein. The scaling of the toroidal component of the magnetic field is immediate, as we chose it to vary as $1/\tilde{R}$ see Eq. (2.2.5). The radial and poloidal components, on the other hand, are determined by the poloidal flux, for which we propose the following ordering

$$\frac{\partial \psi}{\partial \tilde{r}} \sim \frac{1}{a}, \quad \frac{1}{\tilde{r}} \frac{\partial \psi}{\partial \theta} \sim \frac{1}{a}, \quad (2.2.15)$$

with $\partial_\varphi \psi = 0$ because of axisymmetry. The dimensionless poloidal flux ψ is chosen to be of order one, $\tilde{\psi} \sim a^2 |B_0|$ and $\psi = \tilde{\psi} / (a^2 |B_0|)$. Let us show that these assumptions are valid in the SOL of a large aspect ratio tokamak. For simplicity, we consider the case of circular flux surfaces, for which $\psi = \psi(r)$ and $\partial_\theta \psi = 0$. In this case the safety factor reads

$$q := \frac{\tilde{r}}{\tilde{R}} \frac{|\tilde{B}_\varphi \tilde{\nabla} \varphi|}{|\tilde{B}_\theta \tilde{\nabla} \theta|} = \left| \frac{\tilde{B}^\varphi}{\tilde{B}^\theta} \right| = \frac{|B_0| \frac{R_0}{\tilde{R}^2}}{\left| \frac{B_0 a^2}{\tilde{r} \tilde{R}} \partial_{\tilde{r}} \psi \right|} = \frac{\tilde{r}}{a} \frac{R_0}{\tilde{R}} \frac{1}{|a \partial_{\tilde{r}} \psi|} \quad (2.2.16)$$

where we used properties of covariant and contravariant basis in Eq. (2.2.4) and the magnetic field contravariant components in Eq.-(2.2.6). In Eq. (2.2.16), $\tilde{R} = R_0 + \epsilon \tilde{r} \cos \theta$ evaluated at $\cos \theta = \pm 1$ gives an estimate for $\partial_{\tilde{r}} \psi$

$$\frac{1}{q} \frac{\tilde{r}}{a} \frac{1}{1 - \epsilon \tilde{r}/a} < a \left| \frac{\partial \psi}{\partial \tilde{r}} \right| < \frac{1}{q} \frac{\tilde{r}}{a} \frac{1}{1 + \epsilon \tilde{r}/a} \quad (2.2.17)$$

Since $\tilde{r}/a \sim 1$ in the SOL and $q > 1$, if the inverse aspect ratio ϵ is small, then the extremes in the above inequality are order 1 and the assumption on ψ gradient scale lengths in Eq. (2.2.15) are valid.

Under this assumption, the ordering of the magnetic field in covariant components (from

Eq. (2.2.7)) is

$$\begin{aligned}\tilde{\mathbf{B}} &= - \underbrace{\frac{1}{\tilde{r}\tilde{R}}}_{a^{-1}R_0^{-1}} \underbrace{\partial_\theta \tilde{\psi}}_{a^2 B_0} \underbrace{\nabla \tilde{r}}_1 + \underbrace{\frac{\tilde{r}}{\tilde{R}}}_{aR_0^{-1}} \underbrace{\partial_{\tilde{r}} \tilde{\psi}}_{aB_0} \underbrace{\nabla \theta}_{a^{-1}} + \underbrace{B_0 R_0}_{R_0 B_0} \underbrace{\nabla \varphi}_{R_0^{-1}} \\ &= \underbrace{\tilde{B}_r}_{aR_0^{-1}B_0} \nabla \tilde{r} + \underbrace{\tilde{B}_\theta}_{a^2 R_0^{-1}B_0} \nabla \theta + \underbrace{\tilde{B}_\varphi}_{R_0 B_0} \nabla \varphi\end{aligned}\quad (2.2.18)$$

while, in contravariant components (from Eq. (2.2.6)):

$$\begin{aligned}\tilde{\mathbf{B}} &= - \underbrace{\frac{1}{\tilde{r}\tilde{R}}}_{a^{-1}R_0^{-1}} \underbrace{\partial_\theta \tilde{\psi}}_{a^2 B_0} \underbrace{\mathbf{e}_{\tilde{r}}}_1 + \underbrace{\frac{1}{\tilde{r}\tilde{R}}}_{a^{-1}R_0^{-1}} \underbrace{\partial_{\tilde{r}} \tilde{\psi}}_{aB_0} \underbrace{\mathbf{e}_\theta}_a + \underbrace{\frac{B_0 R_0}{\tilde{R}^2}}_{R_0^{-1}B_0} \underbrace{\mathbf{e}_\varphi}_{R_0} \\ &= \underbrace{\tilde{B}^r}_{aR_0^{-1}B_0} \mathbf{e}_{\tilde{r}} + \underbrace{\tilde{B}^\theta}_{R_0^{-1}B_0} \mathbf{e}_\theta + \underbrace{\tilde{B}^\varphi}_{R_0^{-1}B_0} \mathbf{e}_\varphi\end{aligned}\quad (2.2.19)$$

where we used $\tilde{\psi} \sim a^2|B_0|$. The modulus of $\tilde{\mathbf{B}}$ also appears in the operators expressions:

$$\tilde{B}^2 = \tilde{B}_i \tilde{B}^i = \underbrace{\frac{B_0^2 R_0^2}{\tilde{R}^2}}_{B_0^2} + \underbrace{\frac{1}{\tilde{r}^2 \tilde{R}^2} \partial_\theta \tilde{\psi}^2}_{a^2 R_0^{-2} B_0^2} + \underbrace{\frac{1}{\tilde{R}^2} \partial_{\tilde{r}} \tilde{\psi}^2}_{a^2 R_0^{-2} B_0^2} = \frac{B_0^2 R_0^2}{\tilde{R}^2} + O(\varepsilon^2)\quad (2.2.20)$$

In addition, the derivatives of the magnetic field can be ordered as follows:

$$\begin{aligned}\partial_{\tilde{r}} \tilde{B}^2 &= \frac{2}{\tilde{R}} \cos \theta \tilde{B}^2 + \left[-\frac{2}{\tilde{R}^2 \tilde{r}^3} \partial_\theta \tilde{\psi}^2 + \frac{1}{\tilde{R}^2 \tilde{r}^2} \partial_{\tilde{r}} (\partial_\theta \tilde{\psi})^2 + \frac{1}{\tilde{R}^2} \partial_{\tilde{r}} (\partial_{\tilde{r}} \tilde{\psi})^2 \right] \sim \frac{B_0^2}{R_0} \\ \partial_\theta \tilde{B}^2 &= -\frac{2}{\tilde{R}} \tilde{r} \sin \theta \tilde{B}^2 + \left[\frac{1}{\tilde{R}^2 \tilde{r}^2} \partial_\theta (\partial_\theta \tilde{\psi})^2 + \frac{1}{\tilde{R}^2} \partial_\theta (\partial_{\tilde{r}} \tilde{\psi})^2 \right] \sim \frac{a}{R_0} B_0^2 \\ \partial_\theta \tilde{B}^\theta &= \frac{1}{\tilde{r}\tilde{R}} \partial_{\tilde{r}\theta}^2 \tilde{\psi} - \left[\frac{1}{\tilde{R}^2} \sin \theta \partial_{\tilde{r}} \tilde{\psi} \right] \sim \frac{B_0}{R_0} \\ \partial_\theta \tilde{B}_\theta &= \frac{\tilde{r}}{\tilde{R}} \partial_{\tilde{r}\theta}^2 \tilde{\psi} - \left[\frac{r^2}{\tilde{R}^2} \sin \theta \partial_{\tilde{r}} \tilde{\psi} \right] \sim \frac{a^2 B_0}{R_0} \\ \partial_{\tilde{r}} \tilde{B}_\theta &= \frac{1}{\tilde{R}} \partial_{\tilde{r}} \tilde{\psi} + \frac{\tilde{r}}{\tilde{R}} \partial_{\tilde{r}\tilde{r}}^2 \tilde{\psi} + \left[\frac{\tilde{r}}{\tilde{R}^2} \cos \theta \partial_{\tilde{r}} \tilde{\psi} \right] \sim \frac{a}{R_0} B_0 \\ \partial_{\tilde{r}} \tilde{B}^\theta &= -\frac{1}{\tilde{r}^2 \tilde{R}} \partial_{\tilde{r}} \tilde{\psi} + \frac{1}{\tilde{r}\tilde{R}} \partial_{\tilde{r}\tilde{r}}^2 \tilde{\psi} + \left[\frac{\cos \theta}{\tilde{r}\tilde{R}^2} \partial_r \tilde{\psi} \right] \sim \frac{B_0}{aR_0} \\ \partial_\theta \tilde{B}_r &= \partial_\theta \tilde{B}^r = -\frac{1}{\tilde{r}\tilde{R}} \partial_{\theta\theta}^2 \tilde{\psi} - \left[\frac{\sin \theta}{\tilde{R}^2} \partial_\theta \tilde{\psi} \right] \sim \frac{a}{R_0} B_0 \\ \partial_{\tilde{r}} \tilde{B}_r &= \partial_{\tilde{r}} \tilde{B}^r = \frac{1}{\tilde{r}^2 \tilde{R}} \partial_\theta \tilde{\psi} - \frac{1}{\tilde{r}\tilde{R}} \partial_{\tilde{r}\theta}^2 \tilde{\psi} - \left[\frac{\cos \theta}{\tilde{r}\tilde{R}^2} \partial_\theta \tilde{\psi} \right] \sim \frac{B_0}{R_0}\end{aligned}\quad (2.2.21)$$

with the terms inside the square brackets being order a/R_0 higher than the leading order ones. To conclude the ordering of the magnetic field, let us show that $R_0 \tilde{\nabla} \cdot \mathbf{b}$ is order ε , and we can

indeed neglect it in the drift-reduced Braginskii's equations (as mentioned in Sec. 2.1):

$$\begin{aligned}
 R_0 \tilde{\nabla} \cdot \mathbf{b} &= \frac{R_0}{\tilde{J}} \left(\partial_\theta (\tilde{J} \tilde{B}^\theta / \tilde{B}) + \partial_{\tilde{r}} (\tilde{J} \tilde{B}^r / \tilde{B}) \right) = \frac{R_0}{\tilde{r} \tilde{R}} \left(\partial_\theta (\partial_{\tilde{r}} \tilde{\psi} / \tilde{B}) - \partial_{\tilde{r}} (\partial_\theta \tilde{\psi} / \tilde{B}) \right) \\
 &= \underbrace{\frac{R_0}{\tilde{r} \tilde{R}} \frac{\partial_{\tilde{r}} \tilde{\psi} \partial_\theta \tilde{B}^2}{2 \tilde{B}^3}}_{a R_0^{-1}} - \underbrace{\frac{R_0}{\tilde{r} \tilde{R}} \frac{\partial_\theta \tilde{\psi} \partial_{\tilde{r}} \tilde{B}^2}{2 \tilde{B}^3}}_{a R_0^{-1}} \sim \varepsilon
 \end{aligned} \tag{2.2.22}$$

where we used the relations $\partial_{\tilde{r}} \tilde{B} = \partial_{\tilde{r}} \tilde{B}^2 / (2 \tilde{B})$ and $\partial_\theta \tilde{B} = \partial_\theta \tilde{B}^2 / (2 \tilde{B})$.

2.2.6 Assumption on plasma quantities derivatives in toroidal coordinates

The last step before proceeding with the ordering and simplification of the operators expressions (2.2.8)-(2.2.12), is to identify the scale lengths of the derivatives of the evolved quantities u in toroidal coordinates. Intuitively, if the safety factor and the tokamak aspect ratio are large, the perpendicular and the poloidal plane almost coincide. Or, analogously, the projection of the perpendicular operators in the toroidal direction is negligible and therefore the toroidal derivative only appears in the parallel gradients. Following this intuition we have:

$$\frac{\partial u}{\partial \tilde{r}} \sim \frac{1}{l_\perp}, \quad \frac{1}{\tilde{r}} \frac{\partial u}{\partial \theta} \sim \frac{1}{l_\perp}, \quad \frac{1}{\tilde{R}} \frac{\partial u}{\partial \varphi} \sim \frac{1}{R_0} \tag{2.2.23}$$

where l_\perp and R_0 are the typical scale lengths of perpendicular and parallel dynamics respectively (see Sec. 2.2.1). Let us prove that our intuition is correct by comparing the projection of the perpendicular operator in the poloidal and toroidal direction. For simplicity we consider a circular equilibrium ($B_r = 0$), using the definition of $\tilde{\nabla}_\perp$ in Eq. (2.2.13) as well as the formula for the safety factor q in eq (2.2.16) we have

$$\frac{(\tilde{\nabla}_\perp u \cdot \mathbf{e}_\varphi) \tilde{\nabla} \varphi}{(\tilde{\nabla}_\perp u \cdot \mathbf{e}_\theta) \tilde{\nabla} \theta} = \frac{+\tilde{B}_\theta \tilde{B}^\theta \partial_\varphi u - \tilde{B}_\varphi \tilde{B}^\theta \partial_\theta u}{-\tilde{B}_\theta \tilde{B}^\varphi \partial_\varphi u + \tilde{B}_\varphi \tilde{B}^\varphi \partial_\theta u} \frac{\tilde{\nabla} \varphi}{\tilde{\nabla} \theta} = -\frac{\tilde{B}^\theta \tilde{\nabla} \varphi}{\tilde{B}^\varphi \tilde{\nabla} \theta} = \frac{1}{q} \frac{\tilde{r}}{\tilde{R}} \sim \frac{\varepsilon}{q} \tag{2.2.24}$$

where the numerator and denominator correspond to the component of ∇_\perp in the toroidal direction and poloidal direction, respectively. If ε is small and q is large the toroidal component is indeed negligible in the perpendicular dynamics and the typical length scale of a toroidal derivative will be $1/R_0$.

2.2.7 Simplified operator expressions

We have presented order of magnitude scalings for gradients of the fluctuating quantities u and magnetic field, both in the poloidal plane and toroidal direction (Eqs. (2.2.23) and (2.2.15)). The validity of these scalings increases with safety factor q and aspect ratio R_0/a .

In this section, we will piece together the work done in sections 2.2.1-2.2.6 to simplify the differential operators expressions in Sec. 2.2.4. As mentioned, we will neglect all term that are

Chapter 2. Physical model in toroidal coordinates

order ρ_* , σ or ε , and retain only order one terms, with:

$$\frac{\rho_{s0}}{R_0} = \rho_* \leq \frac{l_\perp}{R_0} = \sigma \leq \frac{a}{R_0} = \varepsilon$$

Neglecting order ε terms corresponds to considering the large aspect ratio approximation, while neglecting order σ and ρ_* terms is justified because l_\perp and ρ_{s0} are much smaller than the machine major radius R_0 .

As we have seen in section 2.2.1 parallel and perpendicular operators have intrinsically different magnitude, here we want to keep the terms that are order one in the operators normalised form, for instance, since $\tilde{\nabla}_\perp^2 \sim 1/l_\perp^2$ we want to keep the terms that are smaller than $1/l_\perp^2$, while in the case of $\tilde{\nabla}_\parallel$ we would neglect terms smaller $1/R_0$. Hence, to permit consistent treatment of the operators, we will order them in normalised form:

$$\nabla_\parallel u \sim 1, \quad \tilde{\nabla}_\parallel^2 u \sim 1, \quad \sigma \rho_*^{-1} C(u) \sim 1, \quad \sigma^2 \rho_*^{-2} [\phi, u] \sim 1, \quad \sigma^2 \rho_*^{-2} \nabla_\perp^2 u \sim 1 \quad (2.2.25)$$

(re-arranged from Eq. (2.2.2)) and keep only terms of order 1 or higher in the resulting expressions.

From Eqs. (2.1.20), (2.2.8), (2.2.18) and (2.2.20) the dimensionless expression for the parallel gradient can be ordered as:

$$\nabla_\parallel u = R_0 \underbrace{\frac{\tilde{B}^r}{\tilde{B}} \frac{\partial u}{\partial \tilde{r}}}_{\substack{aR_0^{-1} \\ l_p^{-1}}} + R_0 \underbrace{\frac{\tilde{B}^\theta}{\tilde{B}} \frac{\partial u}{\partial \theta}}_{\substack{R_0^{-1} \\ l_p^{-1} a}} + R_0 \underbrace{\frac{\tilde{B}^\varphi}{\tilde{B}} \frac{\partial u}{\partial \varphi}}_{\substack{R_0^{-1} \\ 1}}.$$

Since $a > l_\perp$ it follows that $\varepsilon \sigma^{-1} > 1$. Therefore the poloidal components are not negligible and it is not possible to simplify the expression of the parallel operator.

To simplify the expression for ∇_\parallel^2 , we need to use the ordering of the derivatives of the magnetic field in Eqs. (2.2.21), as well as the operator expression in physical and dimensionless units (Eqs. (2.2.9) and (2.1.21)), and the ordering of the contravariant components for $\tilde{\mathbf{B}}$ in

Eq. (2.2.19):

$$\begin{aligned}
 \nabla_{\parallel}^2 u = & \underbrace{\left(R_0 \frac{\tilde{B}^\varphi}{\tilde{B}} \right)^2}_{1} \underbrace{\frac{\partial^2 u}{\partial \varphi^2}}_1 + \underbrace{\left(R_0 \frac{\tilde{B}^r}{\tilde{B}} \right)^2}_{a^2} \underbrace{\frac{\partial^2 u}{\partial \tilde{r}^2}}_{l_{\perp}^{-2}} + \underbrace{\left(R_0 \frac{\tilde{B}^\theta}{\tilde{B}} \right)^2}_{1} \underbrace{\frac{\partial^2 u}{\partial \theta^2}}_{l_{\perp}^{-2} a^2} \\
 & + 2 R_0^2 \underbrace{\frac{\tilde{B}^\varphi \tilde{B}^\theta}{\tilde{B}^2}}_1 \underbrace{\frac{\partial^2 u}{\partial \varphi \partial \theta}}_{l_{\perp}^{-1} a} + 2 R_0^2 \underbrace{\frac{\tilde{B}^\varphi \tilde{B}^r}{\tilde{B}^2}}_a \underbrace{\frac{\partial^2 u}{\partial \varphi \partial r}}_{l_{\perp}^{-1}} + 2 R_0^2 \underbrace{\frac{\tilde{B}^r \tilde{B}^\theta}{\tilde{B}^2}}_a \underbrace{\frac{\partial^2 u}{\partial \theta \partial r}}_{l_{\perp}^{-2} a} \\
 & + \left(\underbrace{R_0^2 \frac{\tilde{B}^r \partial_{\tilde{r}} \tilde{B}^r}{\tilde{B}^2}}_a + \underbrace{R_0^2 \frac{\tilde{B}^\theta \partial_\theta \tilde{B}^r}{\tilde{B}^2}}_a - \underbrace{R_0^2 \frac{\tilde{B}^r \tilde{B}^r \partial_{\tilde{r}} \tilde{B}^2}{2 \tilde{B}^4}}_{a^2 R_0^{-1}} - \underbrace{R_0^2 \frac{\tilde{B}^\theta \tilde{B}^r \partial_{\tilde{r}} \tilde{B}^2}{2 \tilde{B}^4}}_{a^2 R_0^{-1}} \right) \underbrace{\frac{\partial u}{\partial r}}_{l_{\perp}^{-1}} \\
 & + \left(\underbrace{R_0^2 \frac{\tilde{B}^\theta \partial_\theta \tilde{B}^\theta}{\tilde{B}^2}}_1 + \underbrace{R_0^2 \frac{\tilde{B}^r \partial_r \tilde{B}^\theta}{\tilde{B}^2}}_1 - \underbrace{R_0^2 \frac{\tilde{B}^\theta \tilde{B}^\theta \partial_\theta \tilde{B}^2}{2 \tilde{B}^4}}_{a R_0^{-1}} - \underbrace{R_0^2 \frac{\tilde{B}^r \tilde{B}^\theta \partial_r \tilde{B}^2}{2 \tilde{B}^4}}_{a R_0^{-1}} \right) \underbrace{\frac{\partial u}{\partial \theta}}_{l_{\perp}^{-1} a} \\
 & + \left(\underbrace{R_0^2 \frac{\tilde{B}^r \partial_{\tilde{r}} \tilde{B}^\varphi}{\tilde{B}^2}}_{R_0^{-1} a} + \underbrace{R_0^2 \frac{\tilde{B}^\theta \partial_\theta \tilde{B}^\varphi}{\tilde{B}^2}}_{R_0^{-1} a} - \underbrace{R_0^2 \frac{\tilde{B}^r \tilde{B}^\varphi \partial_{\tilde{r}} \tilde{B}^2}{2 \tilde{B}^4}}_{R_0^{-1} a} - \underbrace{R_0^2 \frac{\tilde{B}^\theta \tilde{B}^\varphi \partial_\theta \tilde{B}^2}{2 \tilde{B}^4}}_{R_0^{-1} a} \right) \underbrace{\frac{\partial u}{\partial \varphi}}_1
 \end{aligned}$$

In the above expression, all terms order 1, $\varepsilon^2 \sigma^{-2}$ or $\varepsilon \sigma^{-1}$ must be kept and only the terms order $\varepsilon^2 \sigma^{-1}$ and ε can be dropped, meaning that of all the 9 derivatives, i.e. $\partial_{\varphi\varphi}^2 u$, $\partial_{\tilde{r}\tilde{r}}^2 u$, $\partial_{\theta\theta}^2 u$, $\partial_{\varphi\theta}^2 u$, $\partial_{\varphi\tilde{r}}^2 u$, $\partial_{\theta\tilde{r}}^2 u$, $\partial_{\tilde{r}\tilde{r}} u$, $\partial_\theta u$, $\partial_\varphi u$, only the first derivative in the toroidal direction $\partial_\varphi u$ can be entirely neglected.

With respect to the parallel operators, the perpendicular ones can be significantly simplified. From Eq. (2.1.22), (2.2.10), (2.2.19) and (2.2.20) we have for the following ordering for the Poisson brackets:

$$\begin{aligned}
 \sigma^2 \rho_*^{-2} [\phi, u] = & \underbrace{\sigma^2 \rho_*^{-2} \underbrace{\frac{\rho_{s0}^2}{\tilde{J}}}_{\rho_{s0}^2 a^{-1} R_0^{-1}} \underbrace{\frac{\tilde{B}_\varphi}{\tilde{B}}}_{R_0} [\phi, u]_{\tilde{r}, \theta}}_1 \\
 & + \underbrace{\sigma^2 \rho_*^{-2} \underbrace{\frac{\rho_{s0}^2}{\tilde{J}}}_{\rho_{s0}^2 a^{-1} R_0^{-1}} \underbrace{\frac{\tilde{B}_r}{\tilde{B}}}_{a R_0^{-1}} [\phi, u]_{\theta, \varphi}}_{\varepsilon \sigma} + \underbrace{\sigma^2 \rho_*^{-2} \underbrace{\frac{\rho_{s0}^2}{\tilde{J}}}_{\rho_{s0}^2 a^{-1} R_0^{-1}} \underbrace{\frac{\tilde{B}_\theta}{\tilde{B}}}_{a^2 R_0^{-1}} [\phi, u]_{\varphi, \tilde{r}}}_{\varepsilon \sigma}
 \end{aligned}$$

Chapter 2. Physical model in toroidal coordinates

Here the leading order is the first term, $\rho_*^2 \sigma^{-2}$, which is already a small term since $\rho_*/\sigma = \rho_{s0}/l_\perp < 1$. The second and third term are $\varepsilon\sigma$ times smaller than the first and will therefore be neglected. As a results, the simplified Poisson brackets involve only derivatives in the poloidal plane.

For the curvature operator, we make use of the ordering for the derivatives of the magnetic field in Eq. (2.2.21), together with Eqs. (2.1.23), (2.2.11), (2.2.19) and (2.2.20). We obtain:

$$\begin{aligned} \sigma \rho_*^{-1} C(u) = & -\sigma \rho_*^{-1} \overbrace{\frac{\rho_{s0} R_0}{2J} \frac{\tilde{B}_\varphi}{\tilde{B}} \frac{\partial_\theta \tilde{B}^2}{\tilde{B}^2} \frac{\partial u}{\partial \tilde{r}}}^1 + \sigma \rho_*^{-1} \overbrace{\frac{\rho_{s0} R_0}{2\tilde{J}} \frac{\tilde{B}_\varphi}{\tilde{B}} \frac{\partial_{\tilde{r}} \tilde{B}^2}{\tilde{B}^2} \frac{\partial u}{\partial \theta}}^1 \\ & + \sigma \rho_*^{-1} \overbrace{\frac{\rho_{s0} R_0}{2\tilde{J}} \left(\frac{\partial_{\tilde{r}} \tilde{B}_\theta}{\tilde{B}} - \frac{\partial_\theta \tilde{B}_r}{\tilde{B}} - \frac{\tilde{B}_\theta}{\tilde{B}} \frac{\partial_{\tilde{r}} \tilde{B}^2}{\tilde{B}^2} + \frac{\tilde{B}_r}{\tilde{B}} \frac{\partial_\theta \tilde{B}^2}{\tilde{B}^2} \right) \frac{\partial u}{\partial \varphi}}^\sigma \end{aligned}$$

The term containing the toroidal derivative is order σ and can be neglected. Also in this case, derivatives act only on the poloidal plane.

In the case of the perpendicular Laplacian, we have to make use of all the ordering for magnetic field components, modulus and derivatives. From its definition in Eq. (2.1.24) and Eq. (2.2.12), we obtain:

$$\begin{aligned} \sigma^2 \rho_*^{-2} \nabla_\perp^2 u = & \sigma^2 \rho_*^{-2} \underbrace{\frac{\rho_{s0}^2}{\tilde{r} \tilde{R}}}_{\rho_{s0}^2 a^{-1} \tilde{R}_0^{-1}} \left[\underbrace{\frac{\partial}{\partial \varphi}}_{a R_0^{-1}} \left(\underbrace{\frac{\tilde{r}}{\tilde{R}}}_{a^2 R_0^{-2}} \left(\underbrace{\frac{\tilde{B}_\theta \tilde{B}^\theta}{\tilde{B}^2}}_1 \frac{\partial u}{\partial \varphi} - \underbrace{\frac{\tilde{B}_\varphi \tilde{B}^\theta}{\tilde{B}^2}}_1 \frac{\partial u}{\partial \theta} \right) \right. \right. \\ & \left. \left. - \underbrace{\frac{\tilde{B}_\varphi \tilde{B}^r}{\tilde{B}^2}}_a \frac{\partial u}{\partial \tilde{r}} + \underbrace{\frac{\tilde{B}_r \tilde{B}^r}{\tilde{B}^2}}_{a^2 R_0^{-2}} \frac{\partial u}{\partial \varphi} \right) \right. \\ & \left. + \frac{\partial}{\partial \theta} \left(\underbrace{\frac{\tilde{R}}{\tilde{r}}}_{a^{-1} R_0} \left(\underbrace{\frac{\tilde{B}_r \tilde{B}^r}{\tilde{B}^2}}_{a^2 R_0^2} \frac{\partial u}{\partial \theta} - \underbrace{\frac{\tilde{B}_\theta \tilde{B}^r}{\tilde{B}^2}}_{a^3 R_0^{-2}} \frac{\partial u}{\partial \tilde{r}} - \underbrace{\frac{\tilde{B}_\theta \tilde{B}^\varphi}{\tilde{B}^2}}_{a^2 R_0^{-2}} \frac{\partial u}{\partial \varphi} \right) \right. \right. \\ & \left. \left. + \underbrace{\frac{\tilde{B}_\varphi \tilde{B}^\varphi}{\tilde{B}^2}}_1 \frac{\partial u}{\partial \theta} \right) \right. \\ & \left. + \frac{\partial}{\partial r} \left(\underbrace{\frac{\tilde{r} \tilde{R}}{a R_0}}_{a R_0} \left(\underbrace{\frac{\tilde{B}_\varphi \tilde{B}^\varphi}{\tilde{B}^2}}_1 \frac{\partial u}{\partial \tilde{r}} - \underbrace{\frac{\tilde{B}_r \tilde{B}^\varphi}{\tilde{B}^2}}_{a R_0^{-2}} \frac{\partial u}{\partial \varphi} - \underbrace{\frac{\tilde{B}_r \tilde{B}^\theta}{\tilde{B}^2}}_{a R_0^{-2}} \frac{\partial u}{\partial \theta} + \underbrace{\frac{\tilde{B}_\theta \tilde{B}^\theta}{\tilde{B}^2}}_{a^2 R_0^{-2}} \frac{\partial u}{\partial \tilde{r}} \right) \right) \right] \end{aligned}$$

where the terms in the boxes are the terms that dominate after taking the partial derivative in each line. Finally we have

$$\sigma^2 \rho_*^{-2} \nabla_\perp^2 u \sim -\sigma^2 \rho_*^{-2} \overbrace{\frac{\rho_{s0}^2}{\tilde{R}^2} \frac{\tilde{B}_\varphi \tilde{B}^r}{\tilde{B}^2} \frac{\partial^2 u}{\partial \tilde{r} \partial \varphi}}^{\varepsilon \sigma} + \sigma^2 \rho_*^{-2} \overbrace{\frac{\rho_{s0}^2}{\tilde{r}^2} \frac{\tilde{B}_\varphi \tilde{B}^\varphi}{\tilde{B}^2} \frac{\partial^2 u}{\partial \theta^2}}^1 + \sigma^2 \rho_*^{-2} \rho_{s0}^2 \overbrace{\frac{\tilde{B}_\varphi \tilde{B}^\varphi}{\tilde{B}^2} \frac{\partial^2 u}{\partial \tilde{r}^2}}^1$$

Therefore of all the initial terms only two will be retained, one containing a double derivative

2.2. Differential operators in toroidal coordinates

in \tilde{r} and the other a double derivative in θ , once again the originally 3D operators is reduced to 2D. Note that this time the effect on code implementation is important, since ∇_{\perp}^2 has to be inverted to give the electric potential from the vorticity (the last equation of the drift-reduced Braginskii's equation (2.1.17)), inverting a 2D operator or instead of a full 3D one leads to drastic reduction in computational cost.

To conclude, by neglecting terms that are order ρ_* , σ , ε or smaller and introducing the explicit form of the magnetic field components in terms of the poloidal flux (Eq. (2.2.7) and Eq. (2.2.6)) we obtain the simplified expression for the differential operators:

$$\nabla_{\parallel} u = \frac{B_0}{|B_0|} \frac{\partial u}{\partial \varphi} + \frac{a}{\rho_{s0}} \partial_{\hat{r}} \psi \frac{1}{r} \frac{\partial u}{\partial \theta} - \frac{a}{\rho_{s0}} \frac{1}{\hat{r}} \partial_{\theta} \psi \frac{\partial u}{\partial r} \quad (2.2.26)$$

$$\begin{aligned} \nabla_{\parallel}^2 u &= \frac{\partial^2 u}{\partial \varphi^2} + d_{rr} \frac{\partial^2 u}{\partial r^2} + d_{\theta\theta} \frac{1}{r^2} \frac{\partial^2 u}{\partial \theta^2} \\ &+ d_{\varphi\theta} \frac{1}{r} \frac{\partial^2 u}{\partial \varphi \partial \theta} - d_{\varphi r} \frac{\partial^2 u}{\partial \varphi \partial r} - d_{\theta r} \frac{1}{r} \frac{\partial^2 u}{\partial \theta \partial r} \\ &+ d_r \frac{\partial u}{\partial r} + d_{\theta} \frac{1}{r} \frac{\partial u}{\partial \theta} \end{aligned} \quad (2.2.27)$$

$$[\phi, u] = \frac{1}{r} \frac{B_0}{|B_0|} [\phi, u]_{r,\theta} \quad (2.2.28)$$

$$C(u) = \frac{B_0}{|B_0|} \left(\sin \theta \frac{\partial u}{\partial r} + \frac{\cos \theta}{r} \frac{\partial u}{\partial \theta} \right) \quad (2.2.29)$$

$$\nabla_{\perp}^2 u = \frac{\partial^2 u}{\partial r^2} + \frac{1}{r^2} \frac{\partial^2 u}{\partial \theta^2} \quad (2.2.30)$$

Note that we have introduced two different dimensionless form of the radial coordinate, $\hat{r} = \tilde{r}/a$, $r = \tilde{r}/\rho_{s0}$, to highlight the two different scale lengths of equilibrium poloidal flux and fluctuating quantities. The coefficients appearing in the parallel Laplacian are:

$$\begin{aligned} d_{rr} &= \frac{a^2}{\rho_{s0}^2 \hat{r}^2} (\partial_{\theta} \psi)^2, & d_{\theta\theta} &= \frac{a^2}{\rho_{s0}^2} (\partial_{\hat{r}} \psi)^2, \\ d_{\varphi\theta} &= \frac{2a}{\rho_{s0}} \frac{B_0}{|B_0|} \partial_{\hat{r}} \psi, & d_{\varphi r} &= \frac{2a}{\rho_{s0}} \frac{B_0}{|B_0|} \frac{1}{\hat{r}} \partial_{\theta} \psi, & d_{\theta r} &= \frac{2a^2}{\rho_{s0}^2 \hat{r}} \partial_{\hat{r}} \psi \partial_{\theta} \psi \\ d_r &= \frac{a}{\rho_{s0} \hat{r}^2} \left(\partial_{\theta} \psi \partial_{\hat{r}\theta}^2 \psi - \partial_{\hat{r}} \psi \partial_{\theta\theta}^2 \psi - \frac{1}{\hat{r}} (\partial_{\theta} \psi)^2 \right) \\ d_{\theta} &= \frac{a}{\rho_{s0} \hat{r}} \left(\partial_{\hat{r}} \psi \partial_{\hat{r}\theta}^2 \psi - \partial_{\theta} \psi \partial_{\hat{r}\hat{r}}^2 \psi + \frac{1}{\hat{r}} \partial_{\hat{r}} \psi \partial_{\theta} \psi \right) \end{aligned}$$

These simplified operators expressions in Eqs. (2.2.26)-(2.2.30) have been checked using Mathematica, starting from the operators definition Eqs. (2.1.20)-(2.1.24) and the magnetic field expressions (2.2.7), (2.2.6) and imposing the scaling assumptions on ψ and u derivatives in Eqs. (2.2.15)-(2.2.23).

Interestingly, the perpendicular operators (i.e. $[\phi, u]$, $C(u)$, and $\nabla_{\perp}^2 u$) do not depend on the

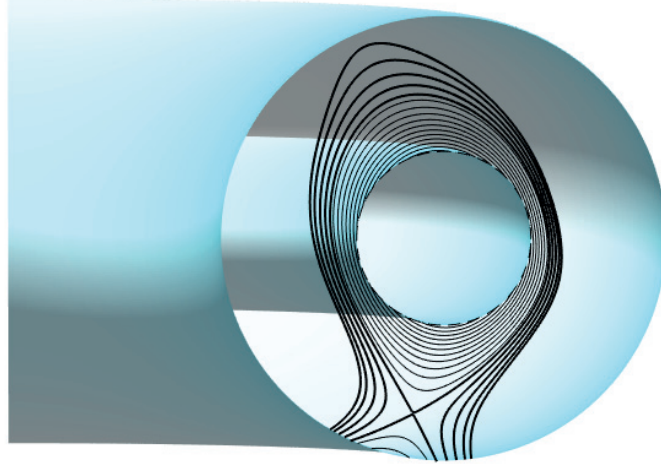


Figure 2.1 – Sketch of the computational domain of GBS with a contour plot of the poloidal flux ψ in the edge (thin lines) and in the SOL (thick lines).

poloidal flux ψ , the information on the magnetic field topology is solely carried by the parallel operators $\nabla_{\parallel} u$ and $\nabla_{\parallel}^2 u$. Furthermore the our approximation led to simplification of the perpendicular operators that are now acting only in the poloidal plane, but did not impact significantly the parallel ones, that are still (unfortunately) fully 3D.

Finally, we would like to stress the flexibility resulting from the use of toroidal coordinates. All expressions of the geometrical operators are reduced to combinations of derivatives in r, θ , and φ multiplied by coefficients that depend only on the equilibrium magnetic field. The resulting scheme is very flexible, since by prescribing these values as input parameters, any axisymmetric magnetic equilibrium can be investigated, for example single null, double null or snowflake configurations.

2.3 Radial boundary conditions

The domain where Eqs. (2.1.11)-(2.1.17) are solved is a toroidal ring, $r_{\min} \leq r \leq r_{\max}$, $0 \leq \theta < 2\pi$, $0 \leq \varphi < 2\pi$. The ring is centered at the tokamak magnetic axis and contains a closed flux surface region, the separatrix, the X-point, and divertor legs (see Fig. 2.1).

In the previous limited configuration implemented in GBS, the magnetic field lines were intersecting the wall at the toroidal limiter, usually localised at the low field side, coinciding with $\theta = 0$ (or $\theta = 2\pi$) (see Fig. 1.2). In diverted configuration there is no limiter, and the magnetic field lines enter the wall at $r = r_{\max}$, not only at the divertor plates, but all along the outer wall.

The plasma interaction with a solid wall is described by the boundary conditions at the magnetic pre-sheath entrance, developed by Loizu *et al.* [31] in the cold ion limit and then

extended by Masetto *et al.* [27] to include hot ion effects. These were previously applied as boundary conditions in θ , at the limiter location, and are now adapted to be applied at the outer wall, in the radial direction:

$$\begin{aligned}
 v_{\parallel,i} &= \pm \sqrt{T_e} F_T \\
 v_{\parallel,e} &= \pm \sqrt{T_e} \max\{\exp(\lambda - \frac{\phi}{T_e}), \exp(\lambda)\} \\
 \partial_r \phi &= \mp \frac{\sqrt{T_e}}{F_T} \partial_r v_{\parallel,i} \\
 \partial_r n &= \mp \frac{n}{\sqrt{T_e} F_T} \partial_r v_{\parallel,i} \\
 \omega &= -\frac{1}{F_T^2} (\partial_r v_{\parallel,i})^2 \mp \frac{\sqrt{T_e}}{F_T} \partial_{rr}^2 v_{\parallel,i} \\
 \partial_r T_e &= 0 \\
 \partial_r T_i &= 0
 \end{aligned} \tag{2.3.1}$$

with $F_T = \sqrt{1 + \tau T_i / T_e}$. Where all quantities are in GBS dimensionless units. The plus/minus indicates whether the magnetic field points towards (top sign) or out from the wall (bottom sign). Note that, for simplicity, the boundary conditions in Eqs. (2.3.1) neglect correction terms containing derivatives along the wall, included in Ref. [31].

Boundary conditions are also required towards the core at $r = r_{\min}$. Since we lack a physical model to describe the interaction between edge and core, an *ad hoc* set of boundary conditions is chosen. We impose for all fields $\partial_r u = 0$ (homogeneous Neumann), except for ω and ϕ , for which we impose Dirichlet conditions $\omega = 0$ and $\phi = \lambda T_e$. The electric potential ϕ requires a Dirichlet condition to grant uniqueness of the solution for the Poisson's equation $\nabla_{\perp}^2 \phi = \omega + \tau T_i$ (Eq. (2.1.17)). The presence of the sources of plasma density and temperature in the closed flux surface region should help decouple the plasma dynamics in the edge and SOL from the *ad hoc* core boundary conditions, which are not based on a physical rationale. In the poloidal and toroidal directions the domain is periodic.

We remark that most magnetic equilibria used in experiments present a vertically elongated shape. As a consequence, the use of a circular ring as a computational domain results into an inefficient use of resources. In these cases the use of toroidal coordinates with a vertical elongation, such that constant r surfaces map ellipses instead of circles, is a relatively straightforward possible future implementation to exploit more efficiently the computational domain.

2.4 Initial conditions

The long term evolution of the system is statistically independent of the initial conditions. For this reason the initial conditions are not physically interesting, and they are just chosen compatible with the boundary conditions. We impose $\phi(r, \theta, \varphi) = \lambda T_e$, with T_e being an initial

Chapter 2. Physical model in toroidal coordinates

constant electron temperature. Similarly, ω , n and T_i are usually set to a constant value on the entire domain. Additionally, we impose $v_{\parallel e} = v_{\parallel i}$, with the $v_{\parallel e}, v_{\parallel i}$ functions satisfying $v_{\parallel e, i}|_{r_{\max}} = \pm\sqrt{T_e}$ and $\partial_r v_{\parallel e, i}|_{r_{\max}} = 0$, such that the right-hand side of the boundary conditions for n, ϕ, ω is zero at the wall (see Eqs. (2.3.1)), according to uniform initial profiles of these quantities. Finally, for all fields, the initial conditions present no toroidal dependence, except for a three-dimensional random noise that is added to seed plasma turbulence.

3 Numerical implementation and code verification

Hereafter we detail the implementation in the GBS code of the physical model described in chapter 2. Our implementation is based on the GBS version for the simulation of limited plasma, which uses flux aligned coordinates [23]. With respect to the limited version of GBS, the use of toroidal coordinates impacts the operators expressions (see Eqs. (2.2.26)-(2.2.30)), and the use of a diverted equilibrium, instead of a limited one, impacts the boundary conditions (Sec. 2.3) and the initial conditions (Sec. 2.4). To compensate for the lack of alignment between grid and magnetic field, we increase the order of accuracy of the centered finite differences scheme.

This chapter is structured as follow. First the code structure is presented in Sec. 3.1. The spatial discretisation including the grid used and the new finite difference scheme that implements the spatial operators is the subject of Sec. 3.2. We then focus on the boundary conditions used in the case of a diverted equilibrium (Sec. 3.3). Finally, we test the code implementation and performance in sections 3.4, 3.5, 3.6, and 3.7.

3.1 Code structure

Figure 3.1 sketches the GBS code work-flow. We first set the initial condition (IC) for $\mathbf{u} = n, T_{e,i}, v_{\parallel e,i}, \omega$ and electric potential ϕ , such that it satisfies the Poisson's Eq. (2.1.17) and the boundary conditions in (2.3.1). The time loop includes the evaluation of the right hand side (RHS) of the drift-reduced Braginskii's equations (2.1.11)-(2.1.16). This is computed and stored in the vector \mathbf{k}_i with $i = 1, \dots, 4$ corresponding to the four substeps of the fourth order Runge-Kutta (RK4) time stepping. The fields values at each substep are computed combining their expression at the previous time step, \mathbf{u}^n , with \mathbf{k}_i according to the Runge-Kutta scheme. In figure 3.1, \mathbf{u}^n is assigned to $[n^{[1]}, T_{e,i}^{[1]}, \dots]$, where the square brackets around the apex indicate a Runge-Kutta substep, in this case $[j] = [1]$ is the last substep, as $i = 1, \dots, 4$ but $j = \text{mod}(i, 4) + 1 = 2, 3, 4, 1$. At every substep the boundary conditions (BC) are applied and the Poisson's equation for the electric potential is solved. This requires the inversion of the perpendicular Laplacian and is the computational bottleneck of the code.

The boxes contoured with a dashed line were modified in the framework of the present thesis

```

Set IC for  $\mathbf{u}^{[1]} = [n^{[1]}, T_{e,i}^{[1]}, v_{\parallel e,i}^{[1]}, \omega^{[1]}, \phi^{[1]}]$ 
for n = 1:Tmax/dt
     $\mathbf{u}^n = [n^{[1]}, T_{e,i}^{[1]}, v_{\parallel e,i}^{[1]}, \omega^{[1]}, \phi^n = \phi^{[1]}$ 
    for i = 1:4
         $\mathbf{k}_i = \text{RHS}(\mathbf{u}^{[i]}, \phi^{[i]})$ 
        j = mod(i,4)+1
        if j = 1     $\mathbf{u}^{[j]} = \mathbf{u}^n + dt/6(\mathbf{k}_1 + 2\mathbf{k}_2 + 2\mathbf{k}_3 + \mathbf{k}_4)$ 
        if j = 2,3   $\mathbf{u}^{[j]} = \mathbf{u}^n + dt/2 \mathbf{k}_{j-1}$ 
        if j = 4     $\mathbf{u}^{[j]} = \mathbf{u}^n + dt \mathbf{k}_{j-1}$ 
        Apply BC to  $\mathbf{u}^{[j]}$ 
         $\nabla_{\perp}^2 \phi^{[j]} = \omega^{[j]} - \tau \nabla_{\perp}^2 T_i^{[j]}, + \text{BC for } \phi^{[j]}$ 
    end
end
end

```

Figure 3.1 – Work-flow of GBS, for both the flux aligned limited version and the toroidal diverted one. The boxes contoured with dashed line correspond to the blocks of code rewritten in the framework of this thesis.

to use toroidal coordinates, diverted equilibrium, and the new finite differences scheme. Note that the new differential operators are discretised and applied to the fields when evaluating the right-hand side of the drift-reduced Braginskii's equations and when inverting the Laplacian.

The drift-reduced Braginskii's equations are evolved until a quasi-steady state is reached, where the plasma quantities averaged on the 3D domain fluctuate in time around a constant value. This state results from a balance between the fluxes of plasma density and temperature coming from the core, turbulent transport across the magnetic flux surfaces, and the plasma losses to the wall.

3.2 Spatial discretisation

3.2.1 Numerical grid and staggering

We discretise our domain by using a numerical grid of N_r , N_θ , and N_φ points along the radial, poloidal and toroidal directions respectively. The discretisation in the toroidal direction is usually coarser than in the poloidal or radial directions ($2\pi/N_\varphi > 2\pi/N_\theta \sim (r_{\max} - r_{\min})/N_r$) reflecting the difference in characteristic scale lengths discussed in Sec. 2.2.6. For simplicity, the spacing is chosen to be constant in each direction, even though in the future a possibility could be to use a more refined mesh for the SOL and wall boundaries to reduce the computational cost of the simulation.

Figure 3.2 shows the difference between the flux aligned grid used for GBS in limited simulations [17] (left) and the toroidal one for diverted simulations (right). The black dashed lines trace the grid and help visualising its alignment (left) and misalignment (right) with

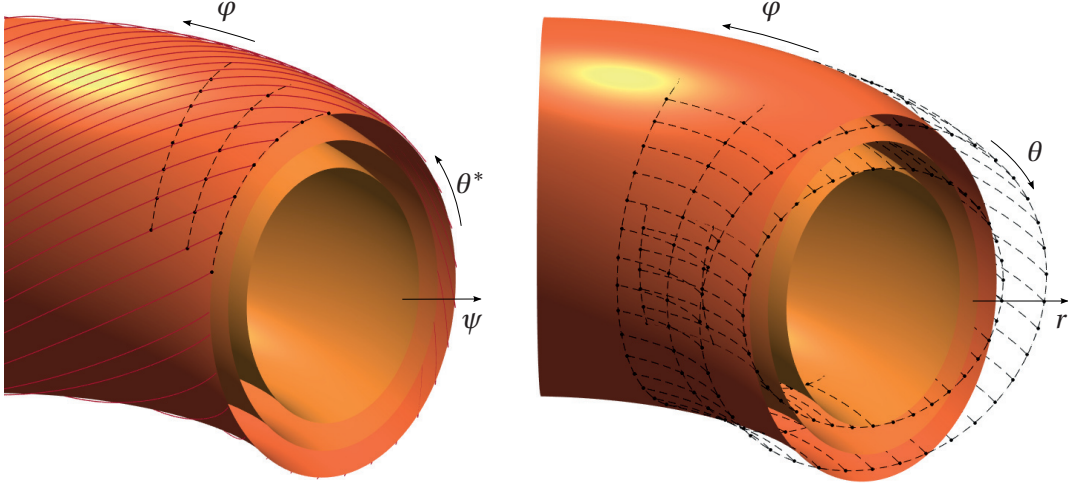


Figure 3.2 – Schematic comparison between grids of the two version of GBS: the flux aligned for limited simulation (left) and the one discretising the toroidal coordinates, for diverted configuration (right). The case of a limited elongated equilibrium is shown. The numerical grid points in black help visualising the alignment/misalignment of the coordinate system with respect to the magnetic field line (traced by red continuous lines) and the flux surfaces.

respect to the flux surface. Note that we could not compare the two schemes on a diverted configuration as the existing version of GBS in flux aligned coordinates for the limited cases (obviously) does not allow for it. For a schematic visualisation of toroidal grid applied to a diverted equilibrium see Fig. 1.4. We choose to consider an elongated equilibrium rather than a circular one because in a circular equilibrium the two coordinate systems coincide, partly motivating our choice to use toroidal coordinates rather than Cartesian ones. The numerical grid in the flux aligned case is always chosen such that the grid points are aligned on the magnetic field line (traced with solid red lines), to facilitate the treatment and the accuracy of the parallel operators.

We stagger the grid that discretises the n , ϕ , ω , T_e and T_i fields (n -grid) with respect to the grid where we evaluate $v_{\parallel e}$ and $v_{\parallel i}$ (v -grid) in the toroidal and poloidal directions. In the limited version of GBS, this was only done in the toroidal direction. Staggered-grids were first used by Harlow and Welch in 1965 [32] to provide a remedy to the checkerboard patterns that can appear when treating an advection problem with centered finite differences, as shown in [33]. The idea behind grid staggering can be shown by considering a minimal system, contained in the drift-reduced Braginskii's equations (2.1.11) and (2.1.12), which describes the evolution of density and electron parallel velocity, i.e.:

$$\begin{aligned}\partial_t N + \nabla_{\parallel} v_{\parallel e} &= 0 \\ \partial_t v_{\parallel e} + T_e \nabla_{\parallel} N &= 0\end{aligned}$$

where we indicate $N = \log(n)$ and we consider T_e constant for simplicity. If a second order

centered finite difference scheme is used to discretise the parallel derivative of N and $v_{\parallel e}$ on the same uniform grid of spacing Δx , together with an explicit Euler time discretisation of step Δt , we obtain:

$$N_j^{m+1} = N_j^m - \frac{\Delta t}{2\Delta x} \left(v_{\parallel e, j+1}^m - v_{\parallel e, j-1}^m \right) \quad (3.2.1)$$

$$v_{\parallel e, j}^m = v_{\parallel e, j}^{m-1} - \frac{\Delta t}{2\Delta x} T_e \left(N_{j+1}^{m-1} - N_{j-1}^{m-1} \right) \quad (3.2.2)$$

Here j and m indicate the spatial and temporal grid index, i.e. $N_j^m = N(x_j, t_m)$. Combining equations (3.2.1) and (3.2.2) we derive:

$$\frac{1}{\Delta t^2} \left(N_j^{m+1} - 2N_j^m + N_j^{m-1} \right) = \frac{1}{4\Delta x^2} T_e \left(N_{j-2}^{m-1} - 2N_j^{m-1} + N_{j+2}^{m-1} \right) \quad (3.2.3)$$

We note that in Eq. (3.2.3) N_j^{m+1} only depends on values of N at the $j-2$, j and $j+2$ points. The values of N on even and odd grid points are therefore decoupled. This decoupling allows for nonphysical checkerboarder patterns, i.e. solutions with a, b such that $N_j = a$ for even j , and $N_j = b$ for odd j , with $a \neq b$. Shifting the position of the grid point at which v is evaluated by $\Delta x/2$, midway between two n -grid points, i.e. “staggering” the n and v -grids, avoids the formation of checkerboarder patterns. Grid staggering could be extended to the radial direction in the future.

3.2.2 Fourth order finite differences

In order to compensate for the misalignment between numerical grid and magnetic field, we proceed with the implementation of fourth order finite difference operators in GBS, an upgrade with respect to the second order scheme used in the flux aligned/limited version. Hereafter we describe the discretisation of derivatives in one-dimension, since all GBS operators, except for the Poisson brackets, can be computed as a linear combination of derivatives in r, θ , and ϕ . More precisely, the differential operators can be written in terms of the discretised first derivatives $D_x, D_x^{n2v}, D_x^{v2n}$, the discretised second derivative D_{xx} , and of the interpolation between staggered grids, I_x^{n2v}, I_x^{v2n} , which are defined as:

$$D_x u_j = \frac{1}{\Delta x} \left[\frac{1}{12} u_{j-2} - \frac{2}{3} u_{j-1} + \frac{2}{3} u_{j+1} - \frac{1}{12} u_{j+2} \right] \quad (3.2.4)$$

$$D_x^{n2v} u_j = \frac{1}{\Delta x} \left[\frac{1}{24} u_{j-2} - \frac{9}{8} u_{j-1} + \frac{9}{8} u_j - \frac{1}{24} u_{j+1} \right] \quad (3.2.5)$$

$$D_x^{v2n} u_j = \frac{1}{\Delta x} \left[\frac{1}{24} u_{j-1} - \frac{9}{8} u_j + \frac{9}{8} u_{j+1} - \frac{1}{24} u_{j+2} \right] \quad (3.2.6)$$

$$D_{xx} u_j = \frac{1}{\Delta x^2} \left[-\frac{1}{12} u_{j-2} + \frac{4}{3} u_{j-1} - \frac{5}{2} u_j + \frac{4}{3} u_{j+1} - \frac{1}{12} u_{j+2} \right] \quad (3.2.7)$$

$$I_x^{n2v} u_j = \left[-\frac{1}{16} u_{j-2} - \frac{9}{16} u_{j-1} + \frac{9}{16} u_j - \frac{1}{16} u_{j+1} \right] \quad (3.2.8)$$

$$I_x^{v2n} u_j = \left[-\frac{1}{16} u_{j-1} - \frac{9}{16} u_j + \frac{9}{16} u_{j+1} - \frac{1}{16} u_{j+2} \right] \quad (3.2.9)$$

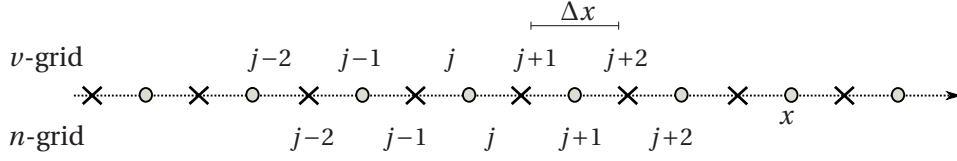


Figure 3.3 – Sketch of the grid staggering performed in the θ and φ . Here x is either one of these directions. The velocities $v_{\parallel e}$ and $v_{\parallel i}$ are evaluated on v -grid points, indicated with crosses, while n, ω, ϕ, T_e and T_i are evaluated on n -grid points, indicated with circles. The labeling of the grid points is useful to interpret the expressions of the discretised derivatives and discrete interpolation in Eq. (3.2.4)-(3.2.9), that allow operating between the two grids.

where x stands for one of the three coordinates r, θ , or φ , and the apex $n2v$ ($v2n$) indicates that the input field is defined on the n -grid (v -grid) and the output on the v -grid (n -grid) (see Fig. 3.3). For example, the advection term in the density equation (2.1.11), evaluated on a n -grid point $(r_j, \theta_k, \varphi_l)$, is computed as:

$$\begin{aligned} (n\nabla_{\parallel} v_{\parallel e})_{j,k,l} &= n \left(c_1 \frac{\partial v_{\parallel e}}{\partial \varphi} + c_2 \frac{\partial v_{\parallel e}}{\partial \theta} + c_3 \frac{\partial v_{\parallel e}}{\partial r} \right) \\ &\simeq n_{i,j,k} \left(c_1 I_{\theta}^{v2n} D_{\varphi}^{v2n} v_{\parallel e} + c_2 I_{\varphi}^{v2n} D_{\theta}^{v2n} v_{\parallel e} + c_3 I_{\theta}^{v2n} I_{\varphi}^{v2n} D_r v_{\parallel e} \right)_{j,k,l} \end{aligned}$$

where $c_1 = B_0/|B_0|$, $c_2 = \partial_r \psi a / \rho_{s0}$, $c_3 = -\partial_{\theta} \psi a / \rho_{s0}$, from Eq. (2.2.26). Note that the interpolation is performed only along the θ and φ directions, since there is no staggering in r . We also note that all the above operators require a 5-point stencil $[j-2, j+2]$ and that $n2v$ and $v2n$ operators use the same coefficients.

Two additional operators, D_{xx}^{n2v} and D_{xx}^{v2n} , are needed for the curvature-related contribution to the gyro-viscous terms, in Eqs. (2.1.18)-(2.1.19), i.e. $C(\nabla_{\parallel}(u))$, $\nabla_{\parallel}(C(u))$ and $C(C(u))$. Since a fourth order implementation of these operators requires a 7-points stencil, which impacts the number of ghost points in the treatment of the MPI subdomain boundaries (see Sec. 3.4), D_{xx}^{n2v} and D_{xx}^{v2n} are implemented at second order:

$$D_{xx}^{n2v} u_j = \frac{1}{\Delta x^2} \left[\frac{1}{2} u_{j-2} - \frac{1}{2} u_{j-1} - \frac{1}{2} u_j + \frac{1}{2} u_{j+1} \right] \quad (3.2.10)$$

$$D_{xx}^{v2n} u_j = \frac{1}{\Delta x^2} \left[\frac{1}{2} u_{j-1} - \frac{1}{2} u_j - \frac{1}{2} u_{j+1} + \frac{1}{2} u_{j+2} \right] \quad (3.2.11)$$

In the limited version of GBS, the Poisson brackets are discretised by using the Arakawa scheme at second order [34]. We keep the use of Arakawa scheme in the diverted version but we implement it at fourth order [35], to be consistent with the rest of the code.

Finally, to compute the electric potential according to Eq. (2.1.17), one needs to invert the perpendicular diffusion operator $\nabla_{\perp}^2 = \partial_{rr}^2 + 1/r^2 \partial_{\theta\theta}^2$, see Eq. (2.2.30). This is done by using a LU factorisation of the matrix resulting from the fourth order discretisation of this operator, computed once for all at the beginning of the simulation.

3.3 Implementation of the boundary conditions

Two ghosts points are added on each side of the radial domain, i.e. $r = r_{\min}$ and $r = r_{\max}$, to impose Dirichlet and Neumann boundary conditions. By indicating the grid points inside the domain with indices $i = 1, \dots, N_r$, the four ghosts points have indices $i = -1, 0$ at the boundary $r = r_{\min}$ and $i = N_r + 1, N_r + 2$ at the vessel wall. We impose that the boundary conditions are satisfied midway between the $i = 0$ and $i = 1$ points and between the $i = N_r$ and $i = N_r + 1$ points, for core and wall boundaries respectively. In practice, to implement the Dirichlet boundary condition $u(r_{\min}) = u_b$ for ω and ϕ , we impose $(u_0 + u_1)/2 = u_b$ and, at the same time, $(u_{-1} + u_2)/2 = u_b$. The same scheme is applied to ω to impose the Dirichlet boundary conditions at the wall $r = r_{\max}$. On the other hand, to impose the Dirichlet conditions at $r = r_{\max}$ for $v_{\parallel e}$ and $v_{\parallel i}$ we impose $u_{N_r+2} = u_{N_r+1} = u_b$. To implement Neumann boundary condition $\partial_r n|_{r_{\min}} = u_b$ (and similarly for $T_e, T_i, v_{\parallel e}, v_{\parallel i}$), we set $(u_1 - u_0)/\Delta r = u_b$ and $(u_0 - u_{-1})/\Delta r = u_b$. The same holds at $r = r_{\max}$ for n, T_e, T_i , and ϕ . These schemes are preferred to a fourth-order algorithm for numerical stability.

A discontinuity arises in the velocities boundary condition at the locations where the magnetic field is tangent to the wall, see Eq. (2.3.1). At these locations, the boundary condition for parallel ion velocity presents a jump from $-\sqrt{T_e}$ to $+\sqrt{T_e}$, and a similar discontinuity arises for $v_{\parallel e}$. This issue is solved by applying a smoothing function from $+\sqrt{T_e}$ to $-\sqrt{T_e}$ so the $v_{\parallel i}$ boundary condition varies continuously at the wall. The discontinuity present in the $v_{\parallel e}$ boundary condition is treated similarly. The discontinuity in n and ϕ boundary is only apparent, as the term $\mp \partial_r v_{\parallel i}$ remains generally negative across the points where \mathbf{B} is tangent to the wall. We remark that this *ad hoc* smoothing function is required since a rigorous derivation of the magnetic pre-sheath boundary conditions for \mathbf{B} tangent to the wall has not been developed yet, despite recent significant work on the subject [36]-[37].

3.4 Parallelisation

The use of the fourth order Runge-Kutta explicit time stepping method allows GBS to be easily parallelised. Domain decomposition is performed in all three coordinates (r, θ, φ) and ghost cell passing is carried out by using standard MPI calls. We note that the use of 5-points stencils for the numerical operators (see section 3.2) requires two ghosts points to be passed in each direction.

For the computation of the electric potential ϕ , Eq. (2.1.17), a direct solver based on the MUMPS library [38]-[39] is used. An iterative multigrid method is also implemented in GBS to allow for a massive parallelisation of the solution of the Laplace operator in the poloidal plane [23], but it is only available for the second order finite difference scheme in the limited scenario at the moment (an ongoing effort is targeted to port the multigrid solver to fourth order).

Scalability tests of the new version of the GBS code are performed using the CPU partition of the Piz Daint supercomputer (hybrid Cray XC40) at the Swiss National Supercomputing Center in Lugano, Switzerland. Figure 3.4 shows the results of a strong scaling test (left), where

3.5. Comparison with previous version of GBS in limited configuration

the grid size is kept constant while the number of cores is increased, and of a weak scaling test (right), where the grid size and the number of cores in φ are increased simultaneously keeping their ratio constant. For both scalings the inverse normalised elapsed times, t_{Ncores}/t_{N_0} , i.e. the *speedup* for the strong scaling and the *efficiency* for the weak scaling, are plotted as a function of the number of cores ($Ncores$). Good scaling properties are observed up to 4608 cores for a grid of $N_r \times N_\theta \times N_\varphi = 512 \times 1024 \times 256$, which corresponds to that of a simulation of a medium size tokamak.

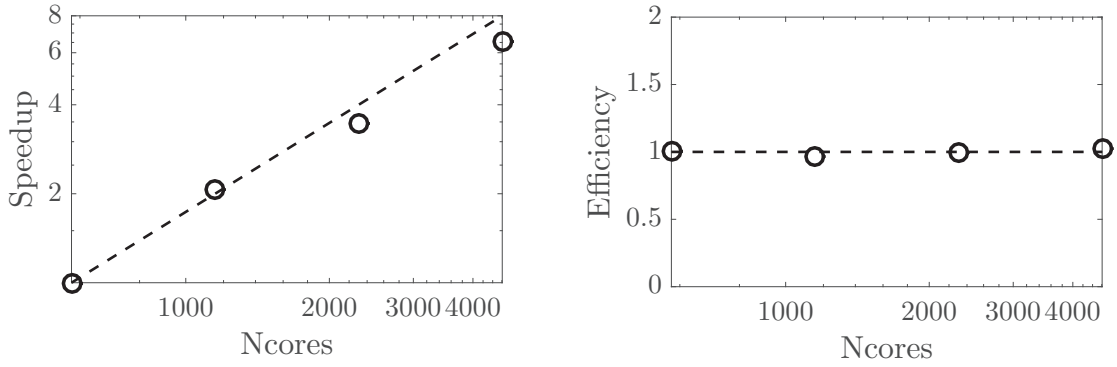


Figure 3.4 – Results of strong (left) and weak (right) scaling tests on Piz Daint. In the strong scaling the grid size is fixed to $N_r \times N_\theta \times N_\varphi = 512 \times 1024 \times 256$ and the number of cores is increased. The speedup, i.e. the inverse of the normalised elapsed time, is expected to scale linearly with the number of cores in the ideal case. In the weak scaling, the ratio of grid size to number of cores stays constant as the number of cores increases ($N_r \times N_\theta \times N_\varphi = 512 \times 1024 \times N_\varphi$). In this case the efficiency, i.e. the normalised elapsed time, is expected to be constant.

3.5 Comparison with previous version of GBS in limited configuration

As a first step to check the performance of the new version of the GBS code in toroidal coordinates, we simulate a limited circular configuration and compare the results with the previous version of GBS in flux aligned coordinates. We refer to the new and old version of GBS as tor4 and fa2, respectively. For the comparison we consider a flux function of the form:

$$\psi(\hat{r}, \theta) = -\frac{\hat{r}^2}{2q}, \quad q = 4 \quad (3.5.1)$$

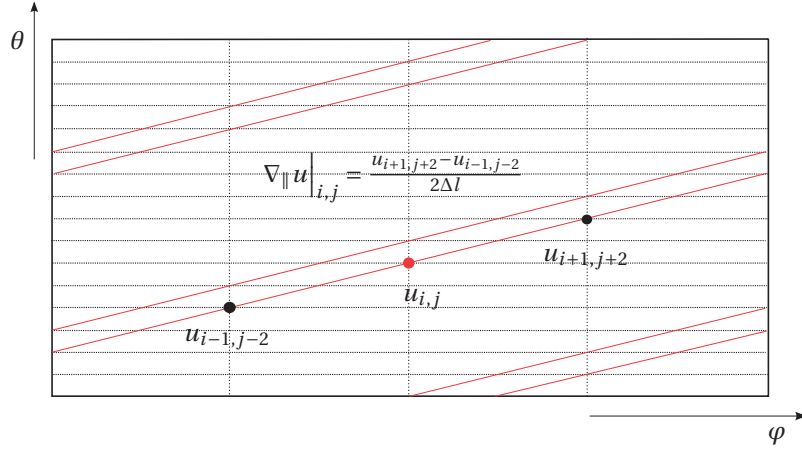


Figure 3.5 – Sketch of fa2 grid on a flux surface and parallel gradient scheme. The dotted intersection of the dotted lines represent the grid points, the red continuous lines trace two neighbouring magnetic field lines looping around the flux surface. Note how the parallel operator expression “skips” one point in θ , allowing for a toroidal grid coarser by a factor of two. In fact, given here $q = 2$, $\hat{r} = 1$ and $N_{\theta} = 16$, we can use $N_{\varphi} = 4$ instead of $N_{\varphi} = N_{\theta} / (\hat{r} q) = 8$.

In limited circular configuration, flux aligned coordinates and toroidal coordinates (r, θ, φ) coincide, since the radial component of the magnetic field is zero ($\mathbf{B}_r \propto \partial_{\theta} \psi = 0$ from Eq. (2.2.7) and (3.5.1)). Hence, the main difference between the two codes is the treatment of the parallel operators acting in the poloidal and toroidal direction. While the tor4 version computes the parallel derivative through its projection along the φ and θ directions, the fa2 version aligns the grid points to the magnetic field line to compute the parallel operators directly in the parallel direction.

In the tor4 version, the parallel operator is expressed as $\nabla_{\parallel} u = \partial_{\varphi} u - \partial_{\theta} u / (\hat{r} q)$ (from Eqs. (3.5.1) and (2.2.26)), and is discretised using a 5×5 point stencil in θ, φ corresponding to fourth order finite differences, on staggered grids.

In the fa2 version, the alignment of the structured flux aligned grid (r, θ, φ) (with θ geometrical poloidal angle) to the magnetic field lines is possible if q is rational and constant across flux surfaces, by choosing $N_{\varphi} / N_{\theta} = 1 / (\hat{r} q)$ with $\hat{r} = 1$ corresponding to $\tilde{r} = a$. The second order finite difference scheme used to compute the parallel derivative in fa2 is sketched in Fig. 3.5 on a flux surface for a magnetic field line of $q = 2$. Note that in the fa2 code it is possible to allow for a toroidal grid coarser by a factor 2, by taking only one every two points in θ when computing the parallel gradient¹, as shown in Fig. 3.5. This reduces the computational cost and reflects the difference in gradient length scales in the parallel and perpendicular directions.

¹It is possible to extend this algorithm to a factor n higher than 2, in order to have $N_{\varphi} \rightarrow N_{\varphi} / n$, but it can lead to numerical instability at the boundaries as it requires the extrapolation of n boundary points at the limiter.

3.5. Comparison with previous version of GBS in limited configuration

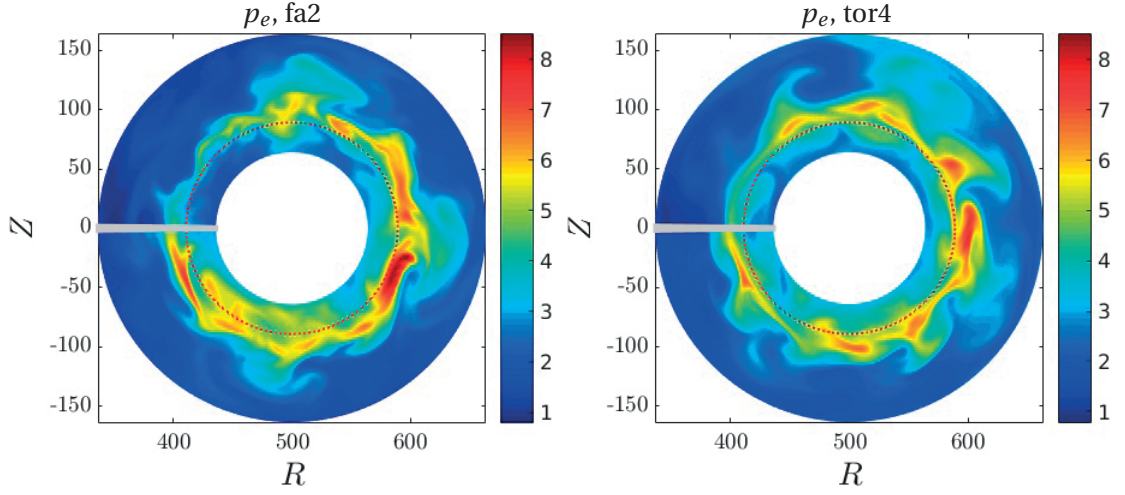


Figure 3.6 – Typical snapshot of p_e in the poloidal cross section in circular limited configuration, showing qualitative agreement between fa2 (left) and tor4 (right) GBS code versions. The dotted lines in red track the plasma source location.

Fig 3.6 shows typical snapshots of $p_e = nT_e$ in the poloidal plane for such configuration, with the fa2 case (left) and the tor4 one (right) showing turbulent structures similar in size and amplitude. The red dotted line traces the source location, and the grey line indicate the limiter position. The region from the inner boundary to the source location is discarded when analysing the simulation results, since it is physically uninteresting. The two simulations use the same set of physical parameter and a grid $N_r \times N_\theta \times N_\varphi = 128 \times 256 \times 32$, with $R_0/\rho_{s0} = 500$ and $a/R_0 \sim 0.13$.

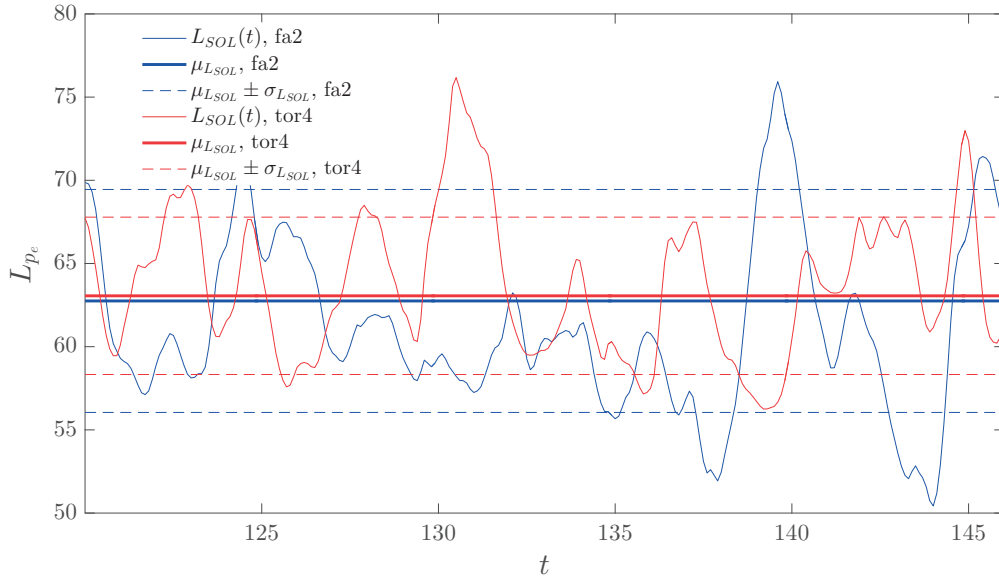


Figure 3.7 – Scrape off layer width with fa2 and tor4 case, predicted from the electron pressure exponential decay length.

Chapter 3. Numerical implementation and code verification

For a more quantitative analysis of the results, we compare the SOL width predicted by looking at the radial decay length of the plasma pressure, L_{p_e} (in ρ_{s0} units) such that $\langle p_e \rangle_{\theta, \varphi} \sim p_{e0} e^{-r/L_{p_e}}$, which is used to determine the heat flux on the tokamak wall. In figure 3.7 we plot the L_{p_e} time traces for both fa2 and tor4 during the quasi-steady state. The thick lines indicate the time average of L_{p_e} . The two version of GBS predict an almost identical average SOL width, well within the statistical uncertainties indicated by the dashed lines.

Since the main difference between the two codes lies on the evaluation of the parallel gradients, we focus on these. We Fourier decompose the fields fluctuations on a flux surface along the θ and φ directions. The Fourier representation of the parallel gradient along the parallel direction \tilde{x}_{\parallel} is:

$$\begin{aligned} \nabla_{\parallel} u &= R_0 \tilde{\nabla}_{\parallel} u = R_0 \frac{\partial u(\tilde{x}_{\parallel})}{\partial \tilde{x}_{\parallel}} = \sum_{m_{\parallel}=-N_{\parallel}/2}^{N_{\parallel}/2-1} i m_{\parallel} \frac{2\pi R_0}{\tilde{L}_{\parallel}} \hat{u}(m_{\parallel}) \exp\left(i m_{\parallel} \frac{2\pi}{\tilde{L}_{\parallel}} \tilde{x}_{\parallel}\right) \\ &= \sum_{m_{\parallel}=-N_{\parallel}/2}^{N_{\parallel}/2-1} i \frac{m_{\parallel}}{q} \hat{u}(m_{\parallel}) \exp\left(i \frac{m_{\parallel}}{q} \frac{\tilde{x}_{\parallel}}{R_0}\right) \end{aligned} \quad (3.5.2)$$

where $\tilde{L}_{\parallel} = 2\pi q R_0$ is the magnetic field line length and $N_{\parallel} = q N_{\varphi}$ is the number of points in the parallel direction. At the same time:

$$\nabla_{\parallel} u = \sum_{m_{\varphi}=-N_{\varphi}/2}^{N_{\varphi}/2-1} \sum_{m_{\theta}=-N_{\theta}/2}^{N_{\theta}/2-1} i \left(m_{\varphi} - \frac{1}{q} m_{\theta} \right) \hat{u}(m_{\varphi}, m_{\theta}) \exp(i m_{\varphi} \varphi + i m_{\theta} \theta) \quad (3.5.3)$$

By equating Eqs. (3.5.2) and (3.5.3) we obtain a relation between parallel, poloidal and toroidal modes:

$$m_{\parallel} = q m_{\varphi} - m_{\theta}, \quad \text{with} \quad \hat{u}(m_{\parallel}) = \hat{u}(m_{\varphi}, m_{\theta}) \quad (3.5.4)$$

In Fig. 3.8, the amplitude of the Fourier modes in (θ, φ) of the electron pressure, averaged in time and radial direction, i.e. $\langle |\hat{p}_e|^2(m_{\varphi}, m_{\theta}) \rangle_{r,t}$, are plotted for the fa2 (left) and tor4 (right) case. Note that the fa2 case has half of the spectrum in θ , since the parallel gradient uses half of the poloidal grid resolution. There is very good quantitative and qualitative agreement between fa2 and tor4. The central oblique line corresponds to the $m_{\parallel} = 0$ mode for which $m_{\theta} = q m_{\varphi}$. Moving away from the central axis m_{\parallel} increases. The black lines set the maximum parallel mode number allowed by the grid resolution $m_{\parallel, \max} = N_{\parallel}/2 = \pm q N_{\varphi}/2 = \pm 64$, after which we incur into numerical aliasing. The peaks visible at the top left and bottom right corners are at $m_{\parallel} = 128 = 2m_{\parallel, \max}$ and maps numerically to $m_{\parallel} = 0$. The $m_{\varphi} = 0$ line corresponds to the axisymmetric part of the spectrum, i.e. the Fourier decomposition of the background electron pressure profile in θ .

Using the relation in Eq. (3.5.4), we can sum all $|\hat{p}_e|^2(m_{\varphi}, m_{\theta})$ that map to the same m_{\parallel} . Removing the background mode at $m_{\varphi} = 0$, we can observe the parallel turbulent spectrum in Fig. (3.9) for fa2 and tor4 simulations.

3.5. Comparison with previous version of GBS in limited configuration

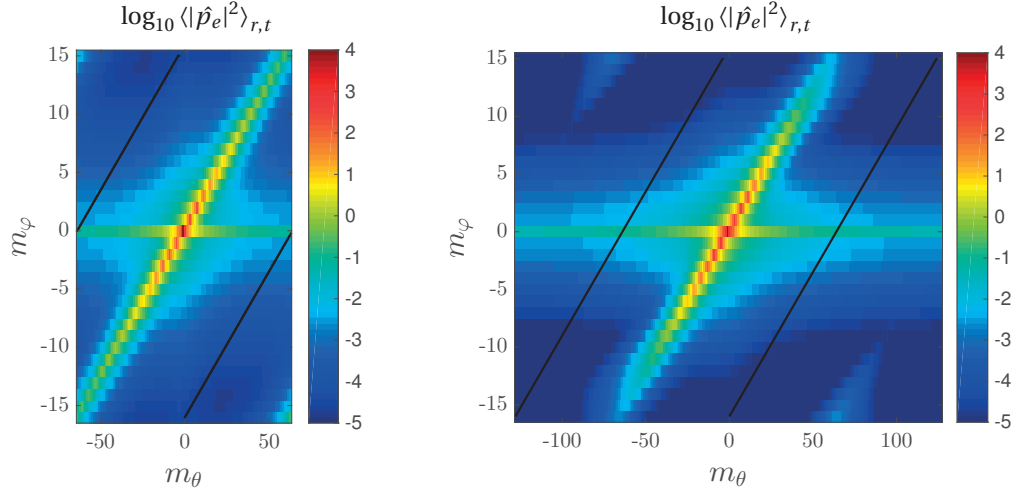


Figure 3.8 – Fourier spectrum of the parallel dynamics in θ and φ for fa2 (left) and tor4 (right) version of the code, with the fa2 version using half of the poloidal resolution and hence half of the poloidal modes. There is excellent qualitative and quantitative agreement between the two codes. The central oblique line corresponds to parallel mode number $m_{\parallel} = 0$, while the black lines trace the maximum parallel mode number $m_{\parallel} = \pm 64$ allowed by the grid resolution.

To conclude, in the case of a limited circular configuration, the tor4 version of GBS reproduces an almost identical perpendicular and parallel dynamics to the fa2 version, suggesting that the use of fourth order finite differences and staggered grid compensates for the non alignment of the toroidal grid to the magnetic field line.

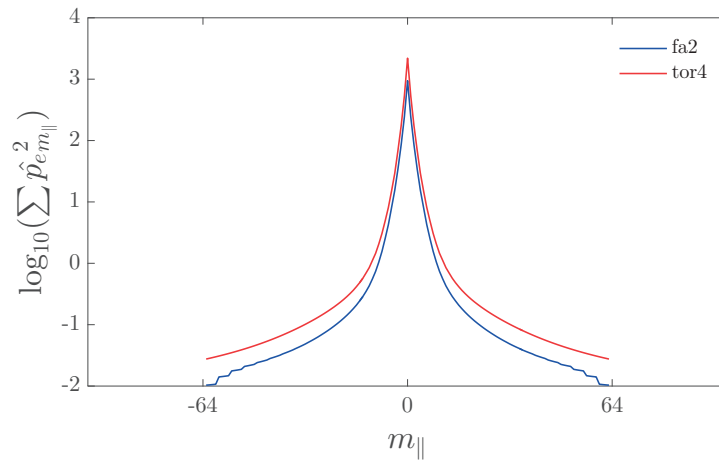


Figure 3.9 – Turbulent parallel spectrum of the electron pressure for fa2 and tor4 simulation showing good agreement.

3.6 Verification of GBS with the method of manufactured solution

We verify the new version of the GBS code using the method of manufactured solutions (MMS), a technique widely adopted by the computational fluid dynamics community [40] and first applied to fully verify a plasma turbulent code by Riva *et al.* [41] for GBS in limited magnetic configuration. We remark that the objective of the MMS is to verify that the discretised model equations have been implemented correctly in the code, not to validate the choice of the physical model. Herein we briefly present the basic idea behind the MMS and refer to Ref. [41] for a more detailed description of this methodology.

Given a model M with s its analytical solution (i.e. $M(s) = 0$), we aim at testing the implementation of a numerical discretisation of M , denoted as M_h , with h the discretisation parameter, through estimate of the error $e_h = \|s - s_h\|$, where s_h is the numerical solution of M_h (i.e. $M_h(s_h) = 0$). Since s is unknown, e_h cannot be evaluated. However, one can choose an arbitrary function u , referred to as the manufactured solution, compute the source term $S = M(u)$ analytically, solve $M_h(u_h) - S = 0$ numerically, and study $\tilde{e}_h = \|u - u_h\|$. Since the source term S is exact, the error \tilde{e}_h is due to the discretisation of M and in our case it is expected to decrease as h^4 when $h \rightarrow 0$ since we use fourth order discretisation schemes (both in space and time). In practice, one needs to compute

$$p = \frac{\ln(\tilde{e}_{rh}/\tilde{e}_h)}{\ln(r)} \quad (3.6.1)$$

where rh indicates the coarsening of the temporal and spatial mesh by a factor r , and show that $p \rightarrow 4$ for $h \rightarrow 0$.

In order to carry out the GBS code verification, we consider the diverted flux function plotted in Fig. 3.10:

$$\psi(\hat{r}, \theta) = k(2u^3 - 2u^2 - (3/2 + \cos\theta)u + 1) \quad (3.6.2)$$

where $u = (r - a/\rho_{s0})/(r_{\max} - r_{\min})$ and k controls the relative intensity of poloidal to toroidal magnetic field. In the present work we use $a = 127\rho_{s0}$, $k = 0.06$, $r_{\max} - r_{\min} = 90$ and $R_0 = 500\rho_{s0}$. We remark that, while ψ is not a solution of the Grad-Shafranov equation, it provides an analytical expression to compute the source term, $M(u) = S$.

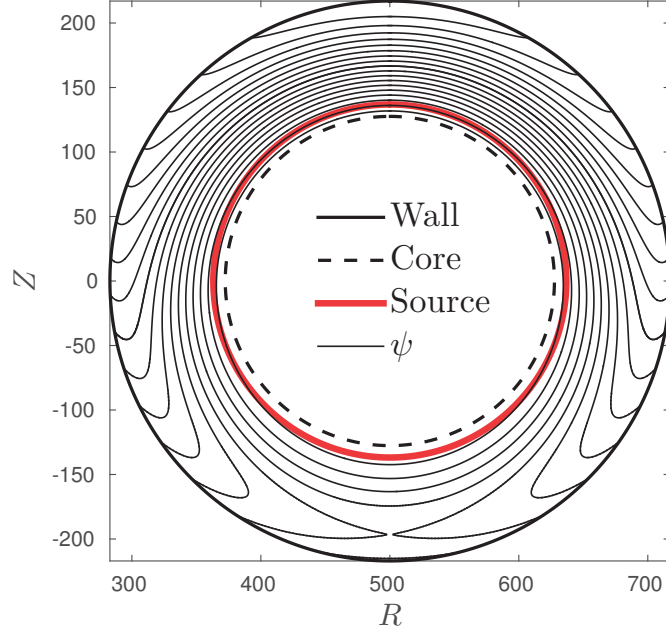


Figure 3.10 – Contour lines of the flux function in eq (3.6.2) used for GBS code verification and convergence tests.

The manufactured solution for the evolved quantities $u = n, T_{e,i}, v_{\parallel e,i}, \phi, \omega$ are chosen to have the form

$$u(r, \theta, \varphi; t) = A_u [B_u + \sin(C_u \varphi) \sin(D_u \theta) \sin(E_u t + F_u r)]$$

where A_u, B_u, C_u, D_u, E_u and F_u are arbitrary constants that may be different for each field u and are tuned to excite all the terms in the model equations.

The source term $S = M(u)$ is computed by using Mathematica software package [42], and it is added to the GBS model equation. The results of the GBS verification confirms that $p \rightarrow 4$ for $h \rightarrow 0$ for both the L_∞ (Fig. 3.11, left) and L_2 (Fig. 3.11, right) norm. These results do not include the curvature parts of gyroviscous terms, as they are implemented at second order and have been verified independently. The boundary conditions are not considered in this study.

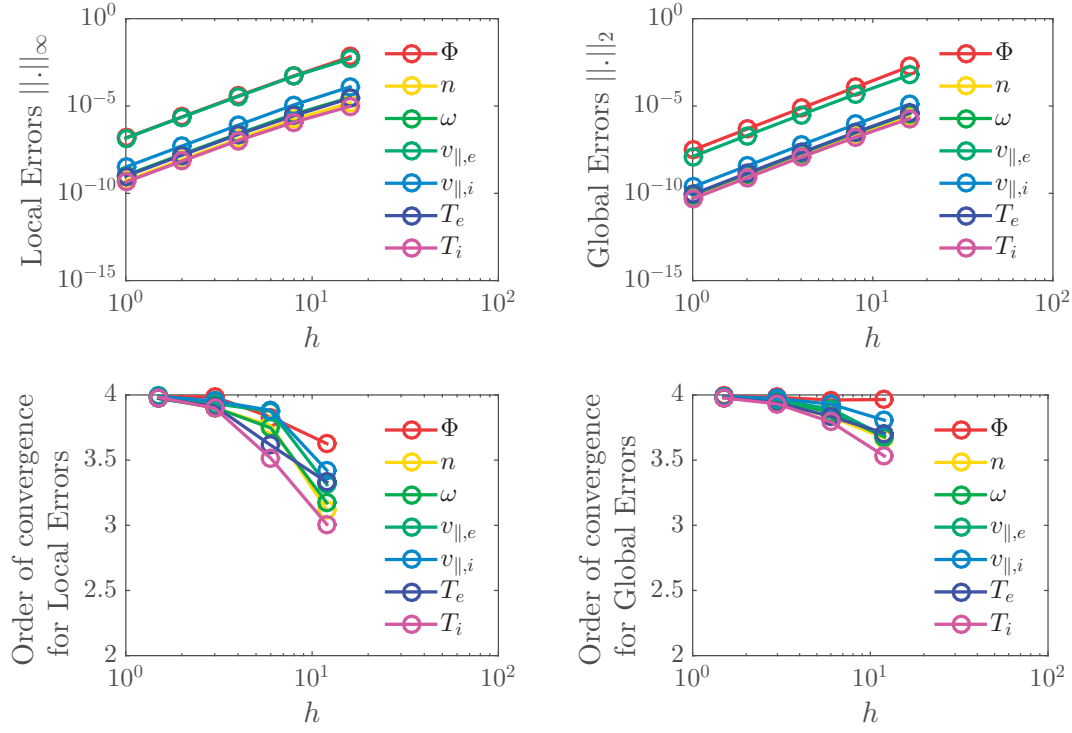


Figure 3.11 – GBS code verification by the method of manufactured solution. The error of the numerical solution to the analytical manufactured one is shown as a function of the grid size h , both in L_∞ (top left) and L_2 norm (top right). The order of convergence p tends to 4 as h decreases for both norms (bottom left and right), consistent with the 4th order finite difference numerical scheme used.

3.7 Convergence study

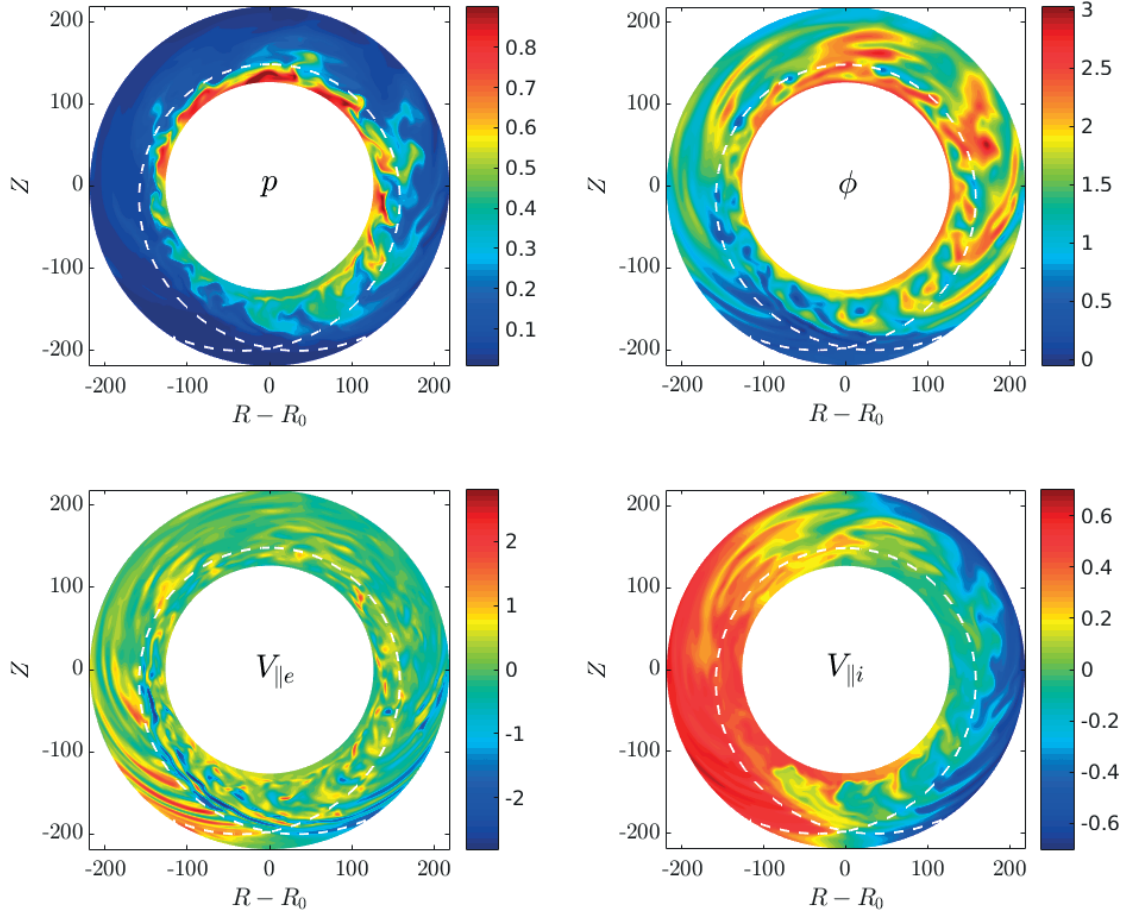


Figure 3.12 – Typical snapshot in the poloidal plane of plasma pressure ($p = n(T_e + \tau T_i)$, normalised to $n_0 T_0$), electric potential, parallel electron and ion velocities for the analytical in flux function shown Fig. 3.10. The plasma is mainly confined inside closed field line region, turbulent eddies are sheared at the separatrix (white dashed line) and form blob structures that move radially outwards and are eventually lost at the wall. The simulation with *fine* grid is considered.

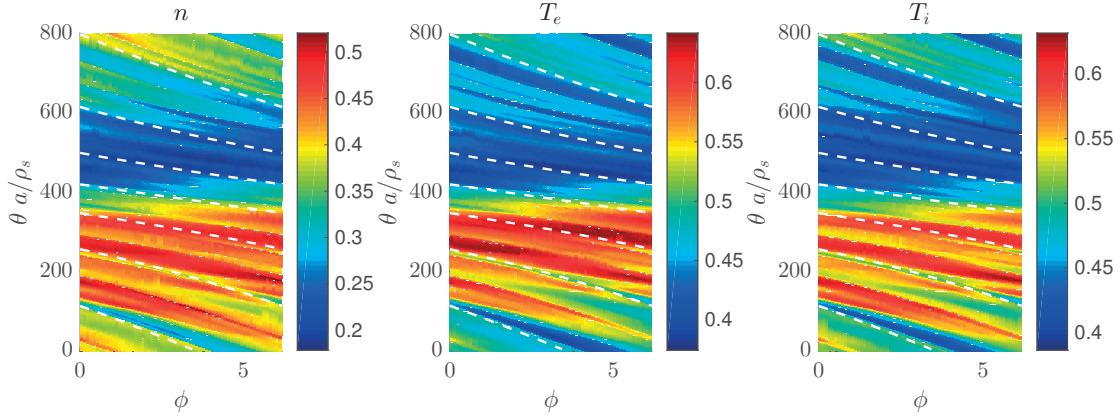


Figure 3.13 – Typical snapshot of density and electron and ion temperatures at the $r = 20$ plane inside the separatrix. Turbulence structures follow the magnetic field lines, traced by white dashed lines. The same simulation and time frame of Fig. 3.12 is considered.

The GBS convergence with respect to the grid refinement is tested with the flux function in Eq. (3.6.2). Three simulations with increasing spatial grid resolution are compared: a *coarse* simulation with grid $N_r \times N_\theta \times N_\phi = 39 \times 122 \times 16$, a *medium* simulation with grid $N_r \times N_\theta \times N_\phi = 78 \times 244 \times 32$, and a *fine* simulation with grid $N_r \times N_\theta \times N_\phi = 156 \times 488 \times 64$. The time step is chosen to grant stability. Typical snapshots from the *fine* simulation are reported in Fig. 3.12 and 3.13 showing turbulence structures that are field aligned. We perform the convergence analysis focusing on time averaged profiles, obtained after the system has reached a quasi steady state. This sets in when the inflow of density and temperature due to the sources is balanced by parallel and radial losses at the wall, resulting in fluctuations around an approximately constant value.

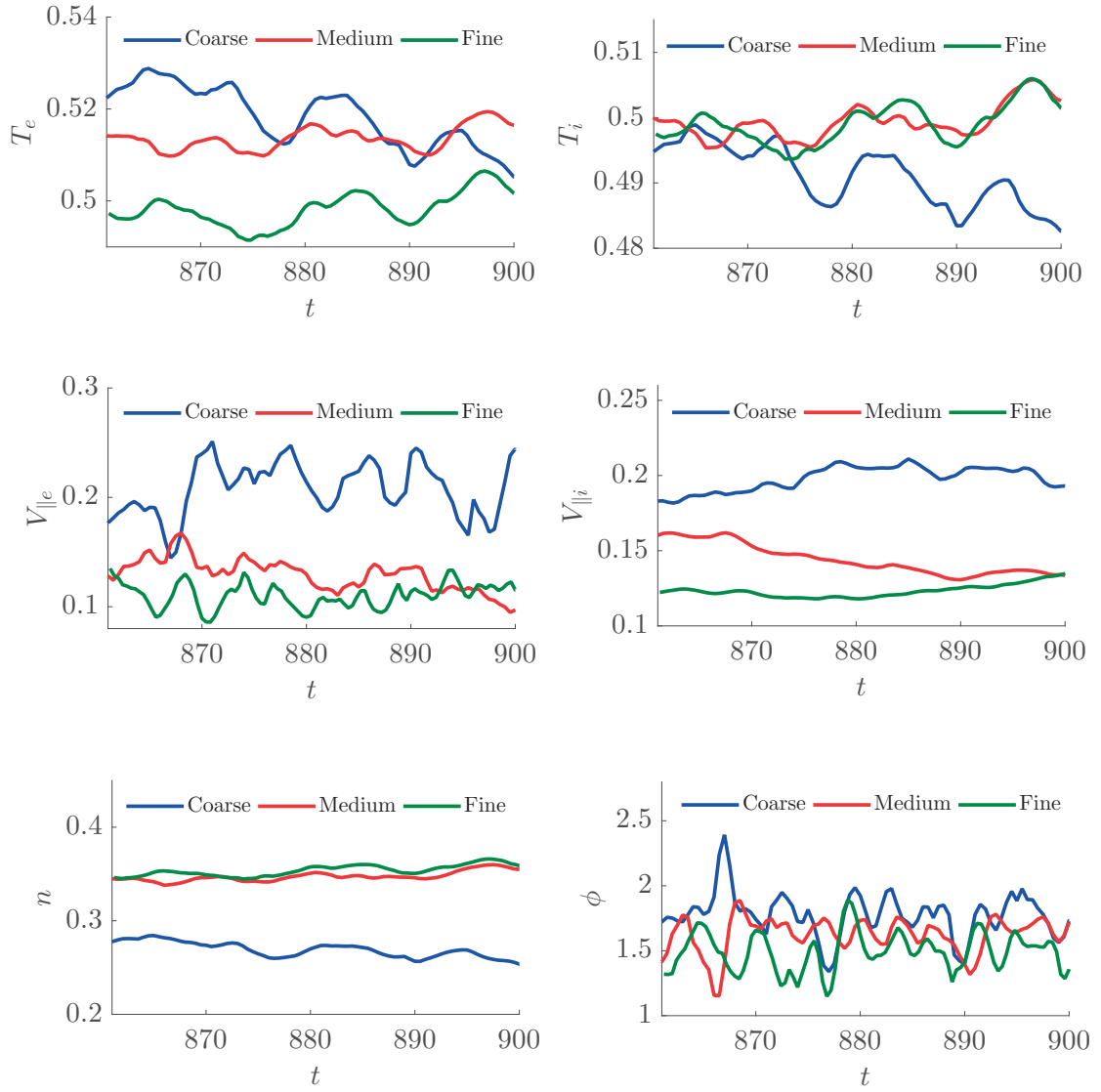


Figure 3.14 – Time trace of T_e , T_i , $v_{||i}$, $v_{||e}$, n and ϕ averaged over the 3D domain for simulation of increasing grid resolution at quasi-steady state: *coarse* grid ($N_r \times N_\theta \times N_\varphi = 39 \times 122 \times 16$), *medium* grid ($N_r \times N_\theta \times N_\varphi = 78 \times 244 \times 32$) and *fine* grid ($N_r \times N_\theta \times N_\varphi = 156 \times 488 \times 64$).

Fig. 3.14 shows the averaged values of T_e , T_i , $v_{||e}$, $v_{||i}$, ϕ and n over the entire domain during quasi-steady state. The plots show qualitatively the convergence of the code results with the grid resolution, inasmuch as the time traces of *fine* and *medium* are close to each other, while the *coarse* grid traces are slightly off. Convergence is evident for n , T_i , $v_{||e}$ and $v_{||i}$. For ϕ the three average values are close to each other, being in overall agreement. Finally, for the electron temperature T_e the trend displayed by the *fine* and *medium* simulations is similar, although the average values differ slightly, and the *coarse* T_e profile oscillates somewhere in between.

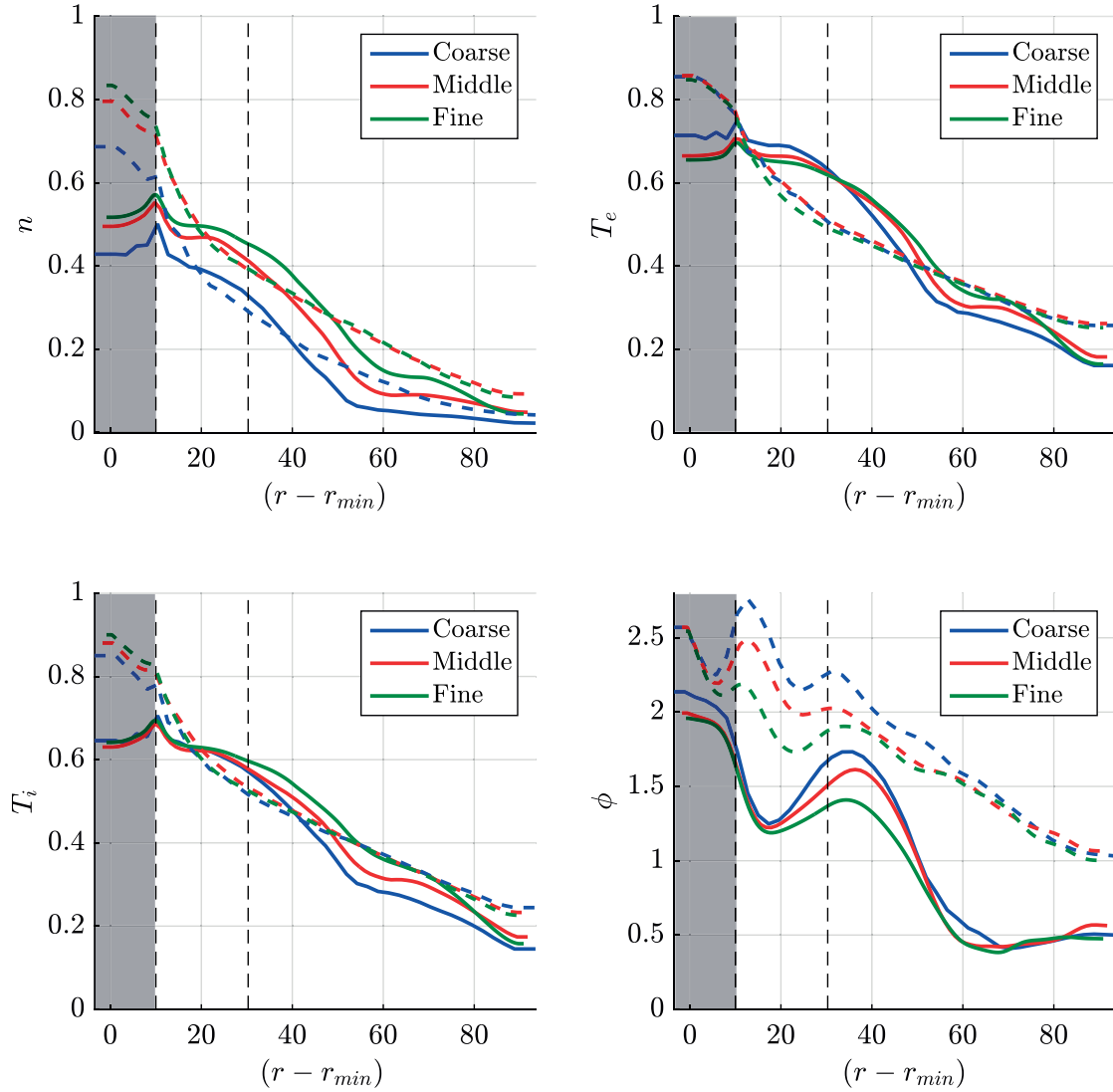


Figure 3.15 – Toroidal and temporal average of radial profiles at the LFS (solid lines) and HFS (dashed lines) for n , T_e , T_i , ϕ resulting from GBS simulations carried out for the three different resolutions in Fig. 3.14. The vertical lines at $r - r_{min} \sim 30$ show the radial position of the separatrix, while the shaded area is the buffer zone between the inner radial boundary and the plasma source position.

The toroidal and time averaged radial profiles of n , T_e , T_i and ϕ , which are often used to predict SOL width (see e.g. [16]), are shown in Fig. 3.15 on the equatorial midplane at the low field side (LFS) and high field side (HFS), with a solid and dashed line, respectively. The vertical dashed line at $r - r_{min} \sim 30$ indicates the separatrix location. The shaded region that extends from the inner radial boundary to the source location is a buffer volume, which is not subject of physics investigations. The three simulations show qualitative agreement for all fields with clear convergence pattern for n , T_e , T_i .

As an indicator of the convergence of the $v_{\parallel e}$ and $v_{\parallel i}$ fields, we analyse their time and toroidally

averaged profiles along the separatrix. Since we are not using flux coordinates, the values on the separatrix are obtained by performing a linear interpolation between the grid points. In Fig. 3.16 the averaged values of $v_{\parallel e}$ and $v_{\parallel i}$ are plotted against s , a coordinate that maps the separatrix and it is normalised to ρ_{s0} . We impose $s = 0$ at the divertor plate at the HFS, the coordinate s increases moving along the inner divertor leg. The value of s at the X-point is indicated by the first vertical line. Larger values of s parametrise the loop around the separatrix from the HFS to the LFS until the X-point position (indicated by the second vertical line). Finally, s tracks the outer leg up to the wall. The results of the three simulations are again in good agreement and show convergence with the refinement of the grid, in particular for $v_{\parallel i}$.

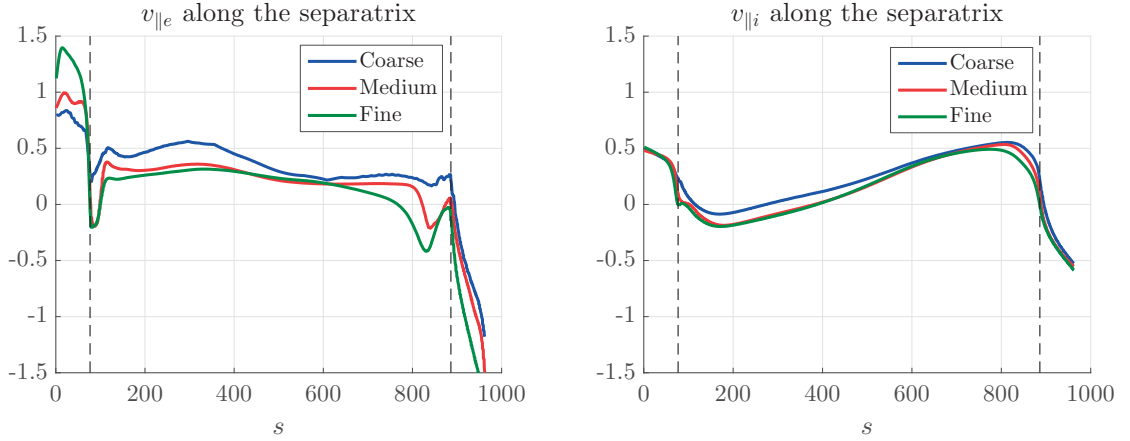


Figure 3.16 – Toroidal and time average of the velocities profiles as a function of s , a coordinate that maps the separatrix from the HFS to the LFS, for the three different resolutions in Fig. 3.14

To conclude the convergence analysis with a quantitative evaluation, we consider the time and toroidally averaged profiles of all fields in the (r, θ) poloidal plane. We use as index of convergence the distance, in the sense of the L_2 norm on the poloidal (r, θ) plane, between the *coarse* and the *fine* simulations and between the *medium* and the *fine* ones. This is represented in Fig. 3.17, where h/h_0 indicates the ratio of the coarser grids to the refined grid spacing. The distance to the refined simulation is smaller for the *medium* grid than for the *coarse* grid for all fields, with an indicative order of convergence, evaluated from the slope of the lines in Fig. 3.17 ranging from approximately 2 for ω and ϕ , to approximately 5 for n .

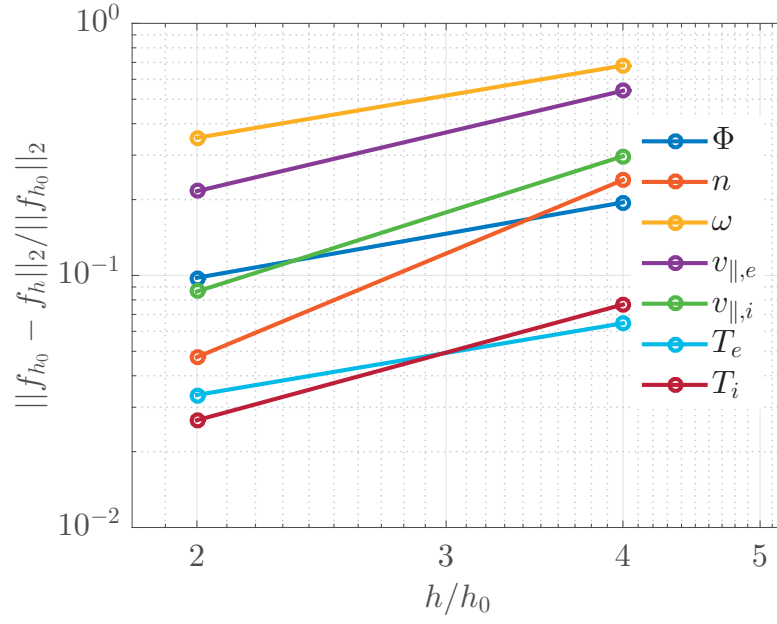


Figure 3.17 – Quantitative estimate of code convergence. The toroidal and temporal average of $\phi, n, \omega, v_{||,e}, v_{||,i}, T_e, T_i$ for the *coarse* and *medium* grid is compared to the *fine* grid, by computing the L_2 norm in (r, θ) of their difference. The parameter h_0 denotes the grid spacing of the *fine* grid and h the grid spacing of the coarser grids, so that $h/h_0 = 4$ and $h/h_0 = 2$ for the *coarse* and *medium* grid, respectively.

4 Blobs

The plasma dynamics in the periphery of magnetic fusion devices is characterised by the presence of blobs. These are coherent structures of enhanced plasma pressure with respect to the background value, spatially localised in the plane perpendicular to the magnetic field and elongated along it [43]. Because of their shape, blobs are also known as filaments. Blobs detach from the main plasma and move radially outwards, making turbulence at the edge of fusion devices intermittent and significantly contributing to the radial transport mechanism in the SOL. Boedo *et al.* [44] estimated that $\sim 50\%$ of radial transport is due to blobs. Blobs have been observed in tokamaks (e.g. in the Caltech Research Tokamak [45], Alcator C-Mod [46], JET [47], JT-60U [48], Tore Supra [49], TCV [50]), stellarators (see, e.g., [51] [52]), reversed field pinches [53], and basic plasma devices (e.g. in LAPD [54] and in TORPEX [55]). They can lead to enhanced intermittent heat flux on the main vessel wall, possibly damaging radio frequencies antennas, wall tiles, and causing sputtering of impurities [56], [57], [58]. On the other hand the presence of blobs can be desirable as the enhanced radial transport can lead to a widening of the SOL width and, consequently, to a reduction of the power deposited on the divertor plates.

It is generally believed that blobs are the result of the non-linear saturation of edge localised interchange-like instabilities, with the density fluctuation sheared apart by the $\mathbf{E} \times \mathbf{B}$ velocity and detached from the main plasma, as observed in JET [59] and in TORPEX [55], and as described by 2D fluid models as in [60].

Once detached from the main plasma, the blob moves radially outwards. An extensive review of the literature on blob motion can be found in Ref. [43]. The radial motion results from the vertical charge separation inside the blob stemming from the effect of the curvature and of the ∇B drifts. The charge separation leads to an electric field and its associated $\mathbf{E} \times \mathbf{B}$ drift that causes the blob to move radially outwards. This basic mechanism of radial motion is confirmed by a series of blob studies conducted on the TORPEX device, where blobs radial velocity was shown in agreement with the $\mathbf{E} \times \mathbf{B}$ drift [61], [62] and by numerical simulations of seeded blobs (see, e.g., [63], [64], [65], [66]). Also using simulations of a single seeded blob, the effect of the X-point on blob motion has been investigated [67] using a 3D version of BOUT++ to reproduce the experimental work of Avino *et al.* [62] on TORPEX. In addition, the magnetic shear effect has been studied as a proxy for the X-point and has been shown to

improve particle confinement and reduce radial transport [68].

The goal of the present chapter is to use the results of a full-turbulence simulation of the tokamak periphery to present the first detailed self-consistent analysis of blob radial motion in a diverted geometry. Only very recently the study of blob motion has been approached by using 3D full-turbulent self-consistent simulations. Results of a full 3D turbulent simulation with the XGC1 gyrokinetic code of a DIII-D H-mode discharge have been used to carry out an initial investigation of the blob properties [70]. Considering a self-consistent simulation of a TCV discharge carried out with the GBS code in limited configuration, Nespoli *et al.* [71] implemented a pattern-recognition algorithm for blob tracking and showed good agreement of the blob velocity with the theoretical scalings. The present chapter extends the work in Ref. [71], and compares the simulation results with the theoretical scalings developed to predict blob velocity in the presence of an X-point ([24, 72]). In diverted configuration, as pointed out also by a more recent work on ASDEX Upgrade [73] the collisionality can affect the blob velocity scaling. Our results focus on the high collisionality regime and, depending on the blob size, we identify the polarization or the parallel current as balance mechanisms to the curvature drive. In both cases, our simulations results are in good agreement with the theoretical scalings.

The present chapter is organised as follows. Leveraging previous derivations, we provide the analytical scaling to estimate the velocity of blobs in diverted configurations in Sec. 4.1. Then, Sec. 4.2 presents the diagnostic tools that allow us to study the velocity of blobs in the double-null GBS simulations. Finally, the simulation results of the blob radial velocity are compared with the analytical scaling in Sec. 4.3.

4.1 The two-region model for the blob dynamics in diverted configuration

Analytical predictions of the blob radial velocity can be obtained by using simplified 2D two-fluid models, describing the plasma dynamics in the poloidal plane. These models usually consider continuity equation, a charge conservation law, and a closure for the parallel current. Examples can be found in [74], [56], [61].

When one wants to account for the X-point effect, the most investigated of such analytical 2D models, is the two-region model [24]. This model separates the upstream region, where the unfavourable curvature of the magnetic field provides most of the drive for the blob radial motion, and the divertor region, where the magnetic shear causes the blob to elongate in the radial and to squeeze in the vertical directions, facilitating the damping of the blob charge separation by cross-field currents (see Fig. 4.1, the two region are labelled 1 and 2, respectively).

Here, we follow Ref. [24] to re-derive the two-region model and, although our results are qualitatively similar to the ones obtained therein, we find quantitative differences that affect the comparison of analytical and simulation results (see Sec. 4.3). Starting from the drift-reduced Braginskii's equations for density (Eq. (2.1.11)) and vorticity (Eq. (2.1.16)) in GBS

4.1. The two-region model for the blob dynamics in diverted configuration

dimensionless units, the two-region model by Myra reads:

$$\begin{aligned}
\frac{\partial \omega_1}{\partial t} + \frac{R_0}{\rho_{s0}} [\phi_1, \omega_1] &= \frac{1}{n_1} \nabla_{\parallel} J_{\parallel,1} + \frac{2T_{e,1}}{n_1} C(n_1) \\
\frac{\partial n_1}{\partial t} + \frac{R_0}{\rho_{s0}} [\phi_1, n_1] &= 0 \\
\frac{\partial \omega_2}{\partial t} + \frac{R_0}{\rho_{s0}} [\phi_2, \omega_2] &= \frac{1}{n_2} \nabla_{\parallel} J_{\parallel,2} \\
\frac{\partial n_2}{\partial t} + \frac{R_0}{\rho_{s0}} [\phi_2, n_2] &= 0
\end{aligned} \tag{4.1.1}$$

In the density equations, with respect to the drift-reduced Braginskii density equation (Eq. (2.1.11)), the parallel streaming and magnetic curvature terms are neglected, as they are smaller than the dominant $\mathbf{E} \times \mathbf{B}$ drift. In the vorticity equations, the parallel terms associated with the polarisation current are neglected and, in the divertor region, the interchange drive is also discarded. The large aspect ratio approximation is used, allowing us to drop the normalised magnetic field strength B that appears in [24].

By balancing the divergence of J_{\parallel} with the resistive term in Ohm's law $J_{\parallel} = -\nabla_{\parallel} \phi / \nu$ in the electron velocity equation (2.1.12), in the upstream region we approximate

$$\nabla_{\parallel} J_{\parallel,1} = \frac{\phi_1 - \phi_2}{\nu L_1^2} \tag{4.1.2}$$

where L_1 is length of the magnetic field line from the equatorial midplane to the entrance of the divertor region (normalised to R_0). In the divertor region, a closure for the parallel current can be obtained by integrating the divergence of the parallel current along the parallel direction from the interface with the upstream region to the sheath entrance, i.e.

$$\int_2^{sh} \nabla_{\parallel} J_{\parallel,2} dl = J_{\parallel} \Big|_2^{sh} = -\frac{\phi_1 - \phi_2}{\nu L_1} + \frac{n_2 c_{s,2}}{T_{e,2}} (\phi_2 - \phi_f) \tag{4.1.3}$$

where the sheath current $J_{\parallel} = n c_s (1 - \exp(\lambda - \phi / T_e))$ is linearised around $\phi \sim \phi_f = \lambda T_e / e$. With the current closures and evaluating the curvature terms at the outboard midplane (using Eq. (2.2.29)), the two-region model becomes:

$$\left(\frac{\partial}{\partial t} + \frac{R_0}{\rho_{s0}} \mathbf{v}_{E,1} \cdot \nabla \right) \nabla_{\perp}^2 \phi_1 = \sigma_1 \frac{\phi_1 - \phi_2}{n_1} - \frac{\beta}{n_1} \frac{1}{r} \frac{\partial n_1}{\partial \theta} \tag{4.1.4}$$

$$\left(\frac{\partial}{\partial t} + \frac{R_0}{\rho_{s0}} \mathbf{v}_{E,1} \cdot \nabla \right) n_1 = 0 \tag{4.1.5}$$

$$\left(\frac{\partial}{\partial t} + \frac{R_0}{\rho_{s0}} \mathbf{v}_{E,2} \cdot \nabla \right) \nabla_{\perp}^2 \phi_2 = -\sigma_2 \frac{\phi_1 - \phi_2}{n_2} + \alpha (\phi_2 - \phi_f) \tag{4.1.6}$$

$$\left(\frac{\partial}{\partial t} + \frac{R_0}{\rho_{s0}} \mathbf{v}_{E,2} \cdot \nabla \right) n_2 = 0 \tag{4.1.7}$$

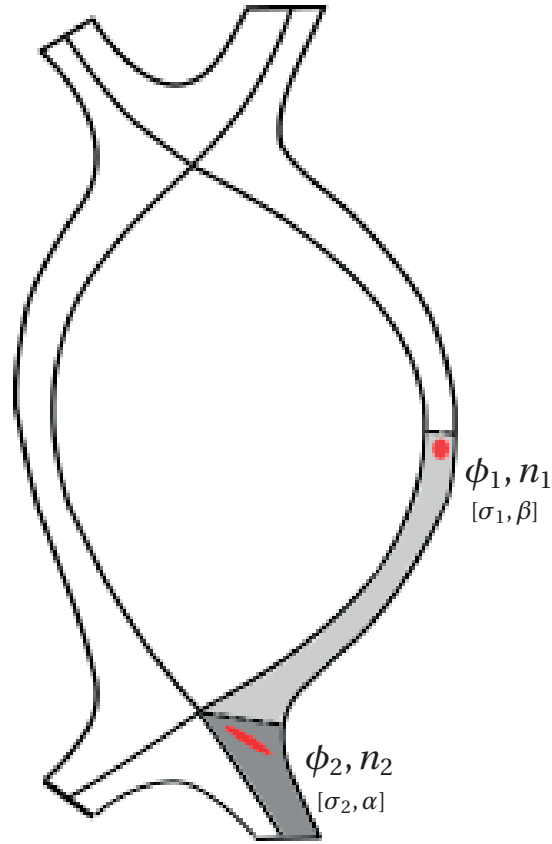


Figure 4.1 – Schematic illustration of the two region model. Region 1 (light gray) correspond to the outboard low field side, where the curvature drive β is active, and extend from midplane to the X-point region. Here the flux expansion is maximal and causes the blobs to elongate and tilt due to field line mapping, disconnecting region 1 from the divertor, i.e region 2 in darker gray, characterised by the current to the sheath α . The coefficients σ_1 and σ_2 in Eqs. (4.1.4)-(4.1.6) regulate the parallel current flow between the two regions and depend on the resistivity ν .

4.1. The two-region model for the blob dynamics in diverted configuration

having defined

$$\sigma_1 = \frac{1}{\nu L_1^2}, \quad \sigma_2 = \frac{1}{\nu L_1 L_2}, \quad \beta = 2\rho_{s,1}^2, \quad \alpha = \frac{1}{\rho_{s,2} L_2} \quad (4.1.8)$$

with L_2 magnetic field line length from X-point to wall (in R_0 units). In addition, in Eqs. (4.1.4)-(4.1.7), the Poisson brackets terms are rewritten as advective terms due to the $\mathbf{E} \times \mathbf{B}$ velocity \mathbf{v}_E , for example

$$[\phi, \omega] = \mathbf{b} \cdot \nabla \phi \times \nabla \omega = \mathbf{v}_E \cdot \nabla \omega \quad (4.1.9)$$

where \mathbf{v}_E is in c_{s0} units and ∇ is in ρ_{s0} units.

In order to make analytical progress in the analysis of the blob velocity, we linearise the two-region model. We indicate the radial ψ and binormal χ directions ($\mathbf{e}_\chi = \mathbf{b} \times \mathbf{e}_\psi$) with x and y , respectively (they are normalised to ρ_{s0} units) and Fourier decompose $\phi_{1,2}$ and $n_{1,2}$ along the y direction, allowing for different wavenumbers in the two regions, i.e.

$$\phi_1 = \delta\phi_1(x)e^{-i\omega t + ik_1 y}, \quad n_1 = n_{0,1}(x) + \delta n_1(x)e^{-i\omega t + ik_1 y} \quad (4.1.10)$$

$$\phi_2 = \delta\phi_2(x)e^{-i\omega t + ik_2 y}, \quad n_2 = n_{0,2}(x) + \delta n_2(x)e^{-i\omega t + ik_2 y} \quad (4.1.11)$$

We note that the background density is given by $n_{bg} = n_0 - \delta n$ and the peak blob density by $n_{peak} = n_0 + \delta n$ (see Fig. 4.2).

We then approximate $\nabla_\perp^2 \delta\phi_1 \simeq -k_1^2 \delta\phi_1$ (assuming the blob electric potential to vary along the x direction on longer scales than along y , consistently with the physical picture of a dipole generating in y), and we work in the $\mathbf{E} \times \mathbf{B}$ frame of reference, so that the background equilibrium potentials $\phi_{0,1}, \phi_{0,2}$ vanish, assuming $\phi_{0,1} = \phi_{0,2} = \text{const}$. We then obtain the following linearised two-region model

$$i\omega k_1^2 \delta\phi_1 = \frac{\sigma_1}{n_{0,1}} (\delta\phi_1 - \delta\phi_2) - i\beta k_1 \frac{\delta n_1}{n_{0,1}} \quad (4.1.12)$$

$$-i\omega \delta n_1 - \frac{R_0}{\rho_{s0}} i k_1 \delta\phi_1 \frac{\partial n_1}{\partial x} = 0 \quad (4.1.13)$$

$$i\omega k_2^2 \delta\phi_2 = \frac{\sigma_2}{n_{0,2}} (\delta\phi_2 - \delta\phi_1) + \alpha \delta\phi_2 \quad (4.1.14)$$

$$-i\omega \delta n_2 - \frac{R_0}{\rho_{s0}} i k_2 \delta\phi_2 \frac{\partial n_2}{\partial x} = 0 \quad (4.1.15)$$

where we made use of Eqs. (4.1.9) to write $\mathbf{v}_{E,j} \cdot \nabla \approx -i k_j \delta\phi_j \frac{\partial}{\partial x}$.

Eq. (4.1.13) allows us to express δn_1 as a function of $\delta\phi_1$, that is

$$\delta n_1 = -\frac{1}{\omega} \frac{R_0}{\rho_{s0}} k_1 \frac{\partial n_1}{\partial x} \delta\phi_1. \quad (4.1.16)$$

Note that we allowed the background density to vary in the radial direction, $n_{0,j} = n_{0,j}(x)$

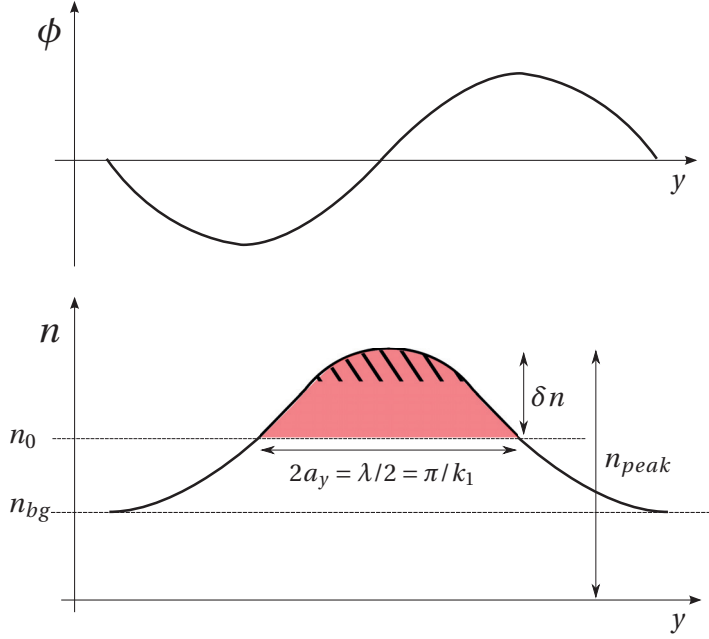


Figure 4.2 – Blob cut along the vertical direction, y , showing potential and density wavelike profiles as expressed in Eqs. (4.1.10)-(4.1.11) and their relation to the blob density peak n_{peak} and the density background value n_{bg} . We also show the link between wavenumber k_1 and blob radius a_y computed with the Half Width Half Maximum technique detailed in Sec. 4.2, i.e. $k_1 = \pi/(2a_y)$.

in Eqs. (4.1.10)-(4.1.11), in the case of uniform background we would have $\partial_x n_j = \partial_x \delta n_j = \delta n_j / a_x$, with a_x half of the radial blob size. Eq. 4.1.16 can be substituted in Eq. (4.1.12) to obtain:

$$\omega^2 \delta \phi_1 = -i \frac{\sigma_1}{n_{0,1} k_1^2} \omega (\delta \phi_1 - \delta \phi_2) + \frac{\beta}{\rho_*} \frac{1}{n_{0,1}} \frac{\partial n_1}{\partial x} \delta \phi_1 \quad (4.1.17)$$

with $\rho_* = \rho_{s0} / R_0$. Introducing the characteristic frequencies $\omega_{\sigma,j} = \sigma_j / (n_{0,j} k_1^2)$ and $\gamma_{mhd}^2 = -\beta \rho_* \partial_x n_1 / n_{0,1}$, this can be written as

$$\omega^2 \delta \phi_1 = -i \omega_{\sigma,1} \omega (\delta \phi_1 - \delta \phi_2) - \gamma_{mhd}^2 \delta \phi_1 \quad (4.1.18)$$

and, using the same notation, Eq. (4.1.14) becomes

$$\omega \delta \phi_2 = i \omega_{\sigma,2} \frac{k_1^2}{k_2^2} (\delta \phi_1 - \delta \phi_2) - i \omega_{\alpha,2} \delta \phi_2 \quad (4.1.19)$$

where $\omega_{\alpha,2} = \alpha / k_2^2$. From Eqs. (4.1.18) and (4.1.19), the following dispersion relation is derived:

$$\omega^2 + \gamma_{mhd}^2 + \frac{(i \omega_{\sigma,1} \omega)(\omega + i \omega_{\alpha,2})}{\omega + i \omega_{\sigma,2} k_1^2 / k_2^2 + i \omega_{\alpha,2}} = 0 \quad (4.1.20)$$

4.1. The two-region model for the blob dynamics in diverted configuration

	GBS	Physical	Phys. Myra
γ_{mhd}^2	$-2\rho_{s,1}^2 \frac{R_0}{\rho_{s0}} \frac{1}{n_{0,1}} \frac{\partial n_1}{\partial x}$	$-2 \frac{\Omega_0^2 \tilde{\rho}_{s,1}^2}{R_0} \frac{1}{\tilde{n}_{0,1}} \frac{\partial \tilde{n}_1}{\partial \tilde{x}}$	$-2 \frac{\tilde{\Omega}^2 \tilde{\rho}_s^2}{\tilde{R}} \partial_{\tilde{x}} \ln n_1$
$\omega_{\sigma,j}$	$(\nu L_1 L_j n_{0,j} k_1^2)^{-1}$	$\frac{\Omega_0^2 m_i \sigma_{\parallel}}{e^2 \tilde{L}_1 \tilde{L}_j \tilde{n}_{0,j} \tilde{k}_1^2}$	$\frac{\tilde{\Omega}^2 m_i \sigma_{\parallel}}{e^2 \tilde{L}_{\parallel}^2 \tilde{n}_1 \tilde{k}_1^2}$
$\omega_{\alpha,j}$	$(\rho_{s,2} L_2 k_j^2)^{-1}$	$\frac{\Omega_0}{\tilde{\rho}_{s,2} \tilde{L}_2 \tilde{k}_j^2}$	$\frac{2\tilde{\Omega}}{\tilde{\rho}_s \tilde{L}_{\parallel} \tilde{k}_j^2}$

Table 4.1 – Comparison of the characteristic frequencies of the two-region model as derived in the present work and as derived by Myra *et al.* [24]. In the first column the dimensionless frequencies are written in GBS dimensionless units, the second column translates them in physical units and, finally, the third column reproduces the expressions from the referenced article. The physical expression $\omega_{\sigma,j}$ are evaluated imposing $\nu = e^2 n_0 R_0 / (m_i \sigma_{\parallel} c_{s0})$, with σ_{\parallel} parallel conductivity.

Since $k_2 = k_1 / \varepsilon_{\chi}$, with ε_{χ} inversely proportional to the flux tube fanning, Eq. (4.1.20) becomes

$$\omega^2 + \gamma_{\text{mhd}}^2 + \frac{(i\omega_{\sigma,1}\omega)(\omega + i\varepsilon_{\chi}^2\omega_{\alpha,1})}{\omega + i\varepsilon_{\chi}^2\omega_{\sigma,2} + i\varepsilon_{\chi}^2\omega_{\alpha,1}} = 0 \quad (4.1.21)$$

In table 4.1 we compare the characteristic frequencies we have derived with the ones in Myra *et al.* [24], in physical units. We note that with the hypothesis of $\tilde{L}_1 = \tilde{L}_2$, $\tilde{n}_1 = \tilde{n}_2$, and $\tilde{\rho}_{s,1} = \tilde{\rho}_{s,2}$ (i.e. $\tilde{T}_{e,1} = \tilde{T}_{e,2}$), our expressions in physical units reduce to the large aspect ratio limit of the ones derived in ref. [24]. For ω_{σ} , we impose $\nu = e^2 n_0 R_0 / (m_i \sigma_{\parallel} c_{s0})$.

Dividing Eq. (4.1.21) by γ_{mhd}^2 , we obtain

$$1 + \hat{\omega}^2 + \frac{i\hat{\omega}\Theta(\hat{\omega} + i\varepsilon_{\chi}^2\Theta)}{\Lambda(\hat{\omega} + i\varepsilon_{\chi}^2\Theta) + i\varepsilon_{\chi}^2 \frac{\omega_{\sigma,2}}{\omega_{\sigma,1}} \Theta} = 0 \quad (4.1.22)$$

where the normalised frequency $\hat{\omega} = \omega / \gamma_{\text{mhd}}$ is introduced as well as the parameters that mostly affect the blob motion, i.e. $\Theta = \omega_{\alpha,1} / \gamma_{\text{mhd}}$ and $\Lambda = \omega_{\alpha,1} / \omega_{\sigma,1}$. The Θ and Λ parameters describe, respectively, the importance of the sheath resistivity with respect to the interchange drive and with respect to the plasma resistivity. As we will see shortly, $\Theta = \omega_{\alpha,1} / \gamma_{\text{mhd}}$ can be reinterpreted as proxy of the blob size, in fact $\omega_{\alpha,1}$ contains the poloidal wavenumber $k_1 = \pi / (2a_y)$ (see Fig. 4.2) while γ_{mhd} contains information on the blob radial size through $\partial_x n_1$. For this reason we approximate $\partial_x n_1$ with $\Delta_x n_1 / a_x$, where, in the general case of background density varying in x over the blob extension, $\Delta_x n_1 \neq \delta n_1$ and a_x , unlike a_y , is not the size at the half maximum but rather half of the radial extension of the entire perturbation above background. Let us

estimate the values of Λ and Θ as functions the blob properties

$$\Lambda = \frac{n_1 \alpha}{\sigma_1} = \frac{\omega_{\alpha,1}}{\omega_{\sigma,1}} = \nu n_1 \frac{L_1^2}{L_2 \rho_{s,2}} \quad (4.1.23)$$

$$\Theta = \frac{\omega_{\alpha,1}}{\gamma_{\text{mhd}}} = \left[\frac{k_1^{-4} a_x}{2 \rho_{s,1}^2 \rho_{s,2}^2 L_2^2 \frac{\Delta_x n_1}{n_{0,1}} \rho_*^{-1}} \right]^{\frac{1}{2}} \stackrel{\text{fig 4.2}}{=} \left[\frac{(2a_y/\pi)^{\frac{4}{5}} a_x^{\frac{1}{5}}}{\left(2 \rho_{s,1}^2 \rho_{s,2}^2 L_2^2 \frac{\Delta_x n_1}{n_{0,1}} \rho_*^{-1} \right)^{\frac{1}{5}}} \right]^{\frac{5}{2}} = \left(\frac{a_b}{a^*} \right)^{\frac{5}{2}} = \hat{a}^{\frac{5}{2}} \quad (4.1.24)$$

where $a_b = (2a_y/\pi)^{4/5} a_x^{1/5}$ is used to estimate of the blob size, while a^* is the reference size, which is given by the balance between the curvature drive β and the sheath current α (defined in Eq. (4.1.8)):

$$a^* = \left(2 \rho_{s,1}^2 \rho_{s,2}^2 L_2^2 \frac{\Delta_x n_1}{n_{0,1}} \rho_*^{-1} \right)^{\frac{1}{5}} = \left(\frac{\beta}{\alpha^2} \frac{\Delta_x n_1}{n_{0,1}} \rho_*^{-1} \right)^{\frac{1}{5}} \quad (4.1.25)$$

We finally derive an analytical prediction for the blob radial velocity, as a function of the normalised blob size \hat{a} (or Θ) and the collisionality Λ . As a first step, we express the radial velocity v_x as a function of the frequency ω . Since the radial blob motion is due to the $\mathbf{E} \times \mathbf{B}$ drift, using the linearised continuity equation (4.1.13), one can write:

$$v_x = v_E = \text{Im}(\omega) \frac{\rho_{s0}}{R_0} \frac{\delta n_1}{\Delta_x n_1} a_x \quad (4.1.26)$$

as $\partial_x n_1 = \Delta_x n_1 / a_x$, and $v_E = -ik_1 \delta \phi_1$. Then, we choose a reference blob velocity such that the normalised velocity $\hat{v} = v_x / v^*$ reads

$$\hat{v} = \text{Im}(\hat{\omega}) \hat{a}^{1/2} \quad (4.1.27)$$

This reference velocity is

$$v^* = v_x \Big|_{\omega=i\gamma_{\text{mhd}}} \hat{a}^{-1/2} = \gamma_{\text{mhd}} \frac{\rho_{s0}}{R_0} \frac{\delta n_1}{\Delta_x n_1} a_x \hat{a}^{-1/2} = \rho_{s,1} \left[8 \frac{\delta n_1^5}{\Delta_x n_1^2 n_{0,1}^3} \left(\frac{\pi a_x}{2a_y} \right)^2 \rho_{s,1} \rho_{s,2} L_2 \rho_*^2 \right]^{\frac{1}{5}} \quad (4.1.28)$$

One can immediately see that since $\hat{\omega} = \omega / \gamma_{\text{mhd}}$ the second to last expression in Eq. (4.1.28) combined with (4.1.26) gives directly the desired expression for the normalised velocity in Eq. (4.1.27). The chosen reference velocity can be interpreted as the radial velocity of blob of size $\hat{a} = 1$, when the Resistive Ballooning is the dominant instability, for which the drive in region 1 is balanced by the inertia in the same region (i.e. the first and last terms in Eqs. (4.1.18)) and $\omega_{\text{RB}} = i\gamma_{\text{mhd}}$.

Table 4.2 summarises the differences between our expressions for Λ , a_b , a^* , and v^* , and the ones in Ref. [24]. In the physical expression for Λ the electron to ion collision frequency

4.1. The two-region model for the blob dynamics in diverted configuration

	GBS	Physical	Phys. Myra
Λ	$\nu n_1 \frac{L_1^2}{L_2 \rho_{s,2}}$	$\frac{\nu_j^{e/i} \tilde{L}_1^2}{\tilde{\rho}_{s,2} \Omega_{0,e} \tilde{L}_2}$	$\frac{\nu_1^{e/i} \tilde{L}_\parallel}{\tilde{\rho}_s \tilde{\Omega}_e}$
a_b	$\left(\frac{2a_y}{\pi}\right)^{\frac{4}{5}} a_x^{\frac{1}{5}}$	$\left(\frac{2\tilde{a}_y}{\pi}\right)^{\frac{4}{5}} \tilde{a}_x^{\frac{1}{5}}$	\tilde{a}_b
a^*	$\left(2\rho_{s,1}^2 \rho_{s,2}^2 L_2^2 \frac{\Delta_x n_1}{n_{0,1}} \frac{R_0}{\rho_{s0}}\right)^{\frac{1}{5}}$	$\tilde{\rho}_{s,1} \left[\frac{2\tilde{L}_2^2}{\tilde{\rho}_{s,1} R_0} \frac{\Delta_x \tilde{n}_1}{\tilde{n}_{0,1}} \left(\frac{\tilde{\rho}_{s,2}}{\tilde{\rho}_{s,1}}\right)^2 \right]^{\frac{1}{5}}$	$\tilde{\rho}_s \left[\frac{\tilde{L}_\parallel^2}{\tilde{\rho}_s \tilde{R}} \right]^{\frac{1}{5}}$
ν^*	$\rho_{s,1} \left[8C(n_1) \rho_{s,1} \rho_{s,2} L_2 \frac{\rho_{s0}^2}{R_0^2} \right]^{\frac{1}{5}}$	$\tilde{c}_{s,1} \left(8C(n_1) \frac{\tilde{\rho}_{s,1} \tilde{\rho}_{s,2} \tilde{L}_2}{R_0^3} \right)^{\frac{1}{5}}$	$\tilde{c}_s \left(\frac{\tilde{\rho}_{s,1}^2 \tilde{L}_\parallel}{\tilde{R}^3} \right)^{\frac{1}{5}}$

Table 4.2 – Comparison of main blob parameters expression as derived here and as reported in the reference article [24]. Columns 1 and 2 contain the same expressions in GBS units and in physical units respectively. Myra’s expression in physical units are reported in the third column. In ν^* , $C(n) = (\delta n_1^5 / \Delta_x n_1^2 n_{0,1}^3) (\pi a_x / (2a_y))^2$.

$\nu^{e/i}$ appears. This relates to the parallel resistivity ν through the parallel conductivity $\sigma_\parallel = e^2 \tilde{n}_1 / (m_e \nu^{e/i})$,

$$\nu = \frac{R_0 m_e \nu^{e/i}}{m_i n_1 c_{s0}} = \frac{\nu^{e/i}}{n_1 \Omega_{0,e}} \frac{R_0}{\rho_{s0}} \quad (4.1.29)$$

with $\Omega_{0,e} = \Omega m_i / m_e$ electron gyro-frequency.

With respect to Myra *et al.* [24], herein we provide an explicit expression for a_b , a quantity that is otherwise usually interpreted as the radial (or poloidal) blob size \tilde{a}_x (or \tilde{a}_y) normalised over $\tilde{\rho}_{s,1}$. In addition, we retain $\Delta_x n_1 / n_{0,1}$ effects in a^* and ν^* as they account for the reduction of the curvature drive due to non zero background density.

Once again, if we set $\tilde{L}_1 = \tilde{L}_2$, $\tilde{n}_1 = \tilde{n}_2$, $\tilde{\rho}_{s,1} = \tilde{\rho}_{s,2}$ (i.e. $\tilde{T}_{e,1} = \tilde{T}_{e,2}$), $\Delta_x n_1 = \delta n_1 = n_{0,1} = 1$, and $a_x = k_y = 2a_y / \pi$ we retrieve the same expressions as the one derived in [24] in the large aspect ratio limit (up to some constant values).

Further progress can be done by observing that we can identify 4 main instabilities that drive the blob motion [24]. They correspond to different mechanisms that counter-balance the curvature drive in region 1 and they are: the sheath connected, denoted as C_s , and ideal interchange mode C_i regimes, typical in low collisionality ($\Lambda \ll 1$), and the Resistive Ballooning RB and Resistive X-point RX regimes, typical in high collisionality ($\Lambda \gg 1$). We focus here on the high collisionality case $\Lambda \gg 1$, where one can incur either in the RB, if $\Lambda \gg \Theta$, or in the RX regime, if $\Lambda \ll \Theta$. Since $\Lambda \gg 1$, then $\omega_\alpha \gg \omega_\sigma$, and the linearised vorticity equation in region 2 (see Eq. (4.1.19)) reduces to

$$\omega \simeq i\omega_{\sigma,2} \frac{\delta\phi_1}{\delta\phi_2} - i\omega_{\alpha,2} \quad (4.1.30)$$

Since $\omega_{\sigma,2}$ is small relatively to $\omega_{\alpha,2}$, either the parallel current term $i\omega_{\sigma,2} \delta\phi_1 / \delta\phi_2$ drops completely or, alternatively $\delta\phi_1 \gg \delta\phi_2$. In the first case the two regions are completely disconnected and the perturbation does not extend to region 2, therefore $\delta\phi_2 \sim 0$ and, in

region 1, the inertia balances the drive (RB regime), from Eq. (4.1.18):

$$\omega^2 \delta\phi_1 = -\gamma_{\text{mhd}}^2 \delta\phi_1, \quad \text{this leads to } \hat{\omega}_{\text{RB}} = i, \text{ and } \hat{\nu}_{\text{RB}} = \hat{a}^{\frac{1}{2}}. \quad (4.1.31)$$

On the other hand, if $\delta\phi_1 \gg \delta\phi_2$ (RX regime), in region 1

$$\omega^2 = -i\omega_{\sigma,1}\omega - \gamma_{\text{mhd}}^2 \quad (4.1.32)$$

i.e the parallel current balances the drive:

$$\hat{\omega}_{\text{RX}} = i \frac{\gamma_{\text{mhd}}}{\omega_{\sigma,1}} = i \frac{\Lambda}{\Theta}, \text{ and } \hat{\nu}_{\text{RX}} = \Lambda \hat{a}^{-2} \quad (4.1.33)$$

The transition threshold between the two regimes is at $\Theta = \Lambda$, as it can be observed in Eq. (4.1.32):

$$\hat{\omega}^2 + i \frac{\Theta}{\Lambda} \hat{\omega} + 1 = 0 \quad (4.1.34)$$

If $\Lambda > \Theta$ (RB regime) first and third term balance, alternatively, if $\Lambda < \Theta$ the second and the third term balance (RX regime), and the first term drops since $\hat{\omega}^2 = -\Theta/\Lambda \ll 1$. The same result for these two regimes can be obtained more formally, but less intuitively, by taking the limit of the dispersion relation in Eq. (4.1.22) for high values of Λ and obtaining directly the above Eq. (4.1.34).

Let us mention the relevant results in Ref. [24] concerning the low collisionality case. In the sheath connected C_s regime the curvature drive is balanced by the current flow to the sheath. In this case, $\omega = i\gamma_{\text{mhd}}^2/\omega_{\alpha,2}$, $\text{Im}(\hat{\omega}) = \Theta^{-1}$, and therefore $\hat{\nu} = \hat{a}^{-2}$. In the ideal interchange mode C_i regime instead the ion polarisation current (due to fanning of the flux surfaces) in region 2 balances the drive; the unstable frequency is $\omega = i\varepsilon_X \gamma_{\text{mhd}}$, which implies $\hat{\nu} = \varepsilon_X \hat{a}^{1/2}$. A practical way to visualise the four regimes and their transition threshold, introduced in Ref. [24], is reported in Fig. 4.3)

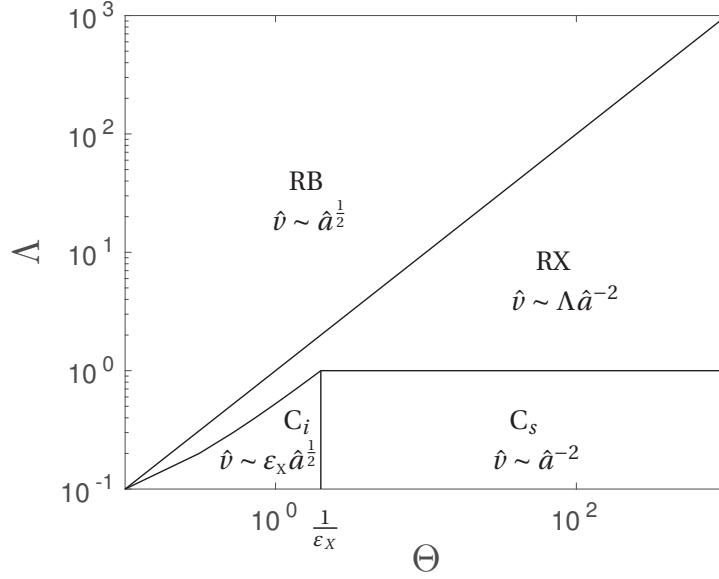


Figure 4.3 – Characterisation of blob regimes in the (Λ, Θ) plane and correspondent velocity to size scaling, as derived in [24] from the two region model.

To conclude, starting from a simplified version of the GBS vorticity and continuity equations, Eq. (4.1.1), and following the steps of [24], we have derived the expression of Λ , Θ , a_b , a^* , v , and v^* that determine the blob radial motion within the two region model, obtaining the velocity to size scaling of a blob in the various regimes at play in diverted configurations. Our expressions of the blob parameter show a few differences with respect to the ones obtained by Myra *et al.* [24]. In fact, the $\delta n/n$ effects are here retained both in the reference blob size a^* and in the reference velocity v^* . We keep the distinction between the length of the magnetic field line, L_1 and L_2 in the upstream and divertor regions. We express the resistivity Λ in terms of the normalised GBS resistivity ν and, finally, we define the blob size as $a_b = (2a_y/\pi)^{4/5} a_x^{1/5}$. These differences affect quantitatively the comparison of simulation and analytical results shown in Sec. 4.3.

4.2 Blob tracking in double-null GBS simulation

The scaling of the blob velocity provided by the two-region model is tested here against the results of a GBS simulation. The simulations are carried out with the version of GBS developed within the framework of the present thesis and consider a double-null configuration, with a poloidal flux based on that generated by three current-carrying wires and given by

$$\begin{aligned} \psi(\hat{r}, \theta) = & S(\log(\hat{r} - c) + \frac{1}{2} I \log((\hat{r} - c)^2 + 4 - 4(\hat{r} - c) \sin \theta) \\ & + \frac{1}{2} I \log((\hat{r} - c)^2 + 4 + 4(\hat{r} - c) \sin \theta)) \end{aligned} \quad (4.2.1)$$

with $S = 0.03$, $I = 10$, and $c = 0.9$. We remind that the radius \hat{r} is normalised to the tokamak minor radius a and the poloidal flux ψ is normalised to $(a^2|B_0|)$. Fig. 4.4 (left) presents a sketch of the flux surfaces in the GBS domain.

We note that in this configuration the magnetic field line length in the upstream region 1, L_1 , is approximately $2/3$ of the magnetic field line length from target to the midplane L_{\parallel} (in the proximity of the LCFS). This can be computed numerically as:

$$L_{\parallel} = \frac{1}{2} \int dl_{\parallel} = \frac{1}{2} \int \rho_* \frac{\sqrt{B_{pol}^2 + B_{tor}^2}}{B_{pol}} ds \quad (4.2.2)$$

where $B_{tor} = B_{\varphi} B^{\varphi} = 1$, $B_{pol} = B_{\theta} B^{\theta} + B_r B^r = \varepsilon \sqrt{(\partial_{\hat{r}} \psi)^2 + (\partial_{\theta} \psi / \hat{r})^2}$, with ε being the inverse aspect ratio, and the integral from the lower to the upper strike point is performed along a flux surface.

After an initial transient, the simulation reaches a quasi-steady state where a strong blob activity is present on the low-field side of the device, leading to transport of the plasma out-flowing from the tokamak core to the far SOL. A typical snapshot of this turbulent regime is shown in Fig. 4.4 (right). The present study is performed on a time window of 73 dimensionless time units during this quasi-steady state. The main physical parameters of interest are $\nu = 1$, $R_0/\rho_{s0} = 500$, and $a/\rho_{s0} \sim 127$.

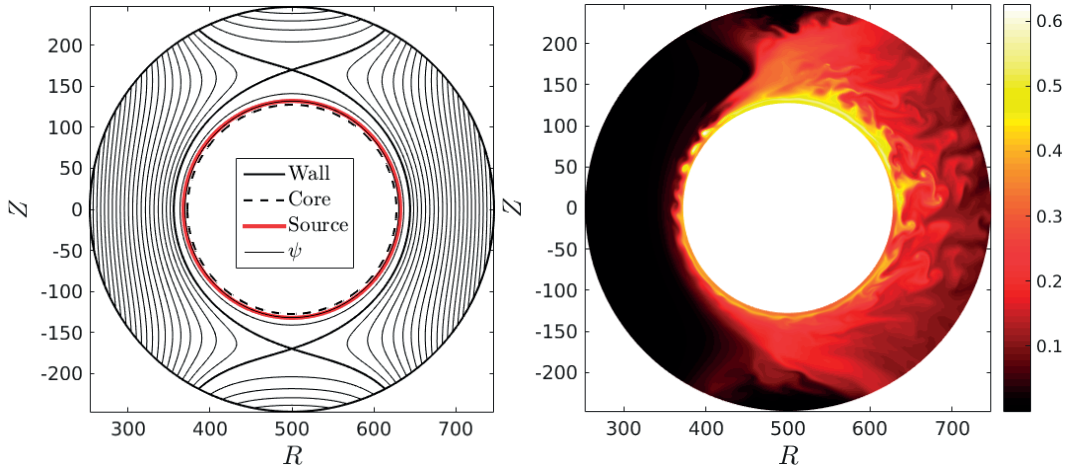


Figure 4.4 – Contour lines of the double null flux function in Eq. (4.2.1) used to run blob simulations (left) and typical snapshot of plasma density (right)

To detect blobs in the GBS simulation we use a pattern recognition algorithm similar to the one presented in Ref. [75]. We define as blob a structure of enhanced density (at least 2.5 times the fluctuation level) that moves coherently (i.e., it exists for $\Delta t > 0.2$). More precisely, blobs are detected from the simulation results as follows. We first identify the regions $\Omega_{b,high}$ with

density larger than the average density, n_{bg} , by 2.5 times the fluctuation level, σ_n , that is:

$$n(r, \theta, t) > n_{bg} + 2.5\sigma_n, \quad (4.2.3)$$

The average background density is computed by time and toroidally averaging the density during the quasi-steady state, $n_{bg}(r, \theta) = \langle n \rangle_{t, \varphi}$, and the standard deviation is defined as $\sigma_n(r, \theta) = \sqrt{\langle (n(r, \theta, \varphi_k, t_m) - n_{bg}(r, \theta))^2 \rangle_{t, \varphi}}$. Once the regions where Eq. (4.2.3) is satisfied are detected, a pattern recognition algorithm groups the points that are connected and therefore belong to and form the same blob. A blob is then tracked from one time frame to the next by checking whether there is (sufficient) spatial overlapping between $\Omega_{b, \text{high}}$ belonging to two subsequent time frames. Splitting and merging of blobs is also allowed by checking if 2 blobs end up corresponding to one single blob in the following time frame or vice-versa. The blob detection is carried out in one poloidal plane.

Having detected the blobs, we determine their size and velocity. The algorithm described above is efficient in tracking blobs, but it often underestimates the blob size, as it only detects the high density peak of a blob, indicated by the striped region in Fig. 4.2. In order to determine the blob size in a way consistent with the analytical two-region model, one needs to detect all the colored region in Fig. 4.2 that we will indicate with Ω_b , characterised by a density fluctuation above the half maximum, n_0 . To determine Ω_b , we take an area $\Omega_{b, \text{ext}}$ larger than $\Omega_{b, \text{high}}$ by $\sim 30\rho_{s0}$ in every direction, and re-define the blob as the set of connected (r, θ) points in $\Omega_{b, \text{ext}}$ for which:

$$n(r, \theta, t) > n_0 = n_{bg} + \delta n = n_{bg} + \max_{\Omega_{b, \text{high}}(t)} \frac{n - n_{bg}}{2}. \quad (4.2.4)$$

Note that the poloidal radius of Ω_b is the half-width half-maximum (HWHM) of the blob density perturbation, corresponding to a_y of the two-region model (see Fig. 4.2). The HWHM technique is commonly used in blob studies [71][76].

The blob detection algorithm also verifies the presence of sufficient overlapping in the subsequent time frames

$$\frac{||\Omega_b(t_m) \cap \Omega_b(t_{m+1})||}{||\Omega_b(t_m)||} > 0.8 \quad (4.2.5)$$

as well as

$$\left| \frac{||\Omega_b(t_m)|| - ||\Omega_b(t_{m+1})||}{||\Omega_b(t_m)||} \right| < 0.2 \quad (4.2.6)$$

to assess that the the blob size does not change very abruptly. If the blob domain Ω_b changes considerably from one time frame to the next, we consider them as two different blobs. The threshold coefficients 0.8 and 0.2 in the double null case are chosen so that the blobs have size and shape that are continuous enough, without incurring excessive splitting.

In order to compare the two-region model in Sec. 4.1 with the simulation results, we estimate

Chapter 4. Blobs

a_x , a_y , Λ , $\Theta = \hat{a}^{5/2} = (a_b/a^*)^{5/2}$, and $\hat{v} = v_x/v^*$ from the blob parameter in region 1. For this reason, we analyse only the blobs detected around the outboard midplane. Specifically, the blob center of mass can be at most $50\rho_{s0}$ away from midplane, $-50 < Z_{CM} < 50$, with the center of mass location (R_{CM}, Z_{CM}) defined as

$$R_{CM} = \frac{\langle R n(R, Z) \rangle_{\Omega_b}}{\langle n \rangle_{\Omega_b}}, \quad Z_{CM} = \frac{\langle Z n(R, Z) \rangle_{\Omega_b}}{\langle n \rangle_{\Omega_b}} \quad (4.2.7)$$

This also avoids counting the same blob twice, when the blob extends over the magnetic field by more than one toroidal turn. Note that x and y directions correspond to the radial and vertical directions, R and Z , when focusing on the outer midplane of an up-down symmetric equilibria (under the large inverse aspect ratio and large safety factor assumptions that allow us to approximate the plane perpendicular to \mathbf{b} with the poloidal plane). The blob radii $a_x = a_R$ and $a_y = a_Z$ correspond therefore to half of the extension of Ω_b along the R and Z directions. Note that actually for a_x we should take the half width of the total blob size, rather than the half width at the half maximum, but unfortunately we do not have a detection algorithm that captures the entire blob size above background density, as such algorithm would wrongly consider every fluctuation above background as a blob.

To limit the effect of numerical noise and uncertainty, a_Z and a_R are computed by averaging the top 10% of the ΔZ and ΔR values for each blob, where ΔR is the radial extension of the blob area at a given Z , and analogously for R .

We define $n_{0,1}$ as the minimum value of n in Ω_b , as suggested by figure 4.2, once again, to avoid numerical noise we average over the lowest 10% density values. To compute the density perturbation $\Delta_x n_1$ that we use to approximate $\partial_x n_1$, we look at the maximal blob density difference along R , for every fixed Z with $(R, Z) \in \Omega_b$, that we denote $\Delta n_b|_Z$ and we take the average of the top 10% values. Analogously, to compute δn_1 (in the equation of the reference velocity) we look at the maximal blob density difference along Z . Note that if the background density value is constant in the radial direction (across the blob domain) then $\delta n_1 = \Delta_x n_1$ and the two estimates coincide.

Another term frequently appearing in the blob parameter expressions is the Larmor radius $\rho_{s,1}$ which in GBS dimensionless units corresponds to $\sqrt{T_{e,1}}$ and that we compute similarly to $n_{0,1}$. The temperature in region 2 instead is not straightforward to compute since the magnetic field line can end at the wall on a different toroidal location than the one we are studying ($\varphi = 0$). For this reason we will consider here $\rho_{s,2} \sim \rho_{s,1}$.

The radial velocity $v_x = v_R$ (in c_{s0} units) is computed by tracking the radial center of mass location R_{CM} during a blob lifetime:

$$v_R(t_i) = \frac{R_{CM}(t_{i+1}) - R_{CM}(t_i)}{t_{i+1} - t_i} \rho_*^{-1} \quad (4.2.8)$$

where t_i is the snapshot time (within the present study $t_{i+1} - t_i = 0.05$).

Finally, we compute the parameters Λ , Θ (or \hat{a}), and \hat{v} , using the expressions in the first

column of table 4.2 and averaging over the blob lifetime.

Let us discuss some characteristics of the 248 blobs detected with the described algorithm. The average slow-down factor due to the background finite density is $\Delta_x n_1 / n_{0,1} \sim 0.7$. The average lifetime is 0.3, after which either the blob is lost or its size changes enough for it to be considered as a separate blob (according to the condition in Eq. (4.2.6)).

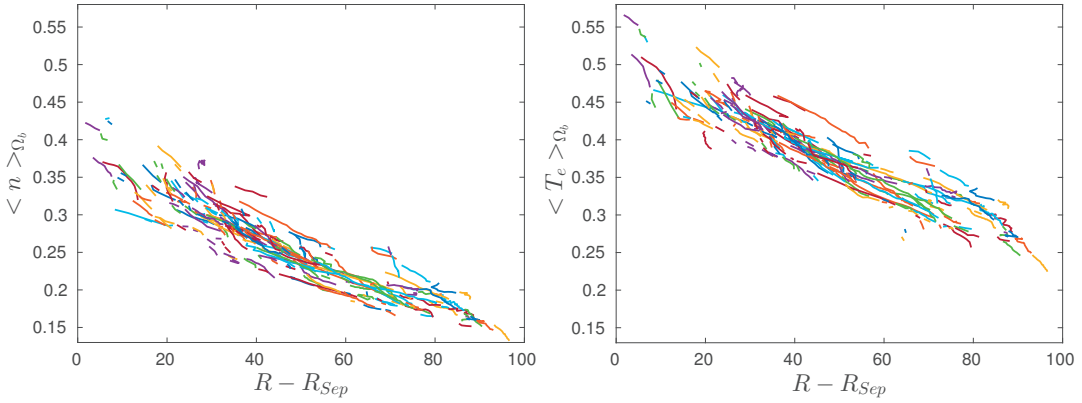


Figure 4.5 – Each line corresponds to a blob density (left) or temperature (right) time trace, plotted as a function of its distance to the separatrix in the major radius ($R - R_{Sep}$). $\langle n \rangle_{\Omega_b}$ ($\langle T_e \rangle_{\Omega_b}$) is the density (electron temperature) averaged on the blob poloidal cross section Ω_b . Both density and temperature decrease linearly as the blob travels radially outwards, at approximately the same rate.

Figure 4.5 (left) shows the decay of the blob density as it moves radially outwards. Each line corresponds to a blob, tracked over time. The density is computed as the averaged plasma density in the blob poloidal cross section Ω_b for the detected blobs. The reduction of the average density as the blob moves away from the separatrix is mostly the result of an increase of the blob size. While the integrated density across the blob area remains approximately constant, the blob area grows over the blob lifetime by approximately 132%, on average. This is due to 8.5% increase of a_Z (a_R remaining approximately constant) and to the general trend of a blob to go from a circular to a more square like shape, consistently with the picture of a resistive blob developing a mushroom like structure (see, e.g. Fig. 3 in Ref. [24]). If the blobs were attached to the sheath one would expect them to lose plasma to the wall. Figure 4.5 (right) shows a very similar behaviour reproduced also in the blob temperature. The total energy contained in a blob, $3/2 \int_{\Omega_b} n T_e$, also appears to decrease with the major radius, as shown in Fig. 4.6. Here we are plotting the average blob energy at a certain radial location, using 30 bins in the major radius. The gray shaded area represents the standard deviation from the mean in each bin. Large values of standard deviation are due to the variety of blob sizes in each bin, which obviously impacts the total energy.

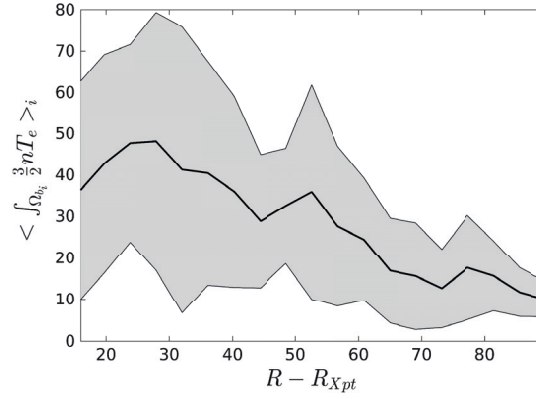


Figure 4.6 – Blob energy as a function of major radius. By grouping the blobs in bins according to their radial location, we compute the average energy contained in a blob for each bin (continuous black line). The gray shaded area indicates the standard deviation in each bin.

4.3 Comparison of the simulation results with the two-region model

Figure 4.7 locates the detected blobs in the (Θ, Λ) plane (left) and plots the normalised velocity \hat{v} of each blob as a function of its size \hat{a} (right). The detected blobs belong to the RB and RX regimes, with the threshold between the two regimes being at $\Theta/\Lambda = 1$. The analytical scalings of the two-region model for the blob velocity in the RB and RX regimes (black dashed lines) are shown to be the upper bounds of the measured blob velocity. We also plot the velocity scaling of the sheath connected C_s regime (red dashed line). This is similar to the RX regime, since the velocity is expected in both RX and C_s regimes be proportional to \hat{a}^{-2} , with the only difference being the multiplying factor $\Lambda \sim 10$. The simulation results show that the sheath connected scaling significantly underestimates the blob velocity, confirming that the large \hat{a} blobs belong to the RX regime. To our knowledge, it is the first time that blobs in RX regimes are observed and studied in blob simulations or experiments. The high collisionality causes the blob to partially disconnect from the sheath, as a consequence the blob sustains its self-induced electric field more efficiently, resulting in a faster outwards motion.

4.3. Comparison of the simulation results with the two-region model

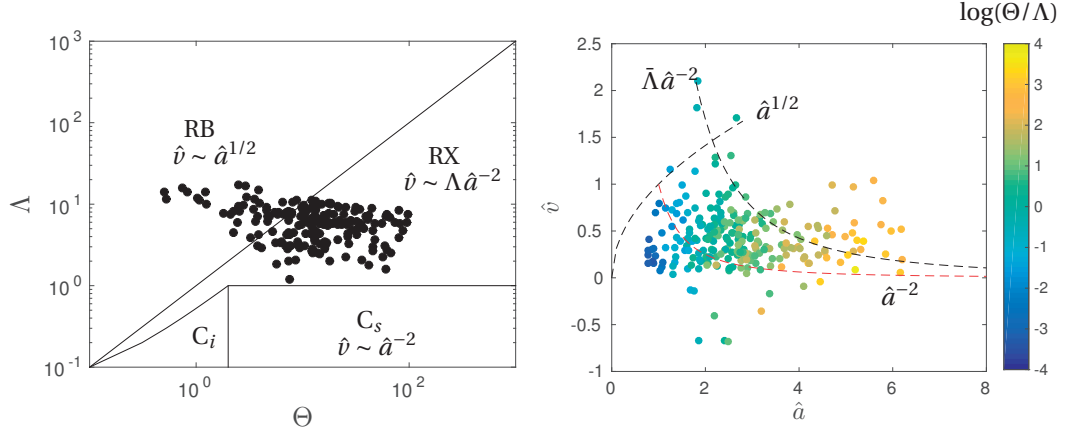


Figure 4.7 – Characterisation of blob regimes in (Θ, Λ) plane (left panel). The blobs belong to the resistive ballooning (RB) and resistive X (RX) regimes. The normalised blob velocity $\hat{v} = v_Z/v^*$ as a function of the normalised size $\hat{a} = a_b/a^*$ (right panel). Good agreement with the analytical scalings of RB and RX regime (in black dashed lines), and very different behaviour with respect to C_s sheath connected regime (in red dashed line) is shown. The color-scheme indicates $\log(\Theta/\Lambda)$, with the transition between the RB and the RX regimes being at $\Theta = \Lambda$.

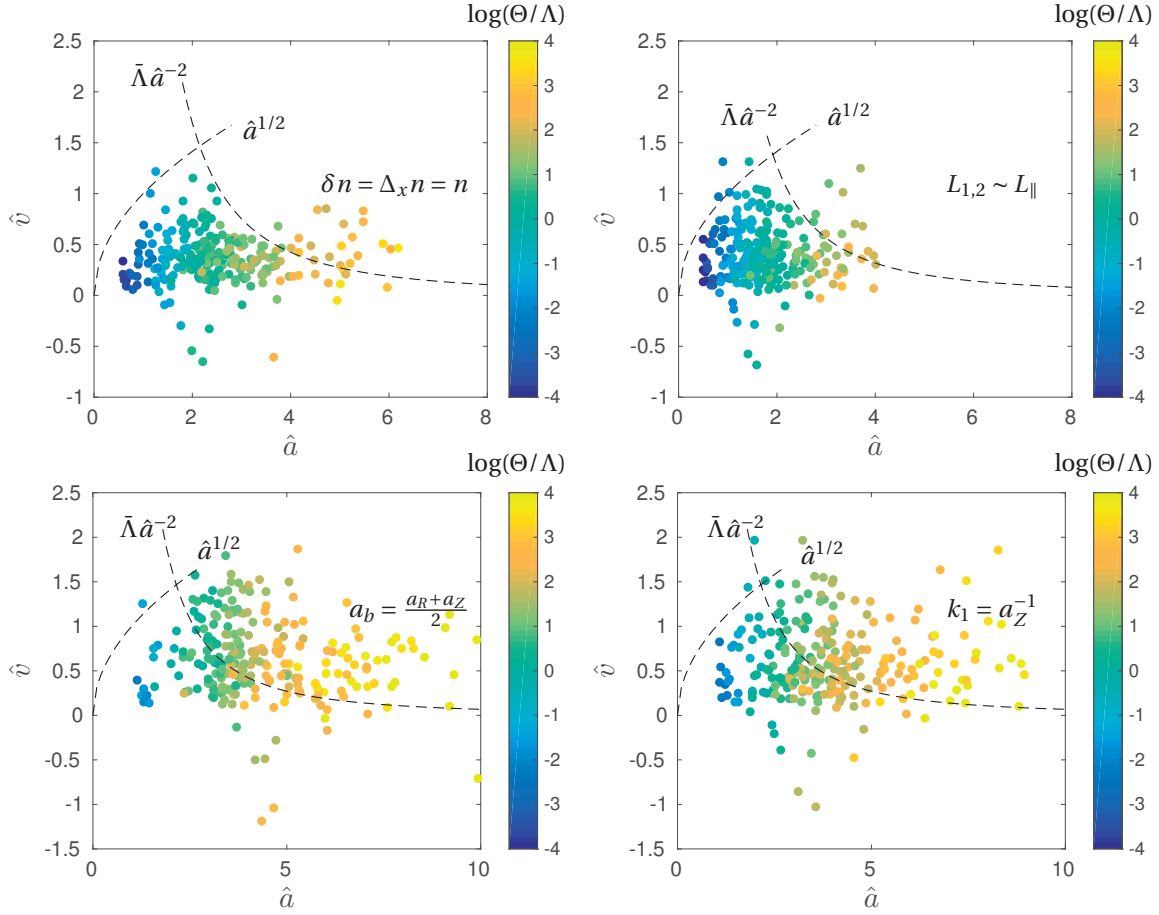


Figure 4.8 – Effect of various approximation of blob scaling. From left to right, top to bottom, impact of: excluding $\delta n/n$ effects, approximating magnetic field line length in region 1 with $L_{\parallel} = L_1 + L_2$, considering a_b to be the radial blob radius a_R or the vertical size a_Z . The qualitative behaviour is similar, but quantitatively the agreement with the analytical scaling is worse than in Fig. 4.7.

Our two-region scalings differ from the ones in Myra et al. [Ref.], as they retain $\delta n/n$ effect, possibly different values for the magnetic field lines in the upstream and divertor regions, as well as blob ellipticity. In Fig. 4.8, we test the influence of these effects on the velocity scaling. The top-left panel of Fig. 4.8 shows that removing the density perturbation effect shifts the blobs distribution to the left with respect to the analytical scaling since the normalised size \hat{a} is reduced by a factor $(\Delta_x n/n_0)^{2/5}$. At the same time, the normalised velocity is reduced by the increase of the reference velocity by a $(\delta n^5/\Delta_x n^3 n_0^2)^{1/5}$ factor. Considering the total magnetic field line length from target to midplane, L_{\parallel} , rather than the field line length in region 1, L_1 , (top-right panel of Fig. 4.8) reduces \hat{a} and impacts the value of Λ , resulting in a slightly worse agreement between the RB/RX regime transition, as indicated by the color code and as suggested by the velocity to size dependence. Finally, taking a_b to be the average between a_R and a_Z (bottom left panel of Fig. 4.8) significantly impacts the two-region prediction since

4.3. Comparison of the simulation results with the two-region model

most blobs are now estimated to belong to the RX regime, with the blobs distribution moving to the right, and the normalised size \hat{a} being overestimated. This is mainly due to the fact that we drop the $2/\pi$ term in a_b , introduced when relating the wavenumber k_1 to a_Z (i.e. $k_1 = 2a_Z/\pi$). This leads to an overestimate of the blob size, as shown in the bottom-right panel of Fig. 4.8.

We investigate further the difference between RB blobs and RX blobs by looking at the density, potential and parallel current of typical blobs belonging to the two regimes. Typically, RB blobs are localised closer to the separatrix and they do not extend to the divertor region. Furthermore, their parallel current is negligible. On the other hand RX blobs are localised further in the SOL and develop a parallel dynamic, reaching the wall. Nonetheless the associated potential perturbation is considerably small in region 2.

A typical blob contoured by a solid black line in the RX regime is shown in Fig. 4.9. As it can be seen from the top panels, the blob structure extends to the wall and reappears periodically in the poloidal plane, at the locations where the magnetic field line (identified by red circles) that passes through the center-of-mass of the detected blob comes back on the $\varphi = 0$ plane. The blob gets stretched as it approaches the X-points, because of the flux expansion present in these regions. The blob elongation along the magnetic field is also confirmed by the bottom panels that show the plasma density and parallel current on the flux surface of the center-of-mass of the blob in the (s, φ) plane, where s is the poloidal distance from midplane, along the magnetic flux surface of the blob, and φ is the toroidal angle (the square identifies the blob center-of-mass at $\varphi = 0$, which is also shown in the top panels). Note that the presence of the parallel current in region 1 and region 2 is not negligible. Furthermore, even though the structure can be traced up to the wall, the fluctuations in density and potential decrease moving from midplane to wall, indicating partial disconnection of the blob between the sheath and the midplane.

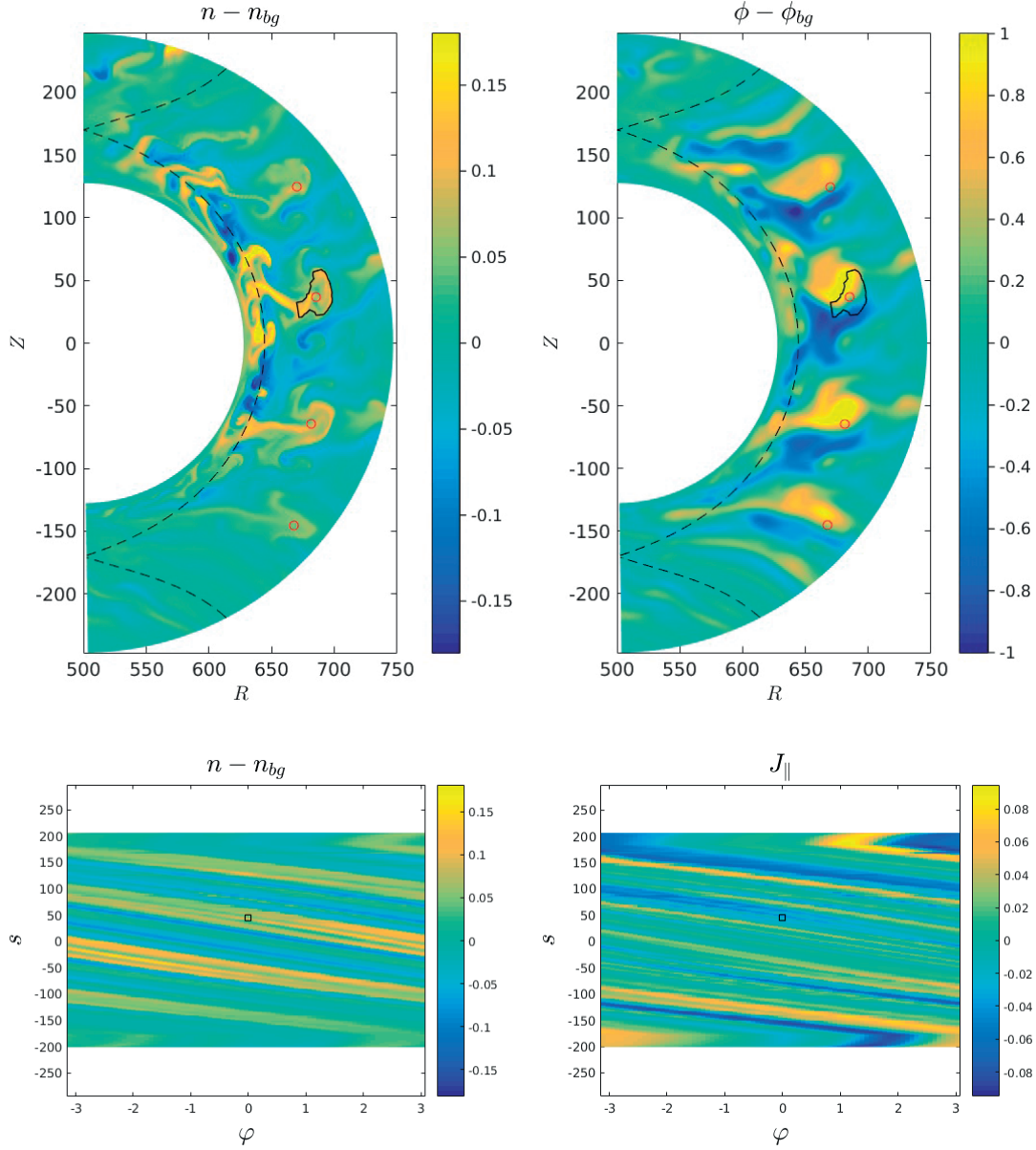


Figure 4.9 – A resistive-X (RX) blob. From left to right, top to bottom: density fluctuation $n - n_{bg}$ in (R, Z) , potential fluctuation $\phi - \phi_{bg}$ in (R, Z) (blob perimeter traced with continuous black line), density fluctuation along the flux surface, and parallel current $J_{\parallel} = n(v_{\parallel,i} - v_{\parallel,e})$ along the flux surface (square indicating blob center of mass location).

Fig. 4.10 shows the density poloidal snapshot of a RB blob. With respect to the RX blob, it is smaller in size and it is located just outside the separatrix. The electric potential shows the presence of a dipole, even though this extends outside of the blob perimeter (top right). Note that the blob structure does not reappear periodically on the poloidal plane this time. If we focus on the flux surface passing through the blob center of mass we can observe that the blob extends along the magnetic field line on the flux surface, without reaching region 2. Finally,

4.3. Comparison of the simulation results with the two-region model

the bottom right plot shows that the parallel current, $J_{\parallel} = n(v_{\parallel,i} - v_{\parallel,e})$, is almost negligible for a RB blob, in agreement with the model that predicts for a RB blob that the curvature drive is compensated by the perpendicular ion-polarisation current and with the parallel dynamics playing a minor role.

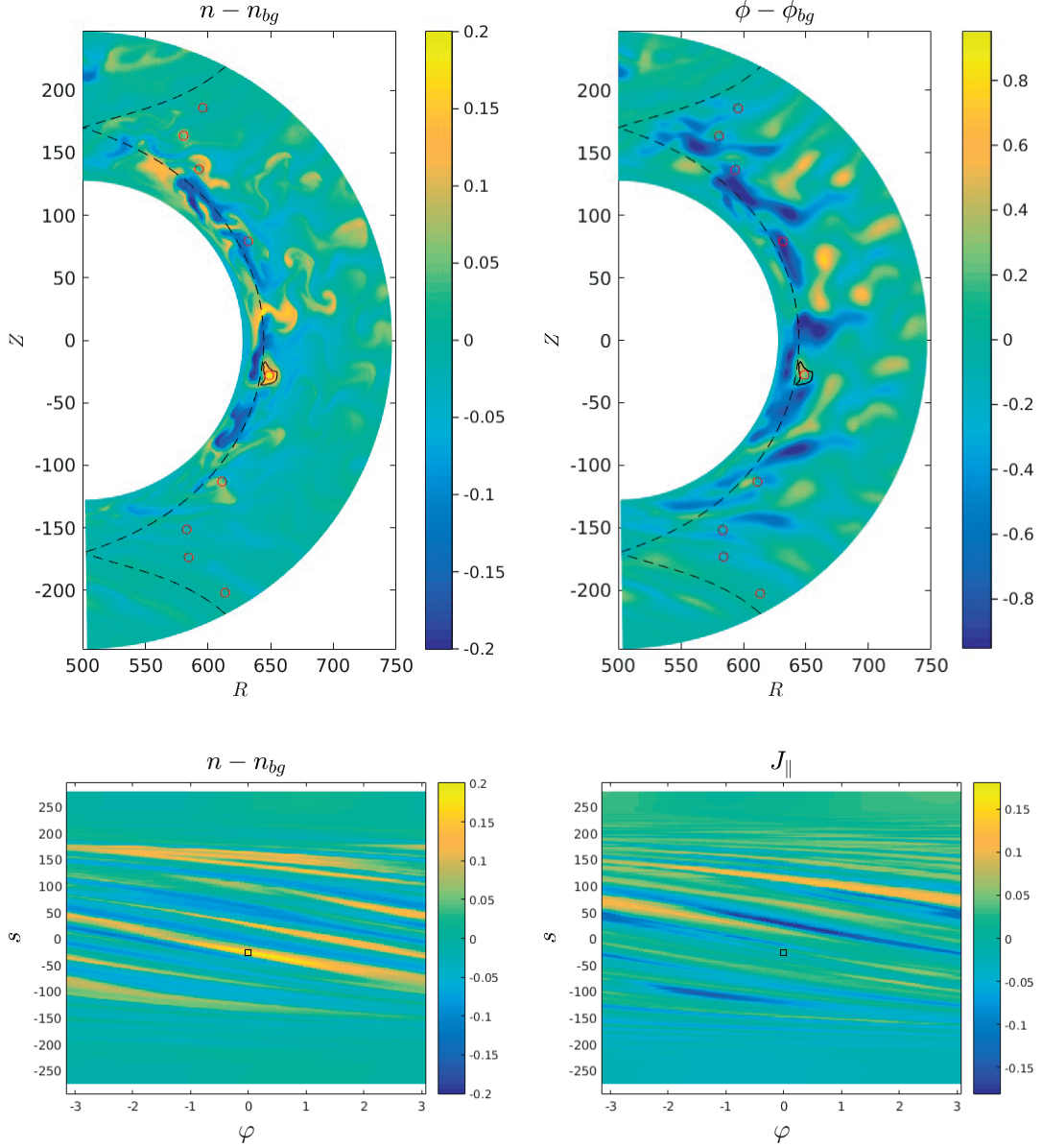


Figure 4.10 – An resistive ballooning RB blob. From left to right, top to bottom: density fluctuation $n - n_{bg}$ in (R, Z) , potential fluctuation $\phi - \phi_{bg}$ in (R, Z) (blob perimeter traced with continuous black line), density fluctuation along the flux surface, and parallel current $J_{\parallel} = n(v_{\parallel,i} - v_{\parallel,e})$ along the flux surface (square indicating blob center of mass location).

5 TCV-like simulation

To show the potential of the new version of the GBS code, we present here the results of a simulation that implements the magnetic geometry of TCV [77] discharge #49633. An L-mode lower single null plasma, with magnetic field at the axis $|B_0| = 1.4429\text{ T}$, safety factor $q \sim 3.6 - 4$, minor radius $a \sim 22\text{ cm}$, major radius $R_0 \sim 88\text{ cm}$, elongation $k \sim 1.4$ and triangularity $\delta \sim 0.1$ [78].

Since this is the first time a TCV diverted equilibrium has been simulated in GBS, we did not attempt to reproduce TCV plasma conditions or to perform a quantitative comparison with shot results. In particular, for computational reasons, we simulate here a machine roughly half the size of TCV by setting $\rho_*^{-1} = R_0/\rho_{s0} = 909.6$. This is an improvement with respect to the simple X-point and the double-null simulations presented in sections 3.7 and 4.2, for which $\rho_*^{-1} = 500$. This work presents a stepping stone for future quantitative comparisons with experimental results, as the simulation results presented here show good agreement with the general physical understanding of plasma turbulence in the periphery of a diverted tokamak.

This chapter is organised as follows. Section 5.1 is a guide to the implementation of the TCV diverted geometry in GBS and to the related challenges. Section 5.2.1 details the simulation setting, focusing on what differs from the general GBS setting presented in chapter 2. Of particular importance is the introduction of a friction term in the velocity equations, which prevent the source of plasma density and temperature from injecting parallel momentum. The simulation results are analysed in Sec. 5.3. In section 5.4 we underline the importance of further investigating the inner radial boundary conditions before quantitative comparison with experiments can be made.

5.1 Exporting a TCV magnetic equilibrium to GBS

The diverted configuration discussed in the previous chapters presented analytical expressions for the poloidal flux (see Eqs. (3.6.2) and (4.2.1)), symmetric around the $R = R_0$ vertical axis. This allowed an easier computation of the first and second ψ derivatives appearing in the differential operators (eqs (2.2.26)-(2.2.29)). The radial magnetic field at the wall changed sign only at a few regular intervals (in fact for both double null and simple X-point $B_r|_{\text{wall}} = 0$

at $\theta = k\pi/4$, $k = 0, \dots, 3$), simplifying the implementation of the boundary conditions and of the initial conditions. Moreover, a certain degree of symmetry in the magnetic equilibrium facilitated the post processing analysis. Finally, by choosing the innermost flux surface to be almost circular, the $\partial_r u = 0$ inner boundary condition (u indicating the evolved fluid quantities) roughly coincided with the more physical $\partial_\psi u = 0$ condition.

Using a TCV equilibrium requires us to deal with a ψ defined numerically on a Cartesian (R, Z) grid, on a domain whose boundaries do not coincide with the GBS ones (see Fig. 5.1). Hence, the function ψ , its first derivatives and its second derivatives in \hat{r} and θ need to be extrapolated to the GBS domain. In addition, ψ and its derivatives should be defined as continuous functions, otherwise the drift-reduced Braginskii's differential operators present discontinuities and as a consequence the evolved fields might do as well. From a physical point of view, a discontinuity in $\partial_{\hat{r}}\psi$ or $\partial_\theta\psi$ corresponds to a discontinuity of \mathbf{B} and a discontinuity in $\partial_{\hat{r}\hat{r}}\psi$, $\partial_{\hat{r}\theta}\psi$ or $\partial_{\theta\theta}\psi$ leads to discontinuous current.

We first extrapolate the flux function $\tilde{\psi}(R, Z)$ reconstructed by the equilibrium code LIUQE [79] (note that $\psi_{\text{LIUQE}} = 2\pi\tilde{\psi}$), on a wider rectangular (R, Z) domain that contains the circular GBS one. This is done with a MATLAB routine that uses plate deformation theory to perform smooth extrapolations [80]. The starting ψ_{LIUQE} has to be computed without wall currents to avoid discontinuities in the ψ derivatives when extrapolating across the wall. We numerically compute the first and second derivatives in R and Z , and we use them to evaluate the \hat{r}, θ derivatives on the (R, Z) grid, for example by using $\partial_{\hat{r}}\tilde{\psi} = \partial_R\tilde{\psi}\partial_{\hat{r}}R + \partial_Z\tilde{\psi}\partial_{\hat{r}}Z$. Finally, we interpolate the derivatives on the (\hat{r}, θ) grid of the GBS domain and normalise them to $a^2|B_0|$. With respect to the reference shot, the toroidal magnetic field direction is chosen such that the $\mathbf{B} \times \nabla B$ ion drift points away from the X-point, i.e. $B_0 > 0$, to avoid potentially entering into H-mode. Although simulating an H-mode scenario can be extremely interesting, the sharp gradients forming at pedestal require a smaller time step to grant the stability of the code, and therefore an increase in computational cost. Hence, as a first simulation, an L-mode is preferable. Furthermore, in H-mode scenarios, the drift-reduced approximation of the Braginskii's set of equations implemented in GBS loses its validity, since the perpendicular gradients at the pedestal are not lengths scales considerably larger than the sound Larmor radius ρ_s (see Sec. 2.1). Otherwise said, the physics length scales that are of interest in an H-mode scenario are that of the Larmor radius, implying that a gyrokinetic approach would be probably better suited for such configuration. Fig. 5.1 shows the contour plot of the poloidal flux ψ given by LIUQE inside the TCV vessel and its extrapolation to fill the GBS circular domain. Fig. 5.2 shows the color-plot of the ψ derivatives in the GBS domain. Note that the derivatives are continuous and their magnitude is of order 1, satisfying the assumption regarding typical scale lengths of ψ derivatives in sec 2.2.6 Eq. (2.2.15). Inverting the steps, i.e. interpolating first ψ on the (\hat{r}, θ) and then deriving it, produced discontinuous derivatives that can not be used.

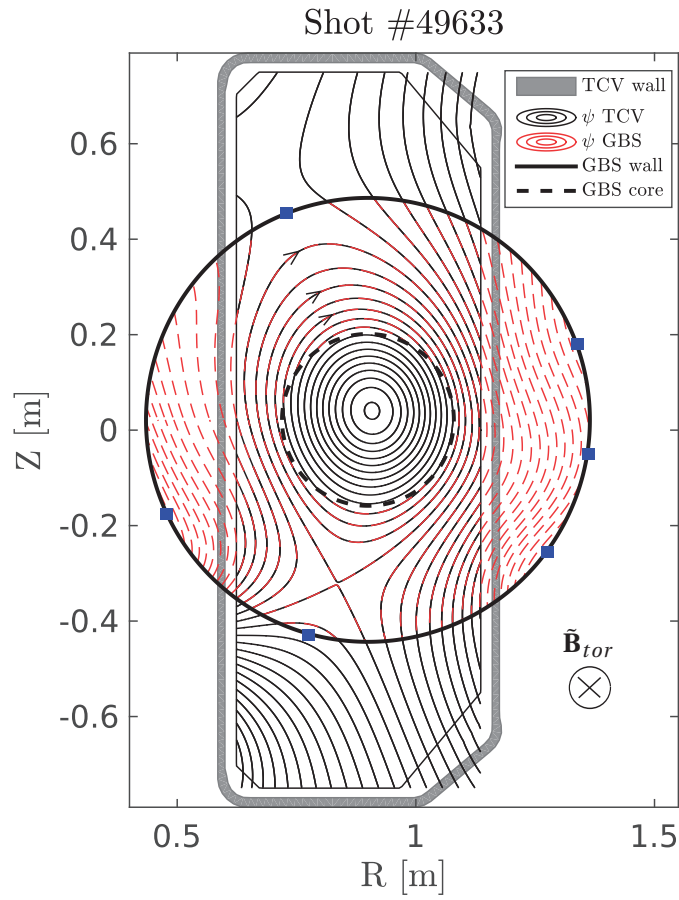


Figure 5.1 – Contour plot of TCV poloidal flux reproduced by LIUQE (black continuous line) in the TCV vessel and its extrapolation to the GBS domain (red staggered line). In blue the locations along the wall at which the radial magnetic field changes sign, that require special boundary treatment.

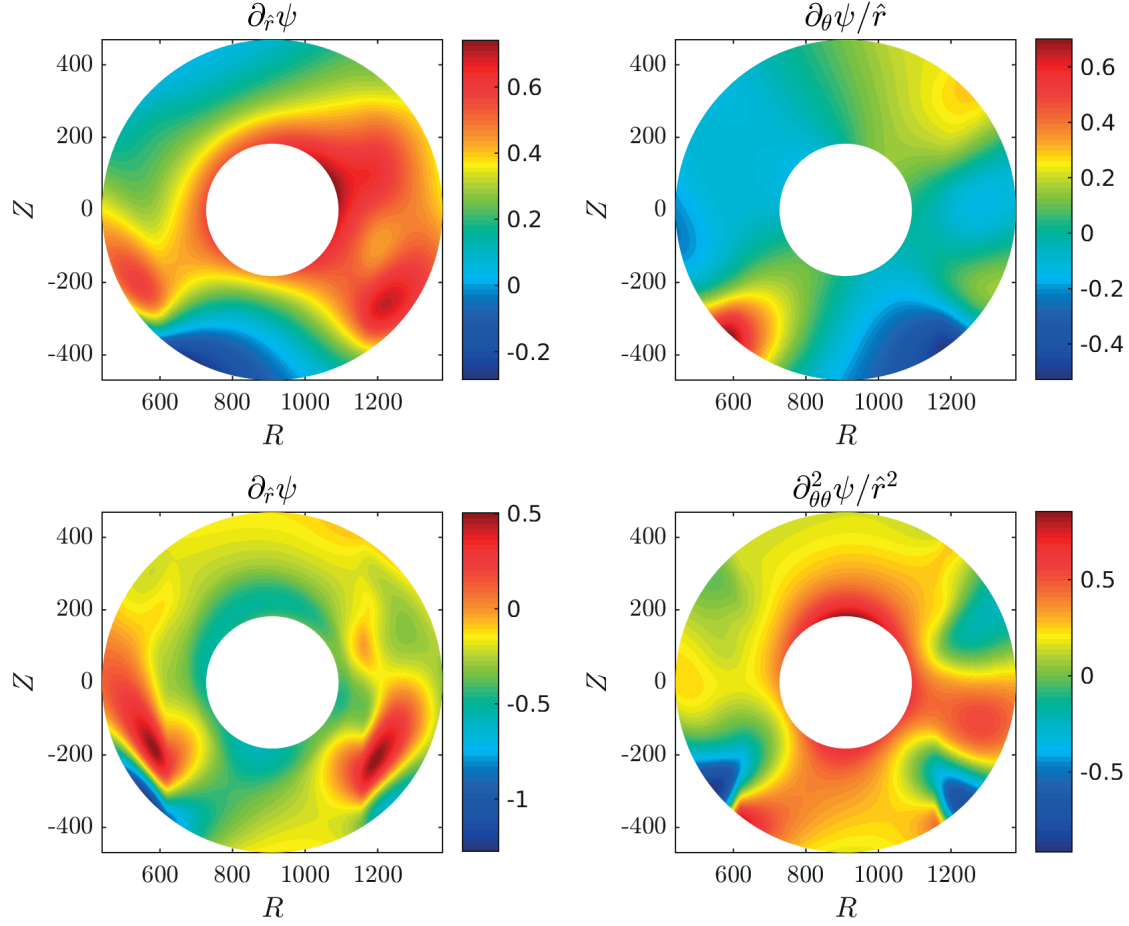


Figure 5.2 – Derivatives of ψ in Fig. 5.1 used to compute the differential operators on the GBS domain

5.2 Simulation settings

The simulation of TCV magnetic field is performed with a partly different setting that is an improvement of the one described in Chapter 2 and used for the simple X-point in Sec. 3.7 and the double-null in Sec. 4.2. The main differences are the wall boundary conditions for the smoothed areas, the location on the source on the flux surface rather than at $r = \text{const}$, the introduction of a friction term in the parallel momentum equations, and a different setting for the core boundaries. These two latter changes were implemented after observing unrealistically high parallel Mach numbers in the TCV simulation results (Sec. 5.2.4). The physical parameters are chosen to be closer to the experimental ones (Sec. 5.2.2).

5.2.1 Initial conditions and wall sources

The initial conditions are set to satisfy the boundary conditions presented in Sec. 2.3. In particular, the initial parallel velocities at the wall boundary have to be equal to the sound speed in norm, with the sign depending on whether the magnetic field line enters or exits the wall, i.e. $v_{\parallel e,i} = \pm \sqrt{T_e}$ for $T_e = \phi/\lambda = 1$, with \pm sign of $B_r|_{\text{wall}}$. It can be seen in Fig. 5.1 that B_r changes sign six times, i.e. B_r vanishes at the locations indicated by blue squares. Figure 5.3 (left) shows the initial condition for electron and ion velocities. In the vicinity of the $B_r = 0$ locations, smoothing is applied to transition from $+\sqrt{T_e}$ to $-\sqrt{T_e}$ with no discontinuities.

In Fig. 5.3 (right), the initial condition for plasma density and electron temperature are shown through the electron pressure. These conditions are chosen so that density and temperature have higher values in the closed flux surface region and lower ones in the SOL, with the transition being at the closed flux surface where the source is located. In the simple X-point and double null case the initial density and pressure were constant on the whole domain and the source was located at $r = \text{const}$ rather than at $\psi = \text{const}$.

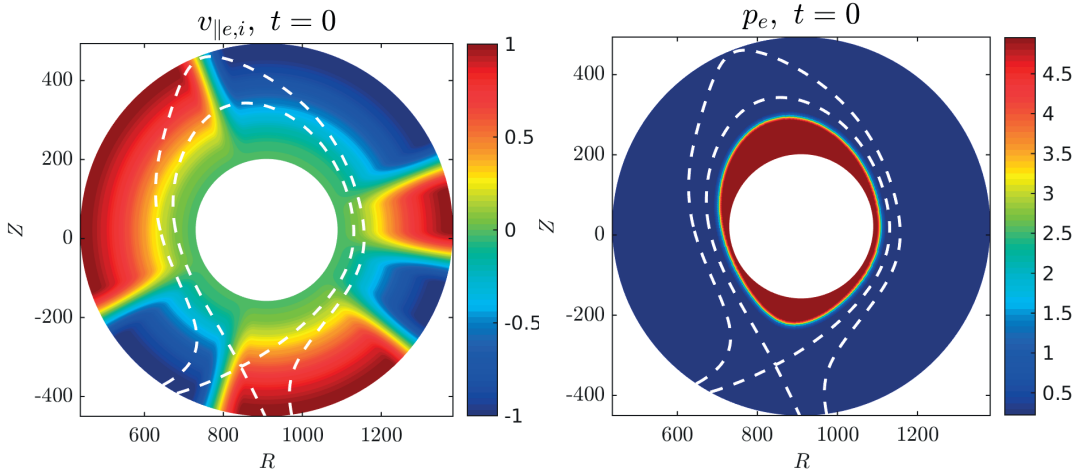


Figure 5.3 – Initial conditions for density temperature and velocity.

Sources of plasma at the wall were introduced in these simulations to avoid excessive decrease in density in the far SOL, which would cause numerical instabilities, due to $1/n$ terms appearing in equations and boundary conditions. Additionally, the physical model itself is not valid in the absence of plasma.

5.2.2 Physical parameters

The simulation considers the following parameters: $\rho_\star^{-1} = 909.6$, inverse aspect ratio $a/R_0 \sim r_{\min}/R_0 = 0.2$, parallel resistivity $\nu = 0.3$, and $\tau = 0$ (cold ion limit). In order to improve the physical model, we introduce the dependence on plasma density and electron temperature of the parallel heat conductivity χ_\parallel and parallel viscosity $\eta_{e,i}$, that were considered as constant

parameters in the previous studies presented in this thesis.

$$\eta_e = \eta_{e,p} \frac{T_e^{5/2}}{n} + \eta_{e,0} \quad (5.2.1)$$

$$\eta_i = \eta_{i,p} \frac{1}{n} + \eta_{i,0} \quad (5.2.2)$$

$$\chi_{\parallel} = \chi_{\parallel,T} T_e^{5/2} + \chi_{\parallel,0} \quad (5.2.3)$$

Here $\chi_{\parallel,0} = 4$, $\eta_{e,p} = 2 \times 10^{-3}$, $\eta_{i,p} = 2 \times 10^{-2}$, $\eta_{e,0} = 0.4$, $\chi_{\parallel,T} = 1.4 \times 10^{-2}$, $\chi_{\parallel,0} = 4.7$.

5.2.3 Revised wall boundary conditions

In the magnetic pre-sheath model, the plasma accelerates towards the wall at the sound speed, meaning that the ion velocity increases its absolute value going towards the wall $\partial_r |v_{\parallel i}| > 0$. The radial derivative of $v_{\parallel i}$ and its sign are of crucial importance for the wall boundary conditions implemented in GBS (see Eqs. (2.3.1)). The wall behaves as a sink of plasma only if $\partial_r |v_{\parallel i}| > 0$, as $\partial_r n \propto -\partial_r |v_{\parallel i}|$. Therefore, a change of sign in the radial derivative can lead to nonphysical flow of plasma from the wall to the SOL. Similarly the derivative of the electric potential should be negative, $\partial_r \phi \propto -\partial_r |v_{\parallel i}|$, in agreement with the presence of an electron sheath at the wall.

When approaching the $B_r = 0$ locations, the smoothing (see Sec. 2.3) forces $v_{\parallel i}$ to deviate from c_s and tend towards 0, as illustrated in Fig. 5.3 left. This leads to $\partial_r |v_{\parallel i}| < 0$ and to the development of numerical instabilities especially at the top smoothing region, where the turbulent SOL plasma approaches the wall with net parallel velocity that can be greater than boundary value.

A revised set of boundary conditions for the smoothed areas shows good numerical stability. The extrapolation of $v_{\parallel,i,e}$ boundary values is left unchanged, but we use $\partial_r v_{\parallel,i} = 0$ and $\partial_{rr}^2 v_{\parallel,i} = 0$ at the RHS of the magnetic pre-sheath boundary conditions in Eqs. (2.3.1), such that $\partial_r \phi = 0$, $\partial_r n = 0$, $\omega = 0$, $\partial_r T_{e,i} = 0$. In the rest of the domain the boundary conditions are mostly unchanged, except for a limitation of derivative of n to zero, to prevent the plasma from flowing radially in from the wall. When this happens, the plasma can still be advected to the wall by the parallel velocity.

From a physical point of view, the magnetic pre-sheath boundary conditions describe the behaviour of the background equilibrium field rather than the one of the fluctuating quantities [31] (in the derivation of the boundary conditions, $\partial_t u$ terms are set to zero). In future, a more robust and consistent way of applying the boundary conditions in the non smoothed regions could be obtained using the radial derivative of the time averaged $v_{\parallel,i}$.

5.2.4 Source of parallel momentum and inner radial boundary conditions

The simulation setting presented in the above sections 5.1-5.2.3 was used to run a TCV-like simulation, with grid $N_r \times N_\theta \times N_\varphi = 216 \times 732 \times 88$, and time step $\Delta t = 10^{-5}$. Fig. 5.4 shows the field values averaged on the 3D domain as a function of time. Focusing on the ion velocity

$v_{\parallel i}$ profile, we notice that its average value increases by 50% from $t \sim 10$ to $t \sim 20$ and then it stabilises between $t \sim 31$ and $t \sim 42$. The average of ω , $v_{\parallel e}$, ϕ fluctuate around constant values, i.e. are at quasi-steady state, from time $t = 20$ onward. Density and electron temperature display variations that are less than 1% for the temperature and 5% for the density in the gray region. The simulation took two/three weeks to run (0.1 GBS time units per hour), it was parallelised on 44 nodes, with 36 tasks per node (i.e. 1584 CPUs), at the Swiss National Supercomputing Center in Lugano, Switzerland supercomputer.

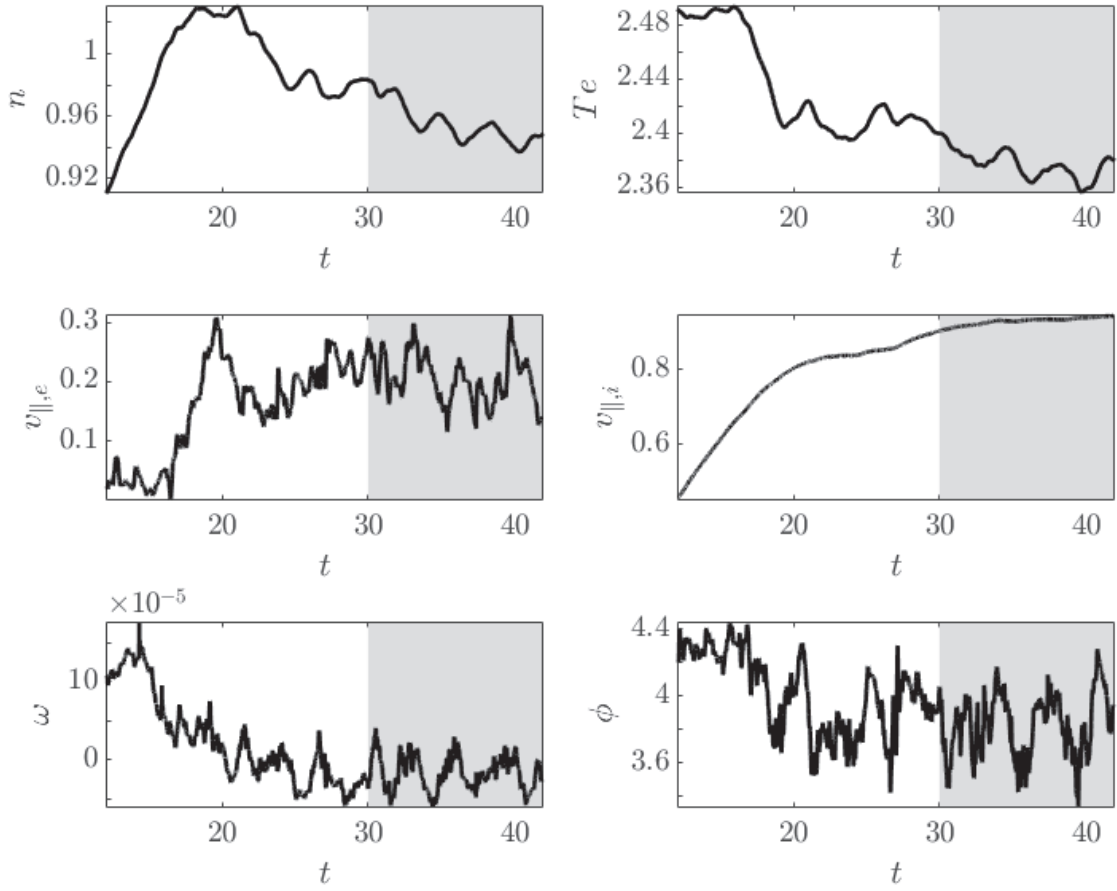


Figure 5.4 – Time trace of the evolved quantities averaged over the 3D domain. The grey region exhibits steady state behaviour, with fields fluctuating around roughly constant values.

The simulation results in the steady state region were analysed and most of the quantities behaved as expected, except for the parallel ion velocity. Figure 5.5 shows a temporal snapshot (left) and the time and toroidally averaged profile (right) of $v_{\parallel i}$. The fact that $v_{\parallel i}$ is positive in the entire closed flux region indicates that the plasma is rotating in the toroidal direction. Since $v_{\parallel i}$ is normalised to the reference ion sound speed $c_{s0} = \sqrt{T_{e0}/m_i}$, values above unity in the background profile as the ones in Fig. 5.5 (right) appear to be nonphysical.

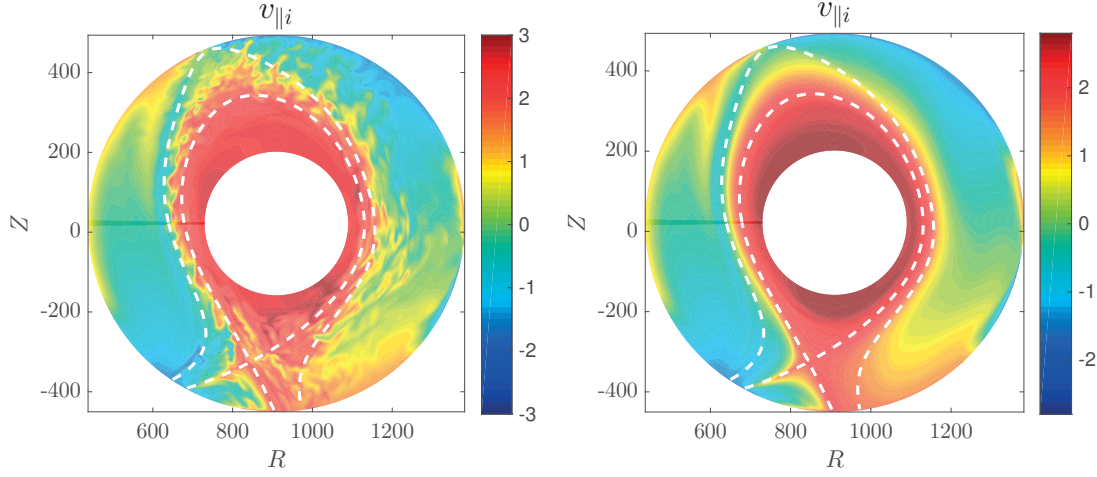


Figure 5.5 – Parallel ion velocity poloidal snapshot (left) and time and toroidally averaged profile (right).

The Mach number $M = \tilde{v}_{\parallel,i} / \tilde{c}_s$, computed using the local ion sound speed $\tilde{c}_s = \sqrt{\tilde{T}_e / m_i}$, was used to test the physicality of the parallel ion velocity. Since in experiments without injection of parallel momentum Mach numbers in the closed flux region are usually ~ 0.1 and not above 0.4 (see [81]), parallel Mach number above 1 in the edge of tokamak devices are not realistic. The parallel Mach number computed from the dimensionless GBS quantities is

$$M = \frac{\tilde{v}_{\parallel,i}}{\tilde{c}_s} = \frac{v_{\parallel,i} \sqrt{T_{e0} / m_i}}{\sqrt{\tilde{T}_e / m_i}} = \frac{v_{\parallel,i}}{\sqrt{T_e}} = \frac{v_{\parallel,i}}{c_s} \quad (5.2.4)$$

Figure 5.6 (left) shows the time and toroidally averaged parallel M displaying nonphysical values around 1 in the SOL and above 1 in the edge. This can also have negative repercussions on the boundary physics, in fact, as discussed in Sec. 2.3, if the absolute value of the parallel velocity does not increase towards the wall, the magnetic pre-sheath boundary conditions fail. For this reason, and in order to avoid numerical instabilities, in this simulation the boundary conditions for the parallel ion velocity (in the regions without smoothing) were adjusted to be $|v_{\parallel,i}(r_{\max})| = \max(c_s(r_{\max}), |v_{\parallel,i}(r_{\max} - \Delta r)|)$, with Δr radial grid spacing, such that the $\partial_r |v_{\parallel,i}| \geq 0$, always.

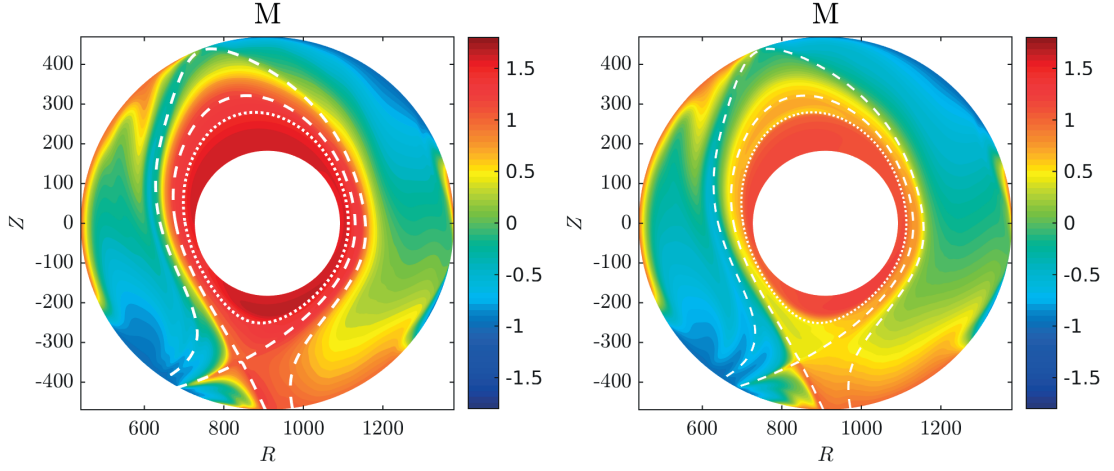


Figure 5.6 – Parallel Mach number $M = v_{\parallel,i}/c_s$ showing unrealistically high values $M > 1$ in the near SOL and EDGE for the standard case (left), and values of $M \sim 0.5$ when introducing a friction source term in the parallel direction and lowering the inner boundary value for $v_{\parallel,i}$ (right).

The Mach number takes its maximum value at the bottom close to the source location (see Fig. 5.6 (left)), suggesting there could injection of parallel momentum there. In order to mimic the outflow of plasma from the core, the drift-reduced Braginskii's equations implemented in GBS introduce a source term solely in the density and temperature equations. A friction term in the parallel electron and ion equations should be introduced to account for the fact that the density is injected with zero velocity. In this simulation, since the friction term is missing, the plasma density source assumes the local velocity, resulting in a net injection of momentum. This would be the equivalent of an NBI beam injecting plasma at the local parallel velocity. Specifically, if the continuity equation has a source term S_n

$$\frac{dn}{dt} = \frac{\partial \tilde{n}}{\partial \tilde{t}} + \nabla \cdot (\tilde{n} \tilde{\mathbf{v}}_s) = \tilde{S}_n \quad (5.2.5)$$

with \mathbf{v}_s fluid velocity of the s species, then the corresponding term in the momentum equation is:

$$m_s \tilde{n} \frac{d\tilde{\mathbf{v}}_s}{d\tilde{t}} = \sum \tilde{\mathbf{F}} - m_s \tilde{S}_n \tilde{\mathbf{v}}_s \quad (5.2.6)$$

This results from substituting the density equation into the momentum equation to remove $\partial_t n$, $m_s \partial_t (\tilde{n} \tilde{\mathbf{v}}_s) = m_s \tilde{\mathbf{v}}_s \partial_t \tilde{n} + m_s n \partial_t \tilde{\mathbf{v}}_s$. For the dimensionless parallel equations in drift-reduced Braginskii's model (2.1.12)-(2.1.13), the term becomes $-v_{\parallel,i,e} S_n/n$. The injection of momentum linked to the perpendicular drift velocities is not investigated in the framework of this thesis.

Another factor that could contribute to the high values of parallel velocity is the inner radial

boundary condition. As mentioned in Sec. 2.3, the region between the inner radial boundary and the source location is of no physical interest, and the presence of the source should help to decouple the dynamics of this region from those at the edge. As previously shown, the boundary conditions at the inner wall are of the type $\partial_r u = 0$ for all fields except the electric potential for which a Dirichlet boundary condition is required. In the case of TCV simulations, there is a drop in electric potential across the separatrix, with ϕ going from positive in the SOL to negative in the edge. This is not compatible with the $\phi = \lambda T_e > 0$ inner boundary condition, used for previous simulations. For this reason the inner boundary of ϕ is set to 0. Furthermore, to help the field values in the inner region stay in a range not too far from the edge values, we bound the evolved quantities at the core:

$$u(r_{\min}) = \max(u_{\min}, \min(u_{\max}, u(r_{\min} + \Delta r))) \quad (5.2.7)$$

where $u(r_{\min}) = u(r_{\min} + \Delta r)$ would correspond to $\partial_r u = 0$. In the current simulation, $v_{\parallel,i}$ background velocity reaches the maximum imposed value $v_{\parallel,i,\max} = 2.8$ over most of the inner boundary (Fig. 5.5 right panel).

With the aim to reduce the toroidal rotation, the friction source term in the ion and electron velocities is introduced and the $v_{\parallel,i,\max}$ inner boundary value is lowered from 2.8 to 2. The simulation again reaches a quasi-steady state starting from $t \sim 70$ (see Fig. 5.7). Fig. 5.6 (right) shows that the average Mach number has significantly decreased towards more realistic values in the in the edge and SOL.

5.3 Preliminary results

The results from the TCV simulation with source of parallel momentum and $v_{\parallel,i,\max} = 2$ at the core are presented in this section. The quasi-steady state time interval between $t = 70$ and $t = 87$ is indicated by the shaded grey area in Fig. 5.4, where the field values averaged on the 3D domain are plotted in time. All fields show a clear steady state behaviour in the grey region, except for the density, although its overall variation is $\sim 5\%$.

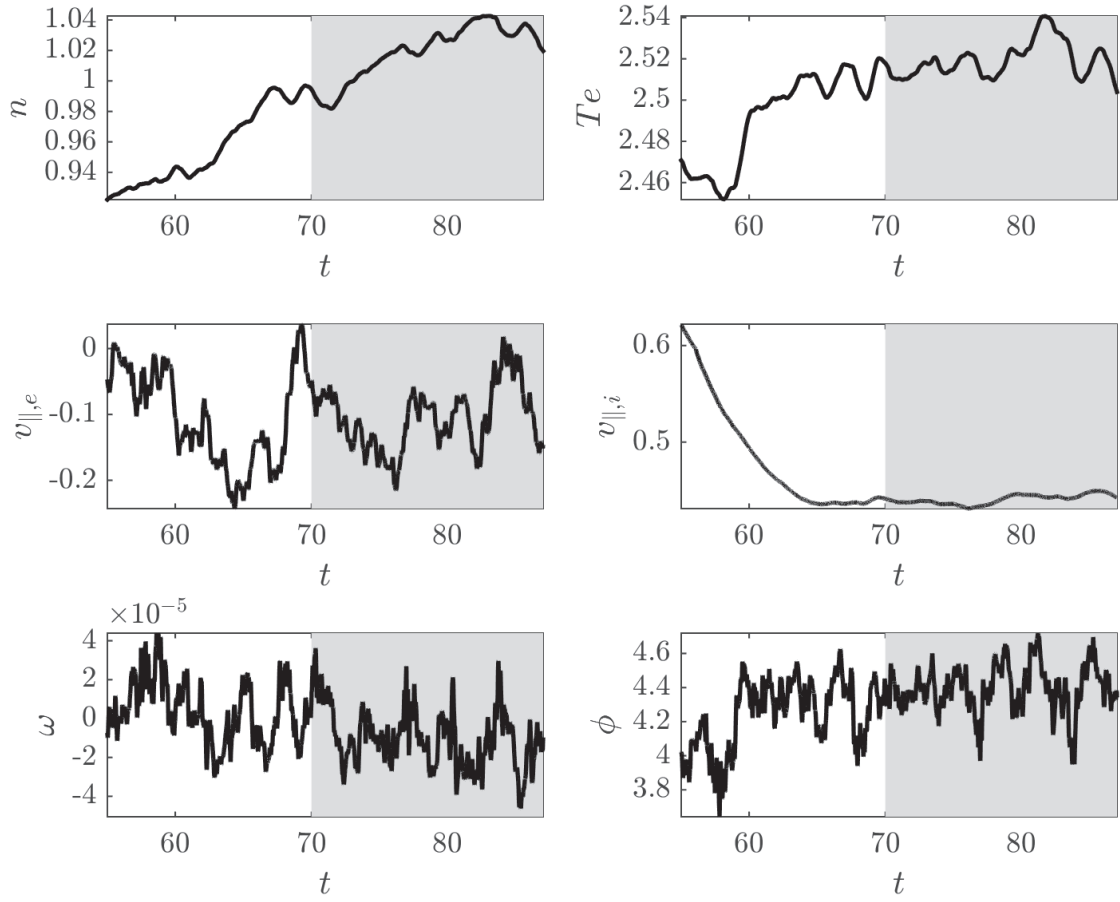


Figure 5.7 – Time trace of the evolved quantities averaged over the 3D domain. The gray region exhibits steady state behaviour, with fields fluctuating around roughly constant values.

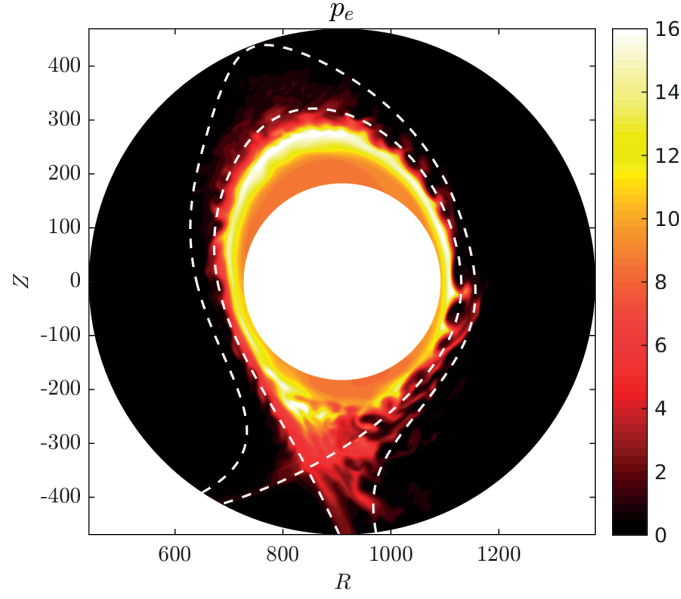


Figure 5.8 – Poloidal cut of the electron pressure ($p_e = nT_e$) in GBS simulation of TCV-like scenario. The dashed lines trace the separatrix and the last connected flux surface.

Fig. 5.8 shows a snapshot of the electron pressure $p_e = nT_e$ turbulence at $t = 73.98$. The electron pressure is mostly confined in the closed flux surface region and peaks at the source location. The up down asymmetry of p_e could be due to the flux expansion around the X-point, that maps the turbulent modes forming at the edge of the LFS into radially wider structures above the X-point. The unstable modes in the closed flux surface region are sheared at the separatrix and form blobs, especially at the LFS, in agreement with our physical understanding of blob formation (see introduction to chapter 4). Furthermore, close to the outer divertor legs, the blobs are elongated because of the flux expansion around the X-point, in accordance with to the two-region model underlying mechanism (see Fig. 4.1). The innermost white dashed line tracks the separatrix, while the outer one is the last flux surface that connects the LFS to the HFS. When the plasma crosses this second flux surface, it experiences an abrupt drop in the parallel connection length L_{\parallel} , which plays a key role in determining the blob dynamics (see chapter 4). In particular, a reduction in L_{\parallel} facilitates the connection to the sheath and the current closure in the parallel direction, possibly explaining the drop in electron pressure beyond the last connected flux surface.

Typical turbulent snapshots for all fields are shown in Fig. 5.9 at time $t = 76.67$. In subplot (a) the turbulent fluctuations of $\log(n)$ are lower at the HFS than at the LFS, consistently with the ballooning character of turbulence. The density peaks at the source location, which is traced by the dotted line. The increase of density towards the inboard wall is due to the presence of the localised wall sources, discussed in Sec. 5.2.1. The top part of the circular wall acts as a limiter for the plasma exiting the last connected flux surface. The temperature shows a similar HFS/LFS asymmetric behaviour, although its radial profile appears to decay on longer scale lengths (see subplot (b)). The electron parallel velocity (c) is positive at the

outer leg and negative at the inner leg, in agreement with the boundary conditions, and it presents elongated structures matching the elongated blob shapes. The X-point topology is here more clearly visible. Furthermore, $v_{\parallel e}$ present sharp fluctuations above background reaching values of $\pm 12c_{s0}$, and dropping to zero over only 3 or 4 ρ_{s0} . Both electron (c) and ion velocities (d) are positive in the closed field line region, with plasma rotating toroidally. The electric potential (e) goes from positive in the SOL to negative inside the separatrix, causing the plasma to rotate poloidally. This drop of electric potential was incompatible with the boundary condition initially set for the core $\phi = \lambda T_e$ and is the reason why the inner boundary is now set to $\phi = 0$ (see Sec. 5.2.4). Finally, the fluctuation levels in the vorticity plot (f) helps locating the turbulent region, consisting mainly in the edge and SOL.

In Fig.5.10 the time and toroidally averaged profiles of the fields are presented. The peak of the density and temperature is localised around the flux surface where the source is located ψ_{src} . The average $v_{\parallel e}$, ϕ , and ω highlight the magnetic field topology, especially the last closed flux surface and the last connected flux surface. The vorticity in particular takes its highest and lowest values just around the separatrix. Knowing the exact relation between ϕ profile and separatrix could help reduce the uncertainty on the separatrix location in experiments. In figure 5.10 (f) the electric potential appears to cross the zero value around the separatrix at the LFS, but a more precise estimate still requires further investigation.

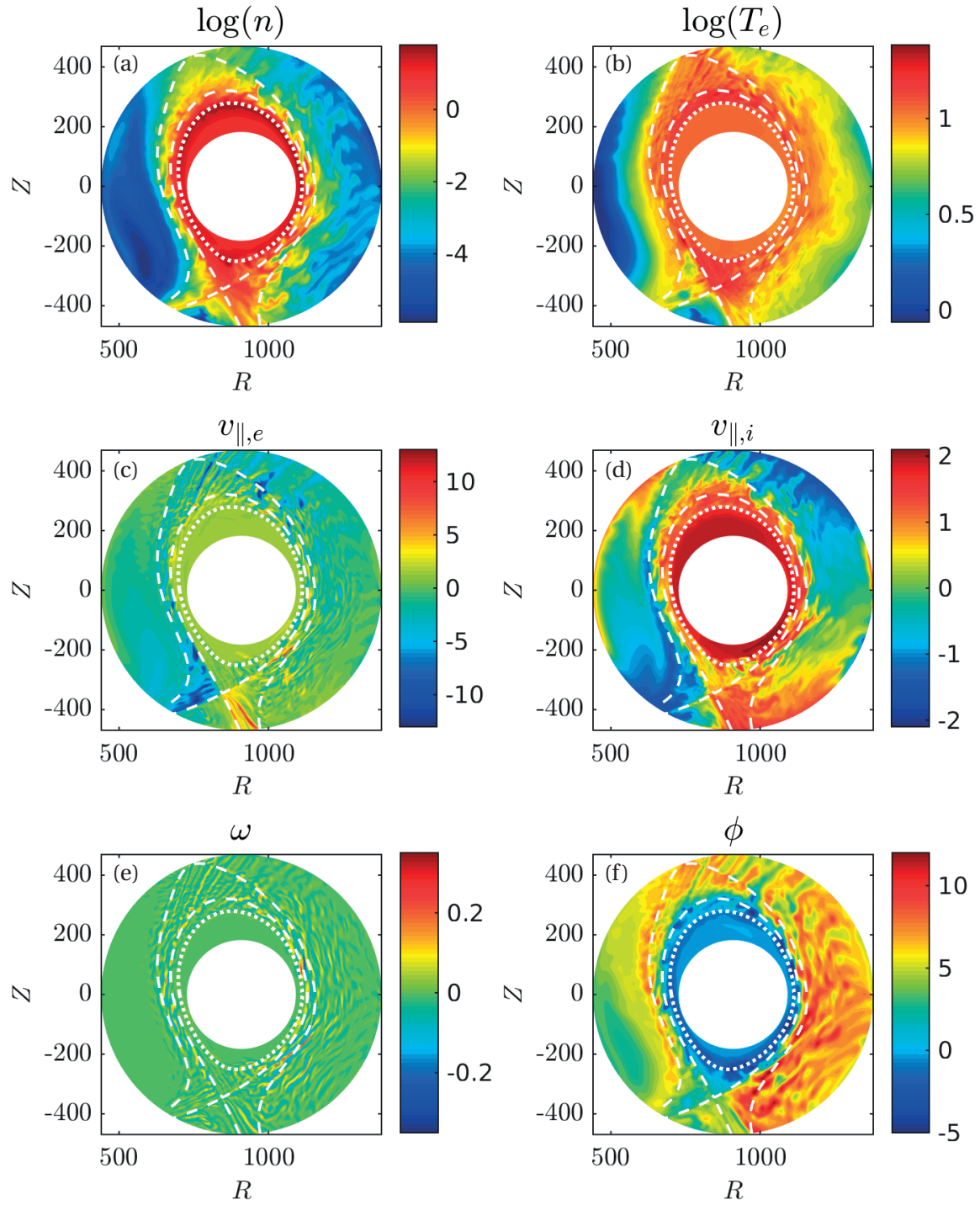


Figure 5.9 – Typical poloidal snapshots of plasma quantities for TCV-like simulation.

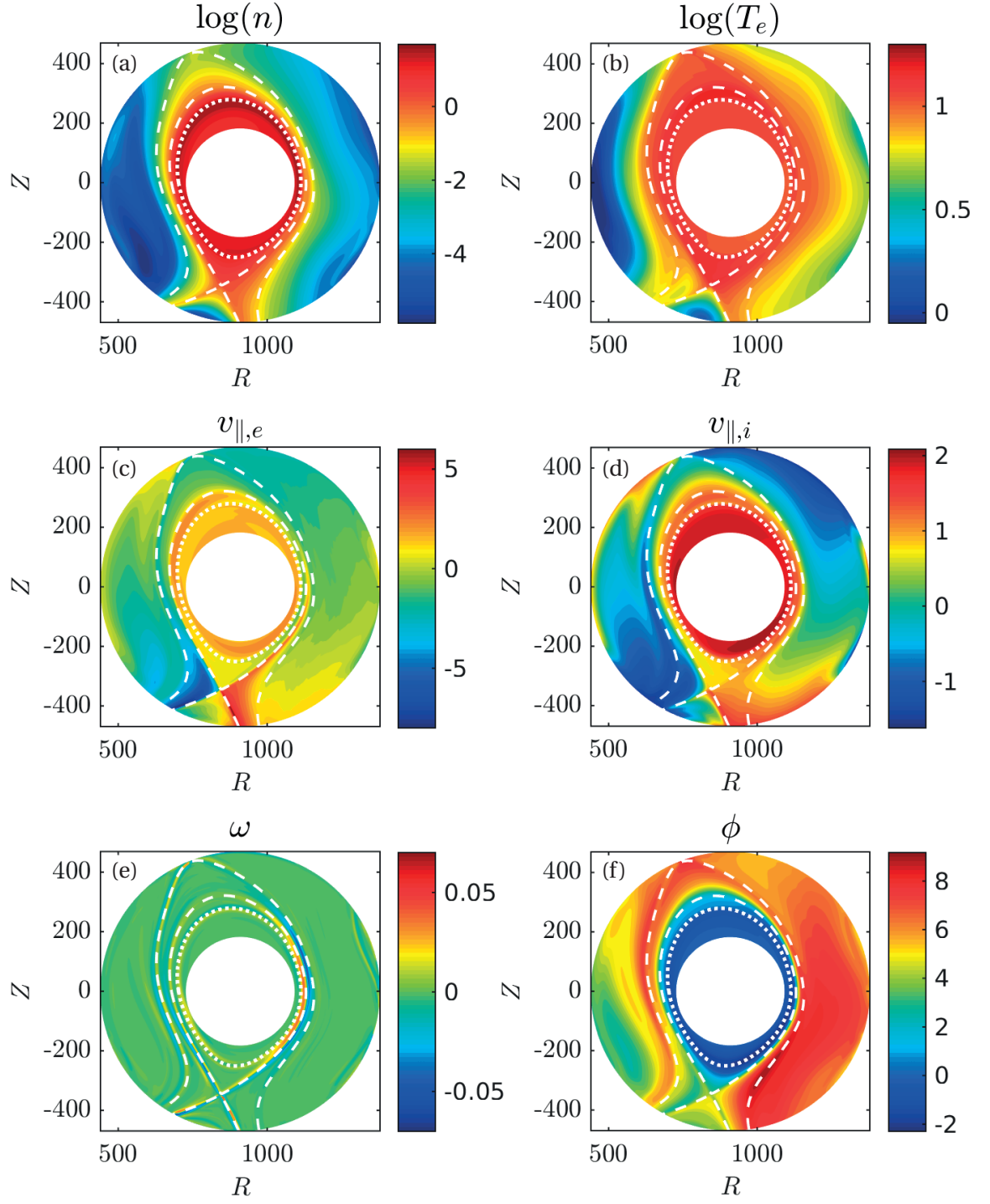


Figure 5.10 – Poloidal cross-section of time and toroidally averaged plasma quantities for TCV-like simulation.

5.3.1 Radial turbulent transport

At the LFS, ∇p and ∇B point in the same direction, the edge interchange modes become unstable and most of the plasma radial transport is localised in this region. Fig. 5.11 (left) illustrates the turbulent radial flux due to the $\mathbf{E} \times \mathbf{B}$ velocity:

$$\langle n_{fl} \mathbf{v}_{E,fl} \cdot \mathbf{u}_\psi \rangle_{t,\varphi} = \langle (n - \bar{n}) (\mathbf{v}_E - \bar{\mathbf{v}}_E) \cdot \frac{\nabla \psi}{\|\nabla \psi\|} \rangle_{t,\varphi} \stackrel{\text{Eq. (4.1.9)}}{=} \langle (n - \bar{n}) \frac{[\phi - \bar{\phi}, \psi]}{\|\nabla \psi\|} \rangle_{t,\varphi} \quad (5.3.1)$$

with ∇ in ρ_{s0} units and \mathbf{u}_ψ unitary vector pointing in the direction orthogonal to the flux surface, i.e. $\mathbf{u}_\psi = \nabla \psi / \|\nabla \psi\|$. As expected, in the simulation the flux is higher at the LFS and almost negligible at the HFS. The turbulent flux intensifies around the upper part of the outer leg. This is due to the flux expansion in the region, as explained by Galassi *et al.* [82]: “the parallel transport tends to homogenize the plasma structures on a flux surface [...]. For this reason, the perpendicular transport tends to adapt its behaviour according to the local flux expansion, resulting in stronger fluxes where further flux surfaces must be reached in order to keep the turbulent structures almost field-aligned”. The radial flux in Eq. (5.3.1) indicates the transport in physical space, rather than the transport from one flux surfaces to the next. The latter is given by:

$$\langle n_{fl} \mathbf{v}_{E,fl} \cdot \nabla \psi \rangle_{t,\varphi} = \langle (n - \bar{n}) [\phi - \bar{\phi}, \psi] \rangle_{t,\varphi} \quad (5.3.2)$$

Since $\mathbf{v} \cdot \nabla \psi = (d\mathbf{x}/dt) \cdot (d\psi/d\mathbf{x}) = d\psi/dt$, Eq. (5.3.2) describes the $\mathbf{E} \times \mathbf{B}$ transport across flux surfaces. Fig. 5.11 (right) shows the resulting transport in $d\psi$ presenting a very clear and more up-down symmetric ballooning behaviour with respect to transport in physical space (left).

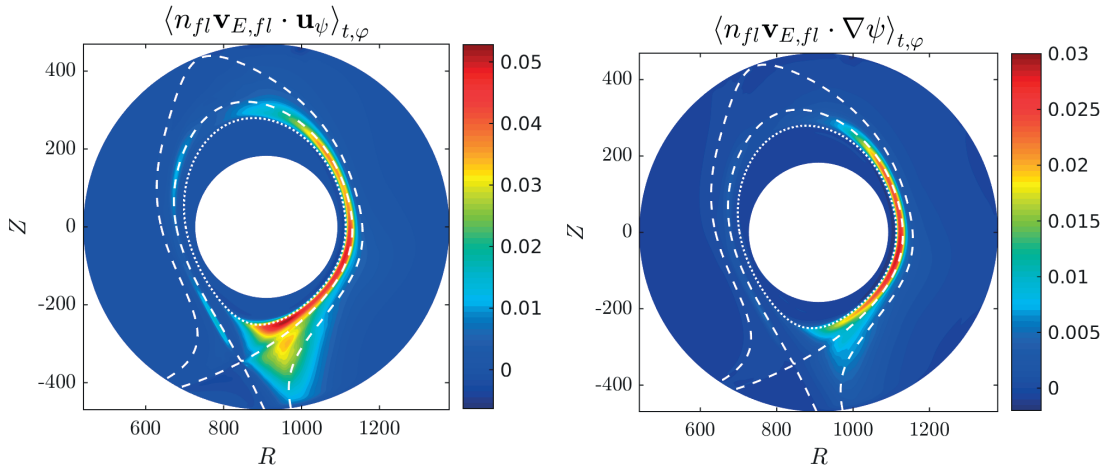


Figure 5.11 – Two different estimates of the turbulent transport orthogonal to the flux surface. The left panel shows transport in physical space, the right panel shows transport in ψ .

From the physical picture of turbulent transport, blobs (holes) form from edge interchange modes and move radially outwards (inwards) giving rise to positive (negative) intermittent

fluctuations in the SOL (edge) [43]. As previously mentioned in chapter 4, intermittency and asymmetry of fluctuations in the edge and SOL have been widely recorded in both simulations and experiments (for example [83]). The same behaviour is seen in this simulation, as shown in Fig. 5.12, where the ion saturation current, $I_{sat} = nc_s$, taken at the outboard midplane of SOL (left) and edge (right) is plotted in time, simulating a Langmuir probe signal used in experiments. The positive asymmetry of the signal is clear in the SOL, while in the edge signal is almost symmetric. Further analysis shows that the simulation I_{sat} peaks come from the plasma density rather than the plasma temperature, as can be inferred from the fluctuation plot of $\log(n)$ and $\log(T_e)$ in Fig. 5.9, panels (a) and (b).

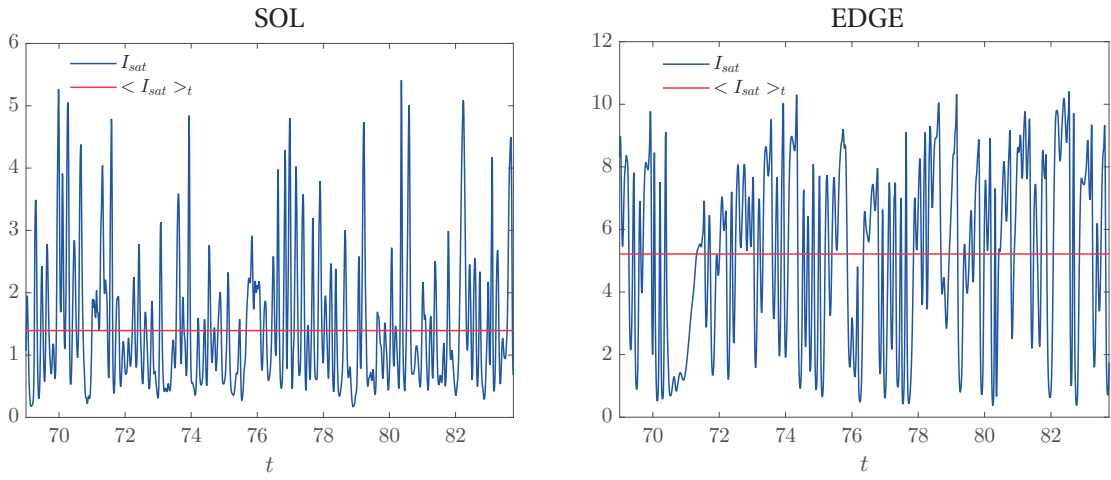


Figure 5.12 – I_{sat} fluctuation at the outboard midplane in the SOL (left) and at the edge (right) displaying intermittent behaviour typical of blob turbulent transport. I_{sat} peaks in the SOL are associated with blobs and I_{sat} sinks in the edge with holes.

Figure 5.13 shows a time lapse of the plasma pressure at the outboard midplane around $t = 80.3$, where the I_{sat} peaks in the SOL (Fig. 5.12). The two crosses indicate the locations at which the I_{sat} signal for edge and SOL is detected. It is believed that holes detach from the edge unstable modes and propagate radially inwards [43]. Consequently, in order to detect their presence, one should be at a location $\psi < \psi_{MODE}$, with ψ_{MODE} flux surface of the edge mode location. In this simulation, though, the edge mode location coincides with the source location and the region $\psi < \psi_{src}$ is excluded from the physical analysis. This explains why I_{sat} edge in Fig. 5.12 (right), detected outside the source location, does not show a clear asymmetry.

In Fig. 5.13, the crests of an unstable mode extend from the edge into the SOL and are sheared around the separatrix location. The crest around midplane evolves into a blob, detached from the main plasma, moves radially outwards and sees a sharp decrease in its peak pressure value. The negative bursts in I_{sat} Fig. 5.12 (right) are due to the detection of the minimum of the edge mode while it moves poloidally. The dynamics of the holes are not present in this simulation, possibly because of insufficient radial extension of the domain towards the core.

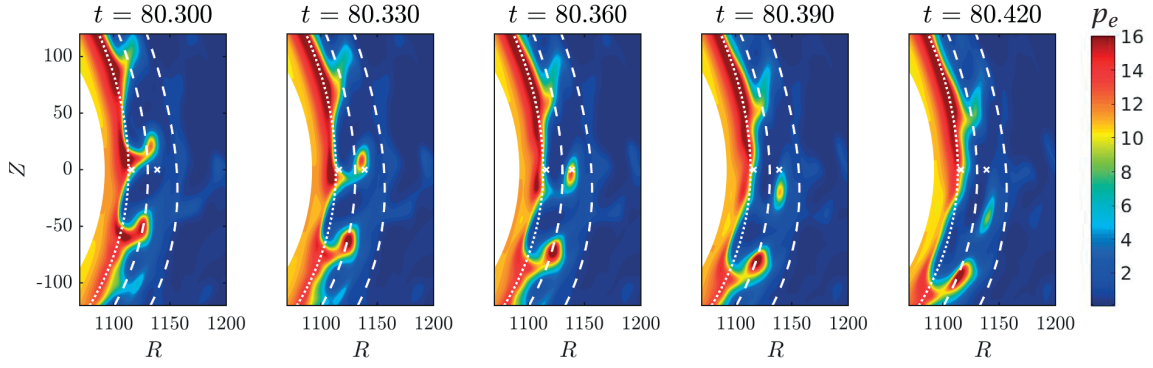


Figure 5.13 – Time frames of electron pressure at the outer midplane showing the formation of a blob from an edge interchange mode, which is rotating poloidally. The dotted line traces the source location, while the staggered lines correspond to the separatrix and the last connected flux surface. The two crosses indicate the locations at which the I_{sat} signals for edge and SOL in Fig. 5.12 are detected.

5.3.2 Poloidal rotation

The pressure sequence in figure 5.13 suggests that the plasma in the edge is rotating poloidally. In principle, both to $\mathbf{E} \times \mathbf{B}$ drift and parallel velocity can contribute to the poloidal rotation. The $\mathbf{E} \times \mathbf{B}$ drift in the poloidal direction, $v_{E,pol}$, is generated by the drop in electric potential around the separatrix. From the ϕ average poloidal profile in Fig. 5.10 we see that $\nabla\phi$ point radially outwards, $\mathbf{B} \sim \mathbf{B}_{tor}$ enters the plane (see Fig. 5.1), and therefore $\mathbf{E} \times \mathbf{B} = -\nabla\phi \times \mathbf{B}$ creates a clockwise rotation, in qualitative agreement with the blob motion in Fig. 5.13. The use of “poloidal” here indicates the direction orthogonal to $\nabla\psi$ and $\nabla\phi$ and does not coincide with e_θ . We can compute $v_{E,pol}$ as:

$$v_{E,pol} = \frac{\tilde{v}_E}{c_{s0}} = \frac{\tilde{\mathbf{v}}_E}{c_{s0}} \cdot \frac{\tilde{\nabla}\phi \times \tilde{\nabla}\tilde{\psi}}{||\tilde{\nabla}\phi \times \tilde{\nabla}\tilde{\psi}||} = \frac{c}{B_0 c_{s0}} (\mathbf{b} \times \tilde{\nabla}\phi) \cdot \frac{(\tilde{\nabla}\phi \times \tilde{\nabla}\tilde{\psi})}{||\tilde{\nabla}\phi \times \tilde{\nabla}\tilde{\psi}||} = \frac{c}{B_0 c_{s0}} \tilde{b}^\phi \frac{\tilde{\nabla}\phi \cdot \tilde{\nabla}\tilde{\psi}}{||\tilde{\nabla}\phi \times \tilde{\nabla}\tilde{\psi}||}$$

$$= \left(\frac{\partial\psi}{\partial\hat{r}} \frac{\partial\phi}{\partial r} + \frac{1}{\hat{r}} \frac{\partial\psi}{\partial\theta} \frac{1}{r} \frac{\partial\phi}{\partial\theta} \right) / \sqrt{\left(\frac{\partial\psi}{\partial\hat{r}} \right)^2 + \left(\frac{1}{\hat{r}} \frac{\partial\psi}{\partial\theta} \right)^2} \quad (5.3.3)$$

Where we used the magnetic field definition in toroidal coordinates, see Sec.2.2.3, as well as the vector identity $(\mathbf{A} \times \mathbf{B}) \cdot (\mathbf{C} \times \mathbf{D}) = (\mathbf{A} \cdot \mathbf{C})(\mathbf{B} \cdot \mathbf{D}) - (\mathbf{A} \cdot \mathbf{D})(\mathbf{B} \cdot \mathbf{C})$. Fig. 5.14 (left) shows $v_{E,pol}$ averaged in time and ϕ , with positive values corresponding to clockwise motion. The rotation is stronger at the LFS and peaks at the separatrix, in agreement with the physical understanding of blob generation being caused by the high $\mathbf{E} \times \mathbf{B}$ shear at the separatrix. We do not investigate the negative values of poloidal rotation in the closed flux surface region, as they are located inside the source region (in white dotted line).

As mentioned, the parallel velocity can contribute to the poloidal rotation. The parallel velocity $v_{||i}$ is positive in the core (see Fig. 5.10) and since the magnetic field wraps around the flux-surfaces clockwise (see Fig.5.1), $v_{||i}$ contributes to the clockwise rotation. The parallel

contribution is computed as:

$$\begin{aligned}
 v_{\parallel i, pol} &= v_{\parallel i} \mathbf{b} \cdot \frac{\tilde{\nabla} \varphi \times \tilde{\nabla} \tilde{\psi}}{\|\tilde{\nabla} \varphi \times \tilde{\nabla} \tilde{\psi}\|} \stackrel{\text{Eq. (2.2.5)}}{=} \frac{v_{\parallel i}}{B_0} \|\tilde{\nabla} \varphi \times \tilde{\nabla} \tilde{\psi}\| \\
 &= v_{\parallel i} \frac{a}{R_0} \sqrt{\left(\frac{\partial \psi}{\partial \hat{r}}\right)^2 + \left(\frac{1}{\hat{r}} \frac{\partial \psi}{\partial \theta}\right)^2}
 \end{aligned} \tag{5.3.4}$$

Hence $v_{\parallel i, pol}$ is given by the parallel ion velocity and the poloidal component of the magnetic field. $v_{\parallel i, pol}$, Fig. 5.14, mimics $\partial_{\hat{r}} \psi$, Fig. 5.2 top-left panel, especially in the region closer to the core boundary where $v_{\parallel i}$ average value is almost constant, Fig. 5.10 (d), and $\partial_{\theta} \psi / \hat{r}$ is small, Fig. 5.2 top-left panel. At the outboard midplane, the magnitude of $v_{E, pol}$ is comparable to $v_{\parallel i}$ in the edge and dominates in the SOL.

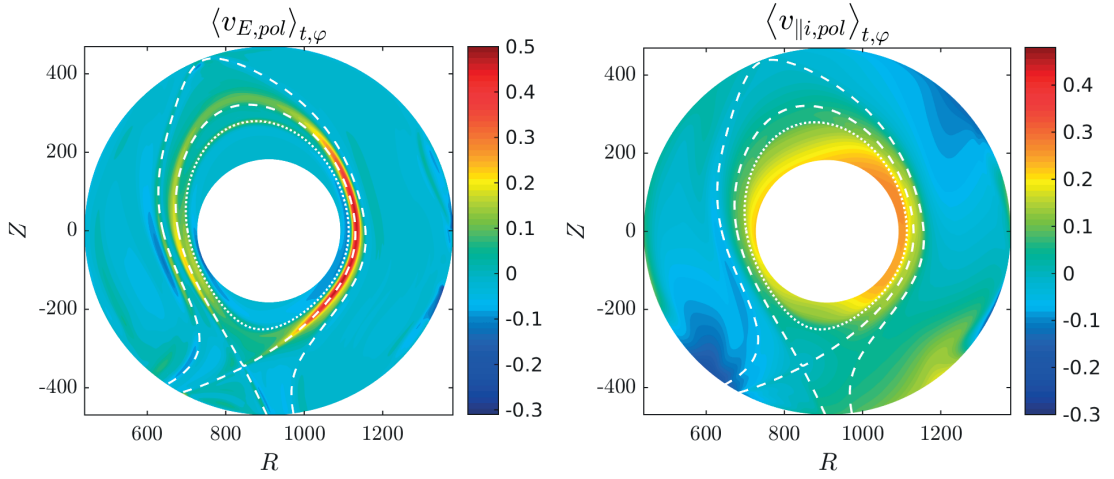


Figure 5.14 – Time and toroidally averaged poloidal velocity due to the $\mathbf{E} \times \mathbf{B}$ drift (left) and to the parallel ion velocity $v_{\parallel i}$ (right).

5.4 Outlook

The simulation results presented in Sec. 5.3 open up the possibility to investigate physical mechanisms that influence the plasma dynamics in the periphery of diverted tokamaks, which are not entirely understood yet. Some of the open questions that the current version of GBS could help answering are: the self-consistent generation drop in the electric potential ϕ across the separatrix leading to the $\mathbf{E} \times \mathbf{B}$ shear, the relation between ϕ profile and separatrix location, the blob generation mechanism, the circulation pattern around the X-point, the role of various physical parameters such as parallel viscosity and parallel heat conductivity on the turbulent dynamics and on the heat flux at the wall, the role on the ∇B drift (by inverting the direction of the toroidal magnetic field).

There are currently still shortcomings in the model that need to be addressed before proceeding to quantitative comparison with experiment. In particular the impact of the inner radial

boundary conditions on the SOL physics requires further investigation. In section 5.2.4, after observing unrealistically high values of Mach numbers, a source of parallel momentum, acting as a friction term for the conservation of parallel momentum, and a limits for the inner radial boundary conditions were introduced. The combination of the two lead to a drop in Mach numbers towards more physical values.

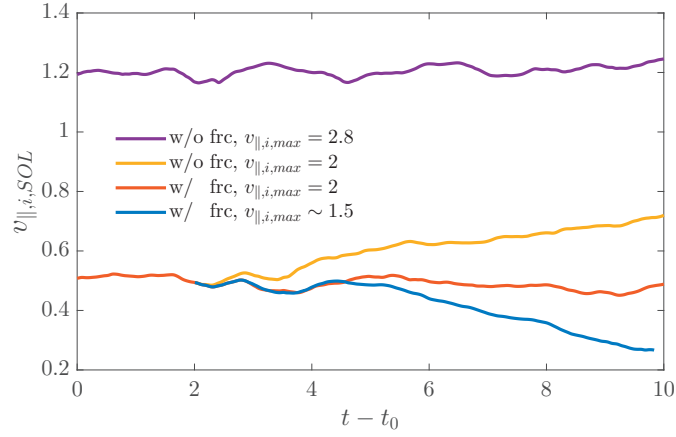


Figure 5.15 – Time traces of average $v_{||,i}$ values in the SOL for 4 different simulations highlighting the effect on the SOL dynamics of the additional friction term in the parallel momentum equations (w/ or w/o fric) and of the maximal $v_{||,i}$ value used at inner radial boundary condition ($v_{||,i,max}$). The purple and red line correspond to the two simulations at quasi steady state analysed in Sec. 5.2.4 and in Sec. 5.3, whose Mach number is compared in Fig. 5.6. The time axis has been shifted and starts at the beginning of the quasi-steady state for the two simulations.

Fig. 5.15 shows the impact of these two factors on the SOL physics. Time traces of average parallel ion velocities in the SOL, $v_{||,i,SOL}$, are shown for 4 different simulations. The purple (red) line correspond to the quasi-steady states characterised by high (low) Mach number investigated in Sec. 5.2.4 (Sec. 5.3). The time axis has been shifted to start at the beginning of the quasi-steady state for the two simulations. The yellow and blue lines show the trend of other two simulations started for the one with low Mach number in red line, where the momentum source and the inner value of the parallel ion velocity were changed individually. It is clear from these trends that both factors impact the parallel ion velocity in the SOL. The necessity of introducing the source terms was motivated in Sec. 5.2.4, conversely, the choice of $v_{||,i,max} = 2$ for the inner boundary is arbitrary and it should in principle not impact the dynamics in the SOL. In fact, the location of the density source on a flux surface between SOL and inner boundaries should help decoupling the two. This is clearly not the case in this simulation and further investigation is required to understand what is the impact, or alternatively, a physically motivated choice of inner radial boundary conditions should be implemented in GBS.

6 Summary

In this thesis, a new version of GBS for the treatment of diverted equilibria is presented, successfully tested, and used to investigate turbulence in the tokamak periphery.

With respect to the limited version of GBS we abandon the use of flux aligned coordinates and use toroidal coordinates (r, θ, φ) instead (Sec. 1.3). A choice motivated by the singularity of flux coordinates at the X-point, which is by definition a saddle point for the poloidal flux, meaning that $\nabla\psi = 0$ and hence the Jacobian $J \propto (\nabla\psi)^{-1} = \infty$. In addition to being locally ill-defined, flux coordinates in diverted configuration makes it challenging from a numerical point of view to obtain good physical resolution around the X-point, due to the increasing distance between flux surfaces when approaching the X-point.

Toroidal coordinates, on the other hand, are defined everywhere and lead to relatively uniform grid spacing, especially in tokamak periphery far from the coordinates axis. Moreover, they do not require domain decomposition, often used in the case of flux coordinates in order to guarantee a structured grid. The obvious downside is the lack of alignment to the magnetic field and the impossibility of taking advantage of the difference in length scales between the direction parallel and perpendicular to the magnetic field line, to reduce the computational cost.

The use of a new coordinate system, requires the re-definition of the parallel $(\nabla_{\parallel}, \nabla_{\parallel}^2)$ and perpendicular $([\phi,], C(), \nabla_{\perp}^2)$ operators, present in the drift-reduced Braginskii's equations, solved by GBS (Sec. 2.2). Simply projecting them onto the toroidal basis gives rise to operator expressions that are fully three dimensional in (r, θ, φ) , causing the typical length scales of parallel and perpendicular gradients to mix. This would lead to an increase of the computational cost, due to the necessity of using a refined grid in all directions. Furthermore, and most importantly, the solution of $\nabla_{\perp}^2 \phi = \omega$ for the electric potential would require the inversion of a full 3D operator at each time step, which is extremely computationally expensive. Fortunately, under the assumption of large machine aspect ratio and safety factor, the component in the toroidal direction of the perpendicular operators can be neglected, leading to bi-dimensional expression for $[\phi,], C()$, and ∇_{\perp}^2 , which, incidentally, are independent from the poloidal flux ψ in their final form. The parallel operators can not be simplified under the same assumptions. Hence, they remain fully 3D and they contain all the information on the poloidal flux shape.

To compensate for the lack of alignment between toroidal coordinates and magnetic field, the spatial accuracy of the numerical scheme is increased from second to fourth order, and additional grid staggering is added in the poloidal direction (Sec. 3.2). This numerical scheme allows for an efficient code parallelisation. A benchmark between the new version of GBS and previous version is performed in circular limited configuration, showing excellent quantitative agreement in the prediction of the SOL width (mainly dependent on the perpendicular radial dynamics) and of the fluctuation spectrum on the flux surface (mainly dependent on the parallel dynamics) (Sec. 3.5). The study of diverted equilibria required the additional implementation of the magnetic pre-sheath boundary condition at the wall and at the divertor legs, complicated by the presence of points where the magnetic field line is tangent to the wall, for which the physical model fails (Sec. 3.3). The code is verified with the method of manufactured solution in the case of a simple X-point configuration, proving the correct implementation of the fourth order differential operators (Sec. 3.6). Finally, the simple X-point configuration is run with three different grid size resolutions. The results at quasi-steady state are compared and prove that the code converges as the grid size decreases (Sec. 3.7).

The new version of GBS is used to investigate blob dynamics in the presence of an X-point. An analytical scaling for the blob velocity as a function of the blob size and plasma collisionality is derived starting from the two-region model in Ref. [24] (Sec. 4.1). This model accounts for the difference in the physical mechanisms and in the magnetic field geometry that characterise the outboard midplane and the divertor regions. The scaling is re-derived starting from a simplified version of the drift-reduced Braginskii's equations for density and vorticity and providing a closure for the parallel dynamics, using Ohm's law and the magnetic pre-sheath physics. The final scalings retains the effect of finite background plasma density and blob ellipticity that are not present in Ref. [24].

A simulation is run in a double-null configuration, a blob detection/tracking algorithm is developed and used to compute blob velocities, sizes and other physical parameters needed to perform a comparison between simulation results and analytical scaling (Sec. 4.2). The blobs appear to be in the high-collisionality Resistive Ballooning and Resistive X regimes of the two-region model, where the curvature drive is balanced by the perpendicular ion polarisation current and parallel current flow between the two regions, respectively (Sec. 4.3). The plot of the detected blob velocities as a function of their sizes has the derived analytical scaling for the two regimes as upper limits. The effect of finite background density and ellipticity are shown to be quantitatively important, although the qualitative trends are unchanged. A detailed analysis of two blobs, one in Resistive X and one in Resistive Ballooning, show density and electric potential fluctuations as well as parallel current profiles that are in agreement with the theoretical physical picture. This is the first time that a blob velocity scaling is investigated using full-3D turbulent simulation in diverted geometry.

Finally, the TCV diverted equilibrium from discharge #49633 is implemented in the new version of GBS (Sec. 5). Results of this simulation produced unrealistically high Mach numbers, partly attributed to the lack of friction source terms in the physical model for the parallel momentum equations (Sec. 5.2.4). The updated model resulted in a better agreement with the general

physical understanding of plasma turbulence in the periphery of diverted tokamaks (Sec. 5.3). The simulated Langmuir probe I_{sat} signals are typical of turbulent dynamics characterised by the presence of blobs (Sec. 5.3.1). The electric potential drop across the separatrix, going from positive values in the SOL to negative values in the edge, is in agreement with experimental observations. The resulting peak in the $\mathbf{E} \times \mathbf{B}$ velocity at the separatrix appears to be linked with blob formation at the outer-mid plane (Sec. 5.3.2). The *ad-hoc* inner radial boundary conditions are shown to impact the SOL dynamics, suggesting that further investigation is required before proceeding towards quantitative comparison with the experimental results (Sec. 5.4).

To conclude, in this thesis the GBS code has been advanced to simulate the periphery of diverted tokamaks, by using *non*-flux-aligned coordinates. The new verified version of GBS has been used to investigate blob transport mechanisms, showing agreement with theoretical models. A preliminary analysis of a TCV-like simulation shows that the current version of GBS is able to address open questions regarding plasma dynamics in the periphery, such as blob generation mechanisms, formation of potential drops, and the effects of plasma toroidal rotation on SOL physics. Quantitative comparison with the experimental results is possible after a careful investigation of the inner radial boundary conditions.

Bibliography

- [1] J. Wesson and D. J. Campbell, *Tokamaks*, vol. 149. Oxford University Press, 2011.
- [2] “The merits of fusion.” <http://fusionforenergy.europa.eu/understandingfusion/merits.aspx>.
- [3] J. Ball and J. P. Parisi, *The Future of Fusion Energy*. World Scientific Publishing, 2018.
- [4] F. Wagner, “Electricity by intermittent sources: An analysis based on the german situation 2012,” *The European Physical Journal Plus*, vol. 129, no. 2, p. 20, 2014.
- [5] X. Sillen, J. Marivoet, and M. Zucchetti, “Analysis of human intrusion scenarios for the deep disposal of fusion wastes,” *Fusion engineering and design*, vol. 54, no. 3-4, pp. 575–581, 2001.
- [6] T. Eich, B. Sieglin, A. Scarabosio, W. Fundamenski, R. J. Goldston, and A. Herrmann, “Inter-ELM Power Decay Length for JET and ASDEX Upgrade: Measurement and Comparison with Heuristic Drift-Based Model,” *Physical Review Letters*, vol. 107, Nov. 2011.
- [7] G. F. Matthews, P. Edwards, T. Hirai, M. Kear, A. Lioure, P. Lomas, A. Loving, C. Lungu, H. Maier, P. Mertens, D. Neilson, R. Neu, J. Pamela, V. Philipps, G. Piazza, V. Riccardo, M. Rubel, C. Ruset, E. Villedieu, M. Way, and t. I.-I. W. P. Team, “Overview of the ITER-like wall project,” *Physica Scripta*, vol. T128, pp. 137–143, Mar. 2007.
- [8] A. Loarte, B. Lipschultz, A. Kukushkin, G. Matthews, P. Stangeby, N. Asakura, G. Counsell, G. Federici, A. Kallenbach, K. Krieger, *et al.*, “Power and particle control,” *Nuclear Fusion*, vol. 47, no. 6, p. S203, 2007.
- [9] B. Dudson, A. Allen, G. Breyiannis, E. Brugger, J. Buchanan, L. Easy, S. Farley, I. Joseph, M. Kim, A. McGann, *et al.*, “Bout++: Recent and current developments,” *Journal of Plasma Physics*, vol. 81, no. 1, 2015.
- [10] P. Tamain, H. Bufferand, G. Ciraolo, C. Colin, D. Galassi, P. Ghendrih, F. Schwander, and E. Serre, “The tokam3x code for edge turbulence fluid simulations of tokamak plasmas in versatile magnetic geometries,” *J. Comput. Phys.*, vol. 321, pp. 606–623, Sept. 2016.
- [11] B. Zhu, M. Francisquez, and B. N. Rogers, “Global 3d two-fluid simulations of the tokamak edge region: Turbulence, transport, profile evolution, and spontaneous $e \times b$ rotation,” *Physics of Plasmas*, vol. 24, no. 5, p. 055903, 2017.

Bibliography

- [12] A. Stegmeir, D. P. Coster, A. Ross, O. Maj, K. Lackner, and E. Poli, “Grillix: A 3d turbulence code based on the flux-coordinate independent approach,” *Plasma Physics and Controlled Fusion*, 2017.
- [13] A. H. Nielsen, G. Xu, J. Madsen, V. Naulin, J. J. Rasmussen, and B. Wan, “Simulation of transition dynamics to high confinement in fusion plasmas,” *Physics Letters A*, vol. 379, no. 47, pp. 3097–3101, 2015.
- [14] S. I. Braginskii, “Transport Processes in a Plasma,” *Reviews of Plasma Physics*, vol. 1, p. 205, 1965.
- [15] A. Zeiler, J. F. Drake, and B. Rogers, “Nonlinear reduced braginskii equations with ion thermal dynamics in toroidal plasma,” *Physics of Plasmas*, vol. 4, no. 6, pp. 2134–2138, 1997.
- [16] F. D. Halpern, P. Ricci, B. Labit, I. Furno, S. Jolliet, J. Loizu, A. Masetto, G. Arnoux, J. Gunn, J. Horacek, *et al.*, “Theory-based scaling of the sol width in circular limited tokamak plasmas,” *Nuclear Fusion*, vol. 53, no. 12, p. 122001, 2013.
- [17] F. Riva, E. Lanti, S. Jolliet, and P. Ricci, “Plasma shaping effects on tokamak scrape-off layer turbulence,” *Plasma Physics and Controlled Fusion*, vol. 59, no. 3, p. 035001, 2017.
- [18] J. P. Freidberg, *Ideal MHD*. Cambridge University Press, 2014.
- [19] F. Hariri and M. Ottaviani, “A flux-coordinate independent field-aligned approach to plasma turbulence simulations,” *Computer Physics Communications*, vol. 184, no. 11, pp. 2419–2429, 2013.
- [20] A. Stegmeir, D. Coster, O. Maj, K. Hallatschek, and K. Lackner, “The field line map approach for simulations of magnetically confined plasmas,” *Computer Physics Communications*, vol. 198, pp. 139–153, 2016.
- [21] B. LaBombard, E. Marmor, J. Irby, J. Terry, R. Vieira, G. Wallace, D. Whyte, S. Wolfe, S. Wukitch, S. Baek, *et al.*, “Adx: a high field, high power density, advanced divertor and rf tokamak,” *Nuclear Fusion*, vol. 55, no. 5, p. 053020, 2015.
- [22] R. Ambrosino, R. Albanese, S. Coda, M. Mattei, J.-M. Moret, and H. Reimerdes, “Optimization of experimental snowflake configurations on tcv,” *Nuclear Fusion*, vol. 54, no. 12, p. 123008, 2014.
- [23] F. Halpern, P. Ricci, S. Jolliet, J. Loizu, J. Morales, A. Masetto, F. Musil, F. Riva, T. Tran, and C. Wersal, “The {GBS} code for tokamak scrape-off layer simulations,” *Journal of Computational Physics*, vol. 315, pp. 388 – 408, 2016.
- [24] J. Myra, D. Russell, and D. D’Ippolito, “Collisionality and magnetic geometry effects on tokamak edge turbulent transport. i. a two-region model with application to blobs,” *Physics of plasmas*, vol. 13, no. 11, p. 112502, 2006.

-
- [25] A. Masetto, “Turbulent regimes in the tokamak scrape-off layer,” 2014.
- [26] P. Ricci, F. Halpern, S. Jolliet, J. Loizu, A. Masetto, A. Fasoli, I. Furno, and C. Theiler, “Simulation of plasma turbulence in scrape-off layer conditions: the gbs code, simulation results and code validation,” *Plasma Physics and Controlled Fusion*, vol. 54, no. 12, p. 124047, 2012.
- [27] A. Masetto, F. D. Halpern, S. Jolliet, J. Loizu, and P. Ricci, “Finite ion temperature effects on scrape-off layer turbulence,” *Physics of Plasmas*, vol. 22, no. 1, p. 012308, 2015.
- [28] F. D. Halpern, S. Jolliet, J. Loizu, A. Masetto, and P. Ricci, “Ideal ballooning modes in the tokamak scrape-off layer,” *Physics of Plasmas*, vol. 20, no. 5, p. 052306, 2013.
- [29] C. Wersal and P. Ricci, “A first-principles self-consistent model of plasma turbulence and kinetic neutral dynamics in the tokamak scrape-off layer,” *Nuclear Fusion*, vol. 55, no. 12, p. 123014, 2015.
- [30] W. D. D’haeseleer, W. N. Hitchon, J. D. Callen, and J. L. Shohet, *Flux coordinates and magnetic field structure: a guide to a fundamental tool of plasma theory*. Springer Science & Business Media, 2012.
- [31] J. Loizu, P. Ricci, F. D. Halpern, and S. Jolliet, “Boundary conditions for plasma fluid models at the magnetic presheath entrance,” *Physics of Plasmas*, vol. 19, no. 12, p. 122307, 2012.
- [32] F. H. Harlow and J. E. Welch, “Numerical calculation of time dependent viscous incompressible flow of fluid with free surface,” *The Physics of Fluids*, vol. 8, no. 12, pp. 2182–2189, 1965.
- [33] S. Patankar, *Numerical heat transfer and fluid flow*. CRC press, 1980.
- [34] A. Arakawa, “Computational design for long-term numerical integration of the equations of fluid motion: Two-dimensional incompressible flow. part i,” *Journal of Computational Physics*, vol. 1, no. 1, pp. 119 – 143, 1966.
- [35] J. L. Peterson and G. W. Hammett, “Positivity preservation and advection algorithms with applications to edge plasma turbulence,” *SIAM Journal on Scientific Computing*, vol. 35, no. 3, pp. B576–B605, 2013.
- [36] J. Moritz, E. Faudot, S. Devaux, and S. Heuraux, “The plasma-wall transition layers in the presence of collisions with a magnetic field parallel to the wall,” *Physics of Plasmas*, vol. 25, no. 1, p. 013534, 2018.
- [37] D. Coulette and G. Manfredi, “Kinetic simulations of the chodura and debye sheaths for magnetic fields with grazing incidence,” *Plasma Physics and Controlled Fusion*, vol. 58, no. 2, p. 025008, 2016.

Bibliography

- [38] P. R. Amestoy, I. S. Duff, J. Koster, and J.-Y. L'Excellent, "A fully asynchronous multifrontal solver using distributed dynamic scheduling," *SIAM Journal on Matrix Analysis and Applications*, vol. 23, no. 1, pp. 15–41, 2001.
- [39] P. R. Amestoy, A. Guermouche, J.-Y. L'Excellent, and S. Pralet, "Hybrid scheduling for the parallel solution of linear systems," *Parallel Computing*, vol. 32, no. 2, pp. 136–156, 2006.
- [40] P. J. Roache, "Code verification by the method of manufactured solutions," *Journal of Fluids Engineering*, vol. 124, no. 1, pp. 4–10, 2002.
- [41] F. Riva, P. Ricci, F. D. Halpern, S. Jolliet, J. Loizu, and A. Masetto, "Verification methodology for plasma simulations and application to a scrape-off layer turbulence code," *Physics of Plasmas*, vol. 21, no. 6, p. 062301, 2014.
- [42] I. Wolfram Research, "Mathematica," 2015.
- [43] D. D'Ippolito, J. Myra, and S. Zweben, "Convective transport by intermittent blob-filaments: Comparison of theory and experiment," *Physics of Plasmas*, vol. 18, no. 6, p. 060501, 2011.
- [44] J. A. Boedo, D. L. Rudakov, R. A. Moyer, G. R. McKee, R. J. Colchin, M. J. Schaffer, P. Stangeby, W. West, S. L. Allen, T. E. Evans, *et al.*, "Transport by intermittency in the boundary of the diii-d tokamak," *Physics of Plasmas*, vol. 10, no. 5, pp. 1670–1677, 2003.
- [45] S. Zweben, "Search for coherent structure within tokamak plasma turbulence," *The Physics of fluids*, vol. 28, no. 3, pp. 974–982, 1985.
- [46] J. Terry, S. Zweben, K. Hallatschek, B. LaBombard, R. Maqueda, B. Bai, C. Boswell, M. Greenwald, D. Kopon, W. Nevins, *et al.*, "Observations of the turbulence in the scrape-off-layer of alcator c-mod and comparisons with simulation," *Physics of Plasmas*, vol. 10, no. 5, pp. 1739–1747, 2003.
- [47] B. Goncalves, C. Hidalgo, C. Silva, M. Pedrosa, and K. Erents, "Statistical description of the radial structure of turbulence in the jet plasma boundary region," *Journal of nuclear materials*, vol. 337, pp. 376–380, 2005.
- [48] H. Tanaka, N. Ohno, N. Asakura, Y. Tsuji, H. Kawashima, S. Takamura, Y. Uesugi, *et al.*, "Statistical analysis of fluctuation characteristics at high-and low-field sides in l-mode sol plasmas of jt-60u," *Nuclear Fusion*, vol. 49, no. 6, p. 065017, 2009.
- [49] N. Fedorczak, J. P. Gunn, P. Ghendrih, P. Monier-Garbet, and A. Pocheau, "Flow generation and intermittent transport in the scrape-off-layer of the tore supra tokamak," *Journal of Nuclear Materials*, vol. 390, pp. 368–371, 2009.
- [50] O. E. Garcia, J. Horacek, R. Pitts, A. H. Nielsen, W. Fundamenski, V. Naulin, and J. J. Rasmussen, "Fluctuations and transport in the tcv scrape-off layer," *Nuclear fusion*, vol. 47, no. 7, p. 667, 2007.

-
- [51] U. Pfeiffer, M. Endler, J. Bleuel, H. Niedermeyer, and G. Theimer, "Density, temperature and potential fluctuation measurements with multiple fast swept langmuir probes on w7-as," *Contributions to Plasma Physics*, vol. 38, no. S1, pp. 134–144, 1998.
- [52] T. Happel, F. Greiner, N. Mahdizadeh, B. Nold, M. Ramisch, and U. Stroth, "Generation of intermittent turbulent events at the transition from closed to open field lines in a toroidal plasma," *Physical review letters*, vol. 102, no. 25, p. 255001, 2009.
- [53] N. Vianello, M. Spolaore, M. Agostini, R. Cavazzana, G. De Masi, E. Martines, B. Momo, P. Scarin, S. Spagnolo, and M. Zuin, "On the statistics and features of turbulent structures in rfx-mod," *Plasma Physics and Controlled Fusion*, vol. 58, no. 4, p. 044009, 2016.
- [54] D. Pace, M. Shi, J. Maggs, G. Morales, and T. Carter, "Exponential frequency spectrum and lorentzian pulses in magnetized plasmas," *Physics of Plasmas*, vol. 15, no. 12, p. 122304, 2008.
- [55] I. Furno, B. Labit, M. Podestà, A. Fasoli, S. Müller, F. Poli, P. Ricci, C. Theiler, S. Brunner, A. Diallo, *et al.*, "Experimental observation of the blob-generation mechanism from interchange waves in a plasma," *Physical review letters*, vol. 100, no. 5, p. 055004, 2008.
- [56] S. Krasheninnikov, D. D'ippolito, and J. Myra, "Recent theoretical progress in understanding coherent structures in edge and sol turbulence," *Journal of Plasma Physics*, vol. 74, no. 5, pp. 679–717, 2008.
- [57] I. P. E. G. on Divertor, I. P. E. G. on Divertor Modelling, Database, and I. P. B. Editors, "Chapter 4: Power and particle control," *Nuclear Fusion*, vol. 39, no. 12, p. 2391, 1999.
- [58] D. Carralero, P. Manz, L. Aho-Mantila, G. Birkenmeier, M. Brix, M. Groth, H. Müller, U. Stroth, N. Vianello, E. Wolfrum, *et al.*, "Experimental validation of a filament transport model in turbulent magnetized plasmas," *Physical review letters*, vol. 115, no. 21, p. 215002, 2015.
- [59] G. Xu, V. Naulin, W. Fundamenski, C. Hidalgo, J. Alonso, C. Silva, B. Goncalves, A. H. Nielsen, J. J. Rasmussen, S. Krasheninnikov, *et al.*, "Blob/hole formation and zonal-flow generation in the edge plasma of the jet tokamak," *Nuclear Fusion*, vol. 49, no. 9, p. 092002, 2009.
- [60] N. Bisai, A. Das, S. Deshpande, R. Jha, P. Kaw, A. Sen, and R. Singh, "Edge and scrape-off layer tokamak plasma turbulence simulation using two-field fluid model," *Physics of plasmas*, vol. 12, no. 7, p. 072520, 2005.
- [61] C. Theiler, I. Furno, P. Ricci, A. Fasoli, B. Labit, S. Müller, and G. Plyushchev, "Cross-field motion of plasma blobs in an open magnetic field line configuration," *Physical review letters*, vol. 103, no. 6, p. 065001, 2009.
- [62] F. Avino, A. Fasoli, I. Furno, P. Ricci, and C. Theiler, "X-point effect on plasma blob dynamics," *Physical review letters*, vol. 116, no. 10, p. 105001, 2016.

Bibliography

- [63] F. Riva, C. Colin, J. Denis, L. Easy, I. Furno, J. Madsen, F. Militello, V. Naulin, A. H. Nielsen, J. M. B. Olsen, *et al.*, “Blob dynamics in the torpex experiment: a multi-code validation,” *Plasma Physics and Controlled Fusion*, vol. 58, no. 4, p. 044005, 2016.
- [64] F. Militello, P. Tamain, W. Fundamenski, A. Kirk, V. Naulin, A. H. Nielsen, *et al.*, “Experimental and numerical characterization of the turbulence in the scrape-off layer of mast,” *Plasma Physics and Controlled Fusion*, vol. 55, no. 2, p. 025005, 2013.
- [65] J. R. Angus and M. V. Umansky, “Modeling of large amplitude plasma blobs in three-dimensions,” *Physics of Plasmas*, vol. 21, no. 1, p. 012514, 2014.
- [66] F. D. Halpern, A. Cardellini, P. Ricci, S. Jolliet, J. Loizu, and A. Mosetto, “Three-dimensional simulations of blob dynamics in a simple magnetized torus,” *Physics of Plasmas*, vol. 21, no. 2, p. 022305, 2014.
- [67] B. W. Shanahan and B. D. Dudson, “Blob dynamics in torpex poloidal null configurations,” *Plasma Physics and Controlled Fusion*, vol. 58, no. 12, p. 125003, 2016.
- [68] N. Nace, P. Tamain, C. Baudoin, H. Bufferand, G. Ciraolo, N. Fedorczak, D. Galassi, P. Ghendrih, and E. Serre, “Impact of safety factor and magnetic shear profiles on edge turbulence in circular limited geometry,” *Contributions to Plasma Physics*, 2018.
- [69] W. Gracias, P. Tamain, E. Serre, R. Pitts, and L. Garcia, “The impact of magnetic shear on the dynamics of a seeded 3d filament in slab geometry,” *Nuclear Materials and Energy*, vol. 12, pp. 798–807, 2017.
- [70] R. Churchill, C. Chang, S. Ku, and J. Dominski, “Pedestal and edge electrostatic turbulence characteristics from an xgc1 gyrokinetic simulation,” *Plasma Physics and Controlled Fusion*, vol. 59, no. 10, p. 105014, 2017.
- [71] F. Nespoli, I. Furno, B. Labit, P. Ricci, F. Avino, F. Halpern, F. Musil, and F. Riva, “Blob properties in full-turbulence simulations of the tcv scrape-off layer,” *Plasma Physics and Controlled Fusion*, vol. 59, no. 5, p. 055009, 2017.
- [72] R. Cohen, B. LaBombard, D. Ryutov, J. Terry, M. Umansky, X. Xu, and S. Zweben, “Theory and fluid simulations of boundary-plasma fluctuations,” *Nuclear fusion*, vol. 47, no. 7, p. 612, 2007.
- [73] D. Carralero, M. Siccino, M. Komm, S. Artene, F. D’Isa, J. Adamek, L. Aho-Mantila, G. Birkenmeier, M. Brix, G. Fuchert, *et al.*, “Recent progress towards a quantitative description of filamentary sol transport,” *Nuclear Fusion*, vol. 57, no. 5, p. 056044, 2017.
- [74] S. I. Krasheninnikov, “On scrape off layer plasma transport,” *Physics Letters A*, vol. 283, no. 5-6, pp. 368–370, 2001.
- [75] F. Nespoli, I. Furno, B. Labit, P. Ricci, F. Avino, F. Halpern, F. Musil, and F. Riva, “Blob properties in full-turbulence simulations of the tcv scrape-off layer,” *Plasma Physics and Controlled Fusion*, vol. 59, no. 5, p. 055009, 2017.

-
- [76] C. Theiler, I. Furno, A. Fasoli, P. Ricci, B. Labit, and D. Iraj, "Blob motion and control in simple magnetized plasmas," *Physics of Plasmas*, vol. 18, no. 5, p. 055901, 2011.
- [77] R. Pitts, R. Chavan, and J.-M. Moret, "The design of central column protection tiles for the tcv tokamak," *Nuclear Fusion*, vol. 39, no. 10, p. 1433, 1999.
- [78] T. Stoltzfus-Dueck, A. Karpushov, O. Sauter, B. Duval, B. Labit, H. Reimerdes, W. Vijvers, Y. Camenen, T. Team, *et al.*, "X-point-position-dependent intrinsic toroidal rotation in the edge of the tcv tokamak," *Physical review letters*, vol. 114, no. 24, p. 245001, 2015.
- [79] J.-M. Moret, B. Duval, H. Le, S. Coda, F. Felici, and H. Reimerdes, "Tokamak equilibrium reconstruction code liuqe and its real time implementation," *Fusion Engineering and Design*, vol. 91, pp. 1–15, 2015.
- [80] J. D'Errico, "inpaint_nans.m," 2012. https://ch.mathworks.com/matlabcentral/fileexchange/4551-inpaint_nans.
- [81] J. Rice, A. Ince-Cushman, L.-G. Eriksson, Y. Sakamoto, A. Scarabosio, A. Bortolon, K. Burrell, B. Duval, C. Fenzi-Bonizec, M. Greenwald, *et al.*, "Inter-machine comparison of intrinsic toroidal rotation in tokamaks," *Nuclear Fusion*, vol. 47, no. 11, p. 1618, 2007.
- [82] D. Galassi, P. Tamain, H. Bufferand, G. Ciraolo, P. Ghendrih, C. Baudoin, C. Colin, N. Fedorczak, N. Nace, and E. Serre, "Drive of parallel flows by turbulence and large-scale $\mathbf{e} \times \mathbf{b}$ transverse transport in divertor geometry," *Nuclear Fusion*, vol. 57, no. 3, p. 036029, 2017.
- [83] G. Xu, V. Naulin, W. Fundamenski, J. J. Rasmussen, A. H. Nielsen, and B. Wan, "Intermittent convective transport carried by propagating electromagnetic filamentary structures in nonuniformly magnetized plasma," *Physics of plasmas*, vol. 17, no. 2, p. 022501, 2010.

Avenue C.F. Ramuz 51
1009, Pully (VD)
+41787168008
paola.paruta@gmail.com



Paola Paruta

STRENGTHS

- Excellent computational skills
- International background

EXPERIENCE

Swiss Plasma Center, EPFL – *PhD in Nuclear Fusion, Physics*

September 2014 – September 2018

- Thesis title: “Simulation of plasma turbulence in the periphery of diverted tokamaks”, supervised by Prof. P. Ricci
- Developer of 3D fluid-dynamics code
- Teaching assistant for 7 EPFL courses

Board of European Students of Technology, Milano – *President*

September 2012 – September 2013

- Fundraising: +20.000 euro from Companies and Universities
- Human Resources: 150% increase in active members

EDUCATION

Politecnico di Milano – *Master in Scientific Computing*

September 2011 – July 2014

- Master thesis project at KU Leuven, Belgium on *Interstellar dust coagulation modelling*
- Exchange semester at TU/e, Eindhoven, Netherlands

Politecnico di Milano – *Bachelor in Mathematical Engineering*

September 2008 – September 2011

- Final project with Prof. Alfio Quarteroni

ACTIVISM

International Civil Service (Tanzania), Amnesty International (CH), Scouting (IT), International Civil Service (Thailand), Volunteering at Orphanage (Malawi)

LANGUAGES

Italian (native) English (C2) French (C1) Spanish (A1) German (A0)